

Theses and Dissertations

Spring 2014

# Low velocity impact testing and computed tomography damage evaluation of layered textile composite

Changpeng Song University of Iowa

Follow this and additional works at: https://ir.uiowa.edu/etd



Part of the Mechanical Engineering Commons

Copyright 2014 Changpeng Song

This thesis is available at Iowa Research Online: https://ir.uiowa.edu/etd/4759

#### **Recommended Citation**

Song, Changpeng. "Low velocity impact testing and computed tomography damage evaluation of layered textile composite." MS (Master of Science) thesis, University of Iowa, 2014. https://doi.org/10.17077/etd.icd69hdx

Follow this and additional works at: https://ir.uiowa.edu/etd



# LOW VELOCITY IMPACT TESTING AND COMPUTED TOMOGRAPHY DAMAGE EVALUATION OF LAYERED TEXTILE COMPOSITE

by

Changpeng Song

A thesis submitted in partial fulfillment of the requirements for the Master of Science degree in Mechanical Engineering in the Graduate College of The University of Iowa

May 2014

Thesis Supervisor: Associate Professor Olesya I. Zhupanska



# Graduate College The University of Iowa Iowa City, Iowa

CE -	RTIFICATE OF APPROVAL
	MASTER'S THESIS
This is to certify tha	t the Master's thesis of
	Changpeng Song
for the thesis require	by the Examining Committee ement for the Master of Science al Engineering at the May 2014 graduation.
Thesis Committee:	Olesya I. Zhupanska, Thesis Supervisor
	Hiroyuki Sugiyama
	Albert Ratner



To My Loving and Adoring Family



#### **ACKNOWLEDGEMENTS**

I would like to express my sincere appreciation to my excellent advisor, Professor Olesya I. Zhupanska for all of her guidance, support, and belief throughout both my research and coursework at The University of Iowa. The knowledge I have gained is invaluable. The research skills I have developed from Professor Olesya I. Zhupanska will benefit me a lot in my future career and life. The research experience has truly been rewarding and enjoyable. I would also like to thank Professors Hiroyuki Sugiyama for his time and support over my last semester for MS degree. My appreciation also goes to Professor Albert Ratner and Hiroyuki Sugiyama for taking their valuable time to serve on my thesis defense committee.

In addition, I would like to express my gratitude to PhD students, Yeqing Wang for his guidance, motivation, and assistance with impact experiments. I also would like to thank Abhilash Kizhakke Puliyakote (Prof. Hoffman's Lab, Department of Radiology, University of Iowa) for assistance with Micro-CT imaging and Michael Lee (Schneider Electric, Cedar Rapids) for assistance with CT imaging using ZEISS METROTOM 1500.

Finally, I would like thank my parents and my wife for their support during my enjoyable education at The University of Iowa.



# TABLE OF CONTENTS

LIST OF TABLES	vi
LIST OF FIGURESv	'ii
CHAPTER 1 INTRODUCTION	.1
1.1 Background Information	.2 .8 11 13 24
CHAPTER 2 LOW VELOCITY IMPACT TESTING OF TEXTILE COMPOISTES	27
2.1 Experimental Setup	27 34
CHAPTER 3 CT IMAGE ANALYSIS5	8
3.1 CT Technology Overview5 3.2 ZEISS METROTOM 1500 Computed Tomography Scanner and	
Image Analysis Software	66
3.4.1 ZEISS METROTOM 1500 CT Results for the Specimens Impacted at the Lowest Impact Energy	77
Impacted at the Highest Impact Energy	)3
CHAPTER 4 SUMMARY AND RECOMMENDATIONS	30
4.1 Summary 13 4.2 Recommendations 13	30 31
APPENDIX A ZEISS METROTOM 1500 CT RESULTS FOR THE SPECIMENS IMPACTED AT THE LOWEST IMPACT ENERGY13	32
APPENDIX B ZEISS METROTOM 1500 CT RESULTS FOR THE SPECIMENS IMPACTED AT THE INTERMEDIATE IMPACT ENERGY14	ŀ6
APPENDIX C ZEISS METROTOM 1500 CT RESULTS FOR THE SPECIMENS IMPACTED AT THE HIGHEST IMPACT ENERGY18	30



## LIST OF TABLES

Table 2. 1: The measurement of the specimen	37
Table 2. 2: Impact test conditions	39
Table 2. 3: Results of the impact tests	39
Table 3. 1: Damage size at different depths away from the impact surface with intermediate impact energy	89
Table 3. 2: Damage size at different depths away from the impact surface with highest impact energy	99
Table 3. 3: Damage Volume, Impact Energy, Max Impact Force and Total Absorbed Energy of each sample	100



# LIST OF FIGURES

Figure 1. 1: Three fundamental ways to weave for woven fabric composites	3
Figure 1. 2: Plain weave (left) and basket weave (right)	4
Figure 1. 3: Leno weave (left) and four harnesses satin (right)	4
Figure 1. 4: Eight harness (left) and satin twill weave (right)	5
Figure 1. 5: Weft (left) and warp (right) knitted fabrics	6
Figure 1. 6: Braided fabrics composite	7
Figure 1. 7: Braided carbon fabrics	8
Figure 1. 8: Procedure to manufacture the textile composite	9
Figure 1. 9: The cylindrical mandrel to manufacture a braided composite	10
Figure 1. 10: The application of textile composites	11
Figure 1. 11: Procedure to manufacture the textile composite pressure bulkhead	12
Figure 1. 12: CFM International new LEAP engine with 18 blades made from 3D woven composite	12
Figure 1. 13: New Tegris baggage made from the textile composite	13
Figure 1. 14: Orientation of delaminations.	15
Figure 1. 15: Two types of matrix Cracks (a) Tensile crack (b) Shear crack	16
Figure 1. 16: Damage patterns of composite after impact (a) The damage pattern for thick composite (b) The damage pattern for thin composite	17
Figure 2. 1: Instron 8200 Impact Tester	28
Figure 2. 2: Two Pneumatic Self-Rebounding Stoppers	29
Figure 2. 3: The Clamping Fixture	30
Figure 2. 4: The Photogate and Flag	31
Figure 2. 5: Instrumented Load Cell	32
Figure 2. 6: Impact Tester Signal Conditioning Box	33
Figure 2. 7: Textile of the Specimen (the arrow indicates a 0° direction)	34



Figure 2. 8: Cutting Layout of Composite Panel 1 (the Arrow Indicates 0° Direction)	35
Figure 2. 9: Cutting Layout of Composite Panel 2 (the Arrow Indicates 0° Direction)	36
Figure 2. 10: Impact Test Samples (1-4, 1-5, 1-6)	37
Figure 2. 11: Impact Load vs. Time	40
Figure 2. 12: Impact Load vs. Deflection	41
Figure 2. 13: Deflection vs. Time.	42
Figure 2. 14: Impact Load vs. Time for the Specimens Impacted at the Lowest Energy, 16 J.	43
Figure 2. 15: Impact Load vs. Deflection for the Specimens Impacted at the Lowest Energy, 16 J.	44
Figure 2. 16: Deflection vs. Time for the Specimens Impacted at the Lowest Energy, 16 J.	45
Figure 2. 17: Impact Load vs. Time for the Specimens Impacted at the Intermediate Energy, 22.5 J.	46
Figure 2. 18: Impact Load vs. Deflection for the Specimens Impacted at the Intermediate Energy, 22.5 J	47
Figure 2. 19: Deflection vs. Time for the Specimens Impacted at the Intermediate Energy, 22.5 J.	48
Figure 2. 20: Impact Load vs. Time for the Specimens Impacted at the Highest Energy, 26 J.	49
Figure 2. 21: Impact Load vs. Deflection for the Specimens Impacted at the Highest Energy, 26 J.	50
Figure 2. 22: Deflection vs. Time for the Specimens Impacted at the Highest Energy, 26 J.	51
Figure 2. 23: Impact Load vs. Time for Three Representative Specimens	52
Figure 2. 24: Impact Load vs. Deflection for Three Representative Specimens	53
Figure 2. 25: Deflection vs. Time for Three Representative Specimens	54
Figure 2. 26: Specimens Impacted at the Lowest Energy, 16 J.	55
Figure 2. 27: Specimens Impacted at the Intermediate Energy, 22.5.	56
Figure 2. 28: Specimens Impacted at the Highest Energy, 26 J.	57

Figure 3. 1: General Operation and Major Components of the Modern Industrial CT System	.58
Figure 3. 2: Multi-scale Computed Tomography of Aerospace-Grade Material	.60
Figure 3. 3: ZEISS METROTOM 1500 System (Lettenbauer, 2007)	.62
Figure 3. 4: ZEISS METROTOM 1500 System Internal Structure	.63
Figure 3. 5: Scan Direction of Each Scan Plane	.65
Figure 3. 6: Siemens MicroCAT II Scanner	.67
Figure 3. 7: The Scanner Bed in the Siemens MicroCAT II Scanner	.68
Figure 3. 8: 3D Rendering CT Scan of a Mouse from the Siemens MicroCAT II Scanner	.68
Figure 3. 9: Gray-Values Setting of Human Head	.70
Figure 3. 10: Gray-Values Setting of samples scanned using the ZEISS METROTOM 1500.	.71
Figure 3. 11: CT image at the plane located 0.22 mm away from the impacted surface	.72
Figure 3. 12: CT image at the plane located 0.47 mm away from the impacted surface	.72
Figure 3. 13: CT image at the plane located 0.62 mm away from the impacted surface	.72
Figure 3. 14: CT image at the plane located 0.77 mm away from the impacted surface	.73
Figure 3. 15: CT image at the plane located 1.07 mm away from the impacted surface	.73
Figure 3. 16: CT image at the plane located 1.37 mm away from the impacted surface	.73
Figure 3. 17: CT image at the plane located 1.62 mm away from the impacted surface	.74
Figure 3. 18: CT image at the plane located 1.87 mm away from the impacted surface	.74
Figure 3. 19: CT image at the plane located 2.22 mm away from the impacted surface	.74
Figure 3. 20: CT image at the plane located 2.37 mm away from the impacted	75



Figure 3. 21: CT image at the plane located 2.67 mm away from the impacted surface	75
Figure 3. 22: CT image at the plane located 2.92 mm away from the impacted surface	75
Figure 3. 23: CT image at the plane located 3.12 mm away from the impacted surface	76
Figure 3. 24: CT image at the plane located 3.37 mm away from the impacted surface	76
Figure 3. 25: CT image at the plane located 3.57 mm away from the impacted surface	76
Figure 3. 26: CT image at the plane located 3.87 mm away from the impacted surface	77
Figure 3. 27: CT image at the plane located 0.22 mm away from the impacted surface	78
Figure 3. 28: CT image at the plane located 0.47 mm away from the impacted surface	78
Figure 3. 29: CT image at the plane located 0.62 mm away from the impacted surface	79
Figure 3. 30: CT image at the plane located 0.77 mm away from the impacted surface	79
Figure 3. 31: CT image at the plane located 1.07 mm away from the impacted surface	80
Figure 3. 32: CT image at the plane located 1.37 mm away from the impacted surface	80
Figure 3. 33: CT image at the plane located 1.62 mm away from the impacted surface	81
Figure 3. 34: CT image at the plane located 1.87 mm away from the impacted surface	81
Figure 3. 35: CT image at the plane located 2.22 mm away from the impacted surface	82
Figure 3. 36: CT image at the plane located 2.37 mm away from the impacted surface	82
Figure 3. 37: CT image at the plane located 2.67 mm away from the impacted surface	83
Figure 3. 38: CT image at the plane located 2.92 mm away from the impacted surface	83



Figure 3. 39:	CT image at the plane located 3.12 mm away from the impacted surface
Figure 3. 40:	CT image at the plane located 3.37 mm away from the impacted surface
Figure 3. 41:	CT image at the plane located 3.57 mm away from the impacted surface
Figure 3. 42:	CT image at the plane located 3.87 mm away from the impacted surface
Figure 3. 43:	CT image at the plane with the largest damage size in sample 1-4 (located 2.17 mm away from the impacted surface)86
Figure 3. 44:	CT image at the plane with the largest damage size in sample 1-5 (located 1.87 mm away from the impacted surface)87
Figure 3. 45:	CT image at the plane with the largest damage size in sample 1-6 (located 2.22 mm away from the impacted surface)
Figure 3. 46:	CT image at the plane located 0.22 mm away from the impacted surface
Figure 3. 47:	CT image at the plane located 0.47 mm away from the impacted surface
Figure 3. 48:	CT image at the plane located 0.62 mm away from the impacted surface
Figure 3. 49:	CT image at the plane located 0.77 mm away from the impacted surface
Figure 3. 50:	CT image at the plane located 1.07 mm away from the impacted surface
	CT image at the plane located 1.37 mm away from the impacted surface
Figure 3. 52:	CT image at the plane located 1.62 mm away from the impacted surface
Figure 3. 53:	CT image at the plane located 1.87 mm away from the impacted surface
Figure 3. 54:	CT image at the plane located 2.22 mm away from the impacted surface
Figure 3. 55:	CT image at the plane located 2.37 mm away from the impacted surface
Figure 3. 56:	CT image at the plane located 2.67 mm away from the impacted surface



	CT image at the plane located 2.92 mm away from the impacted surface	94
	CT image at the plane located 3.12 mm away from the impacted surface	94
	CT image at the plane located 3.37 mm away from the impacted surface	95
	CT image at the plane located 3.57 mm away from the impacted surface	95
	CT image at the plane located 3.87 mm away from the impacted surface	95
	CT image at the plane with the largest damage size in sample 2-4 (located 2.43 mm away from the impacted surface)	96
	CT image at the plane with the largest damage size in sample 2-5 (located 2.47 mm away from the impacted surface)	97
Figure 3. 64: 1	Damage Volume vs. Impact Energy	101
Figure 3. 65:	Damage Volume vs. Max Impact Force	101
Figure 3. 66: 1	Damage Volume vs. Absorbed Energy	102
	Micro-CT image at the plane located 0.22 mm away from the impacted surface	104
	Micro-CT image at the plane located 0.47 mm away from the impacted surface	105
	Micro-CT image at the plane located 0.62 mm away from the impacted surface	105
Figure 3. 70:	Micro-CT image at the plane located 0.77 mm away from the impacted surface	106
	Micro-CT image at the plane located 1.07 mm away from the impacted surface	106
	Micro-CT image at the plane located 1.37 mm away from the impacted surface	107
	Micro-CT image at the plane located 1.62 mm away from the impacted surface	107
	Micro-CT image at the plane located 1.87 mm away from the impacted surface	108
	Micro-CT image at the plane located 2.22 mm away from the impacted surface	108



Figure 3. 70	5: Micro-CT image at the plane located 2.37 mm away from the impacted surface
Figure 3. 7'	7: Micro-CT image at the plane located 2.67 mm away from the impacted surface
Figure 3. 78	3: Micro-CT image at the plane located 2.92 mm away from the impacted surface
Figure 3. 79	9: Micro-CT image at the plane located 3.12 mm away from the impacted surface
Figure 3. 80	2): Micro-CT image at the plane located 3.37 mm away from the impacted surface
Figure 3. 8	1: Micro-CT image at the plane located 3.57 mm away from the impacted surface
Figure 3. 82	2: Micro-CT image at the plane located 3.87 mm away from the impacted surface
Figure 3. 83	3: CT image comparison at the plane located 0.22 mm away from the impacted surface
Figure 3. 84	4: CT image comparison at the plane located 0.47 mm away from the impacted surface
Figure 3. 8:	5: CT image comparison at the plane located 0.62 mm away from the impacted surface
Figure 3. 86	5: CT image comparison at the plane located 0.77 mm away from the impacted surface
Figure 3. 8'	7: CT image comparison at the plane located 1.07 mm away from the impacted surface
Figure 3. 88	3: CT image comparison at the plane located 1.37 mm away from the impacted surface
Figure 3. 89	9: CT image comparison at the plane located 1.62 mm away from the impacted surface
Figure 3. 90	2): CT image comparison at the plane located 1.87 mm away from the impacted surface
Figure 3. 9	1: CT image comparison at the plane located 2.22 mm away from the impacted surface
Figure 3. 92	2: CT image comparison at the plane located 2.37 mm away from the impacted surface
Figure 3. 93	3: CT image comparison at the plane located 2.67 mm away from the impacted surface 118



Figure 3. 94: CT image comparison at the plane located 2.92 mm away from the impacted surface	119
Figure 3. 95: CT image comparison at the plane located 3.12 mm away from the impacted surface	119
Figure 3. 96: CT image comparison at the plane located 3.37 mm away from the impacted surface	120
Figure 3. 97: CT image comparison at the plane located 3.57 mm away from the impacted surface	120
Figure 3. 98: CT image comparison at the plane located 3.87 mm away from the impacted surface	121
Figure 3. 99: CT image comparison at the plane located 0.22 mm away from the impacted surface	121
Figure 3. 100: CT image comparison at the plane located 0.47 mm away from the impacted surface	122
Figure 3. 101: CT image comparison at the plane located 0.62 mm away from the impacted surface	122
Figure 3. 102: CT image comparison at the plane located 0.77 mm away from the impacted surface	123
Figure 3. 103: CT image comparison at the plane located 1.07 mm away from the impacted surface	123
Figure 3. 104: CT image comparison at the plane located 1.37 mm away from the impacted surface	124
Figure 3. 105: CT image comparison at the plane located 1.62 mm away from the impacted surface	124
Figure 3. 106: CT image comparison at the plane located 1.87 mm away from the impacted surface	125
Figure 3. 107: CT image comparison at the plane located 2.22 mm away from the impacted surface	125
Figure 3. 108: CT image comparison at the plane located 2.37 mm away from the impacted surface	126
Figure 3. 109: CT image comparison at the plane located 2.67 mm away from the impacted surface	126
Figure 3. 110: CT image comparison at the plane located 2.92 mm away from the impacted surface	127
Figure 3. 111: CT image comparison at the plane located 3.12 mm away from the	127



Figure 3. 112: CT image comparison at the plane located 3.37 mm away from the impacted surface	128
Figure 3. 113: CT image comparison at the plane located 3.57 mm away from the impacted surface	128
Figure 3. 114: CT image comparison at the plane located 3.87 mm away from the impacted surface	129
Figure A. 1: Sample 2-1	132
Figure A. 2: CT image at the plane located 0. 22 mm away from the impacted surface of sample 2-1	133
Figure A. 3: CT image at the plane located 1.87 mm away from the impacted surface of sample 2-1	133
Figure A. 4: CT image at the plane located 2.22 mm away from the impacted surface of sample 2-1	134
Figure A. 5: CT image at the plane located 2.37 mm away from the impacted surface of sample 2-1	134
Figure A. 6: CT image at the plane located 3.87 mm away from the impacted surface of sample 2-1	135
Figure A. 7: Sample 2-2	136
Figure A. 8: CT image at the plane located 0. 22 mm away from the impacted surface of sample 2-2	136
Figure A. 9: CT image at the plane located 0.47 mm away from the impacted surface of sample 2-2	137
Figure A. 10: CT image at the plane located 2.22 mm away from the impacted surface of sample 2-2	137
Figure A. 11: CT image at the plane located 2.37 mm away from the impacted surface of sample 2-2	138
Figure A. 12: CT image at the plane located 2.67 mm away from the impacted surface of sample 2-2	138
Figure A. 13: CT image at the plane located 3.87 mm away from the impacted surface of sample 2-2	139
Figure A. 14: Sample 2-3	140
Figure A. 15: CT image at the plane located 0. 22 mm away from the impacted surface of sample 2-3	140
Figure A. 16: CT image at the plane located 0.47 mm away from the impacted	1/1



Figure A. 17: CT image at the plane located 0.62 mm away from the impacted surface of sample 2-2	141
Figure A. 18: CT image at the plane located 1.87 mm away from the impacted surface of sample 2-3	142
Figure A. 19: CT image at the plane located 2.22 mm away from the impacted surface of sample 2-3	142
Figure A. 20: CT image at the plane located 2.37 mm away from the impacted surface of sample 2-3	143
Figure A. 21: CT image at the plane located 2.67 mm away from the impacted surface of sample 2-3	143
Figure A. 22: CT image at the plane located 2.97 mm away from the impacted surface of sample 2-3	144
Figure A. 23: CT image at the plane located 3.12 mm away from the impacted surface of sample 2-3	144
Figure A. 24: CT image at the plane located 3.87 mm away from the impacted surface of sample 2-3	145
Figure B. 1: Sample 1-4	146
Figure B. 2: CT image in the center of sample 1-4 in the right scan direction	147
Figure B. 3: CT image in the center of sample 1-4 in the front scan direction	147
Figure B. 4: CT image at the plane located 0.22 mm away from the impacted surface of sample 1-4	148
Figure B. 5: CT image at the plane located 0.47 mm away from the impacted surface of sample 1-4	149
Figure B. 6: CT image at the plane located 0.62 mm away from the impacted surface of sample 1-4	149
Figure B. 7: CT image at the plane located 0.77 mm away from the impacted surface of sample 1-4	150
Figure B. 8: CT image at the plane located 1.07 mm away from the impacted surface of sample 1-4	150
Figure B. 9: CT image at the plane located 1.37 mm away from the impacted surface of sample 1-4.	151
Figure B. 10: CT image at the plane located 1.62 mm away from the impacted surface of sample 1-4	151
Figure B. 11: CT image at the plane located 1.87 mm away from the impacted	152



Figure B. 12: CT image at the plane located 2.22 mm away from the impacted surface of sample 1-4	152
Figure B. 13: CT image at the plane located 2.37 mm away from the impacted surface of sample 1-4	153
Figure B. 14: CT image at the plane located 2.67 mm away from the impacted surface of sample 1-4	153
Figure B. 15: CT image at the plane located 2.92 mm away from the impacted surface of sample 1-4	154
Figure B. 16: CT image at the plane located 3.12 mm away from the impacted surface of sample 1-4	154
Figure B. 17: CT image at the plane located 3.37 mm away from the impacted surface of sample 1-4	155
Figure B. 18: CT image at the plane located 3.57 mm away from the impacted surface of sample 1-4	155
Figure B. 19: CT image at the plane located 3.87 mm away from the impacted surface of sample 1-4	156
Figure B. 20: CT image at the plane with the largest damage size in sample 1-4 (located 2.17 mm away from the impacted surface)	156
Figure B. 21: Sample 1-5	157
Figure B. 21: Sample 1-5  Figure B. 22: CT image in the center of sample 1-5 in the right scan direction	
	158
Figure B. 22: CT image in the center of sample 1-5 in the right scan direction	158
Figure B. 22: CT image in the center of sample 1-5 in the right scan direction  Figure B. 23: CT image in the center of sample 1-5 in the front scan direction  Figure B. 24: CT image at the plane located 0.22 mm away from the impacted	158 159 160
Figure B. 22: CT image in the center of sample 1-5 in the right scan direction  Figure B. 23: CT image in the center of sample 1-5 in the front scan direction  Figure B. 24: CT image at the plane located 0.22 mm away from the impacted surface of sample 1-5  Figure B. 25: CT image at the plane located 0.47 mm away from the impacted	158 159 160
Figure B. 22: CT image in the center of sample 1-5 in the right scan direction  Figure B. 23: CT image in the center of sample 1-5 in the front scan direction  Figure B. 24: CT image at the plane located 0.22 mm away from the impacted surface of sample 1-5  Figure B. 25: CT image at the plane located 0.47 mm away from the impacted surface of sample 1-5  Figure B. 26: CT image at the plane located 0.62 mm away from the impacted	158 159 160 160
Figure B. 22: CT image in the center of sample 1-5 in the right scan direction  Figure B. 23: CT image in the center of sample 1-5 in the front scan direction  Figure B. 24: CT image at the plane located 0.22 mm away from the impacted surface of sample 1-5  Figure B. 25: CT image at the plane located 0.47 mm away from the impacted surface of sample 1-5  Figure B. 26: CT image at the plane located 0.62 mm away from the impacted surface of sample 1-5  Figure B. 27: CT image at the plane located 0.77 mm away from the impacted	158 159 160 161
Figure B. 22: CT image in the center of sample 1-5 in the right scan direction  Figure B. 23: CT image in the center of sample 1-5 in the front scan direction  Figure B. 24: CT image at the plane located 0.22 mm away from the impacted surface of sample 1-5  Figure B. 25: CT image at the plane located 0.47 mm away from the impacted surface of sample 1-5  Figure B. 26: CT image at the plane located 0.62 mm away from the impacted surface of sample 1-5  Figure B. 27: CT image at the plane located 0.77 mm away from the impacted surface of sample 1-5  Figure B. 28: CT image at the plane located 1.07 mm away from the impacted surface of sample 1-5	158 159 160 161 161



	T image at the plane located 1.87 mm away from the impacted urface of sample 1-5	163
Figure B. 32: C	T image at the plane located 2.22 mm away from the impacted urface of sample 1-5	164
Figure B. 33: C	T image at the plane located 2.37 mm away from the impacted urface of sample 1-5	164
Figure B. 34: C	T image at the plane located 2.67 mm away from the impacted urface of sample 1-5	165
Figure B. 35: C	T image at the plane located 2.92 mm away from the impacted urface of sample 1-5	165
Figure B. 36: C	T image at the plane located 3.12 mm away from the impacted urface of sample 1-5	166
Figure B. 37: C	T image at the plane located 3.37 mm away from the impacted urface of sample 1-5	166
Figure B. 38: C	T image at the plane located 3.57 mm away from the impacted urface of sample 1-5	167
Figure B. 39: C	T image at the plane located 3.87 mm away from the impacted urface of sample 1-5	167
	T image at the plane with the largest damage size in sample 1-5 located 1.87 mm away from the impacted surface)	168
Figure B. 41: Sa	ample 1-6	169
	T image at the plane located 0.22 mm away from the impacted urface of sample 1-6	170
	T image at the plane located 0.47 mm away from the impacted urface of sample 1-6	170
	T image at the plane located 0.62 mm away from the impacted urface of sample 1-6	171
	T image at the plane located 0.77 mm away from the impacted urface of sample 1-6	171
	T image at the plane located 1.07 mm away from the impacted urface of sample 1-6	172
	T image at the plane located 1.37 mm away from the impacted urface of sample 1-6	172
	T image at the plane located 1.62 mm away from the impacted	173



Figure B. 49: CT image at the plane located 1.87 mm away from the impacted surface of sample 1-6	173
Figure B. 50: CT image at the plane located 2.22 mm away from the impacted surface of sample 1-6	174
Figure B. 51: CT image at the plane located 2.37 mm away from the impacted surface of sample 1-6	174
Figure B. 52: CT image at the plane located 2.67 mm away from the impacted surface of sample 1-6	175
Figure B. 53: CT image at the plane located 2.92 mm away from the impacted surface of sample 1-6	175
Figure B. 54: CT image at the plane located 3.12 mm away from the impacted surface of sample 1-6	176
Figure B. 55: CT image at the plane located 3.37 mm away from the impacted surface of sample 1-6	176
Figure B. 56: CT image at the plane located 3.57 mm away from the impacted surface of sample 1-6	177
Figure B. 57: CT image at the plane located 3.87 mm away from the impacted surface of sample 1-6	177
Figure B. 58: CT image at the plane with the largest damage size in sample 1-6 (located 2.22 mm away from the impacted surface)	178
Figure C. 1: Sample 2-4	180
Figure C. 2: CT image at the plane located 0.22 mm away from the impacted surface of sample 2-4	181
Figure C. 3: CT image at the plane located 0.47 mm away from the impacted surface of sample 2-4	181
Figure C. 4: CT image at the plane located 0.62 mm away from the impacted surface of sample 2-4.	182
Figure C. 5: CT image at the plane located 0.77 mm away from the impacted surface of sample 2-4	182
Figure C. 6: CT image at the plane located 1.07 mm away from the impacted surface of sample 2-4	183
Figure C. 7: CT image at the plane located 1.37 mm away from the impacted surface of sample 2-4	183
Figure C. 8: CT image at the plane located 1.62 mm away from the impacted surface of sample 2-4	184



Figure C. 9: CT image at the plane located 1.87 mm away from the impacted surface of sample 2-4	184
Figure C. 10: CT image at the plane located 2.22 mm away from the impacted surface of sample 2-4	185
Figure C. 11: CT image at the plane located 2.37 mm away from the impacted surface of sample 2-4	185
Figure C. 12: CT image at the plane located 2.67 mm away from the impacted surface of sample 2-4	186
Figure C. 13: CT image at the plane located 2.97 mm away from the impacted surface of sample 2-4	186
Figure C. 14: CT image at the plane located 3.12 mm away from the impacted surface of sample 2-4	187
Figure C. 15: CT image at the plane located 3.37 mm away from the impacted surface of sample 2-4	187
Figure C. 16: CT image at the plane located 3.57 mm away from the impacted surface of sample 2-4	188
Figure C. 17: CT image at the plane located 3.87 mm away from the impacted surface of sample 2-4	188
Figure C. 18: CT image at the plane with the largest damage size in sample 2-4 (located 2.43 mm away from the impacted surface)	189
Figure C. 19: Sample 2-5	190
Figure C. 20: CT image at the plane located 0.22 mm away from the impacted surface of sample 2-5	190
Figure C. 21: CT image at the plane located 0.47 mm away from the impacted surface of sample 2-5	191
Figure C. 22: CT image at the plane located 0.62 mm away from the impacted surface of sample 2-5	191
Figure C. 23: CT image at the plane located 0.77 mm away from the impacted surface of sample 2-5	192
Figure C. 24: CT image at the plane located 1.07 mm away from the impacted surface of sample 2-5	192
Figure C. 25: CT image at the plane located 1.37 mm away from the impacted surface of sample 2-5	193
Figure C. 26: CT image at the plane located 1.62 mm away from the impacted surface of sample 2-5	193



Figure C. 27:	CT image at the plane located 1.87 mm away from the impacted surface of sample 2-5	194
Figure C. 28:	CT image at the plane located 2.22 mm away from the impacted surface of sample 2-5	194
Figure C. 29:	CT image at the plane located 2.37 mm away from the impacted surface of sample 2-5	195
Figure C. 30:	CT image at the plane located 2.67 mm away from the impacted surface of sample 2-5	195
Figure C. 31:	CT image at the plane located 2.92 mm away from the impacted surface of sample 2-5	196
Figure C. 32:	CT image at the plane located 3.12 mm away from the impacted surface of sample 2-5	196
Figure C. 33:	CT image at the plane located 3.37 mm away from the impacted surface of sample 2-5	197
Figure C. 34:	CT image at the plane located 3.57 mm away from the impacted surface of sample 2-5	197
Figure C. 35:	CT image at the plane located 3.87 mm away from the impacted surface of sample 2-5	198
Figure C. 36:	CT image at the plane with the largest damage size in sample 2-5 (located 2.47 mm away from the impacted surface)	198



#### CHAPTER 1

#### INTRODUCTION

#### 1.1 Background Information

With the development of science and technology, the application of composite materials is increasingly important to society. With superior properties like high strength, low density, and high stiffness, composite materials make a big contribution to the automotive, aerospace, maritime, and energy industries.

Composite materials can be defined as the materials that are formed by combining two or more materials on a macroscopic scale. Composite materials often exhibit better properties than traditional materials, and they often have qualities that their constituents do not possess, such as strength, stiffness, resistance, attractiveness, fatigue life, and some thermal properties (Jones, 1998).

There are two types of constituents of composite materials: the reinforcement and the matrix. With the reinforcement, the composite materials can have a better strength, stiffness. Then the matrix will fix the reinforcement and help to transfer its load.

Therefore, both the reinforcement and the matrix have important functions in composite materials. According to the fiber architecture, composite structures can be regarded as laminated composites, 2D fabric composites, and structural composites. One example is3D fabric composites in which the fibrous reinforcements are interlaced in multiple directions. Traditional laminated composite structures are obtained by stacking a number of unidirectional laminas so that they exhibit inferior out-of-plane mechanical properties. They can be expensive to manufacture due to high labor and production costs (Clarke, 1998). To overcome inferior out-of-plane mechanical properties, the fibers can be woven in certain ways to obtain better material properties. Therefore, woven fabric composites are recognized as more competitive than unidirectional composites for their impact resistance (Jones, 1998).



Research on composite materials subjected to impact load has been done for many years. Some studies have been about the behavior of a composite structure subjected to low-velocity impact. These days, textile composites provide tremendous potential applications due to their superior characteristics such as light weight, high strength, and good damage tolerance. Therefore, textile composites are ideal materials for designers to use in the aerospace, automobile, and armor industries.

A textile composite material usually consists of the textile reinforcement combined with the polymer matrix. The fibers form yarns and eventually the textile fabric. There are two types of reinforcements in a textile: two-dimensional (2D) and three-dimensional (3D) (Jones, 1998).

If the yarns are arranged in the thickness direction, it will be classified as 3D.

Normally, 3D fabrics are thicker than 2D fabrics because 2D fabrics have only one layer of reinforcement.

Textile composites have better impact properties than traditional composites due to the interlacing of yarns in a textile. In addition, textile composites have higher energy absorption capabilities because the matrix cracks will stop when the yarn changes its direction.

# 1.2 Classification of Textile Composite Material

Usually, there are three kinds of textile composite materials:woven fabric composites, knitted fabric composites, and braided fabric composites (see Figure 1.1). For general woven fabric composite materials, two orthogonal yarns, known as warp and weft, are interlaced. Usually the warp yarns go vertically and weft yarns go horizontally.



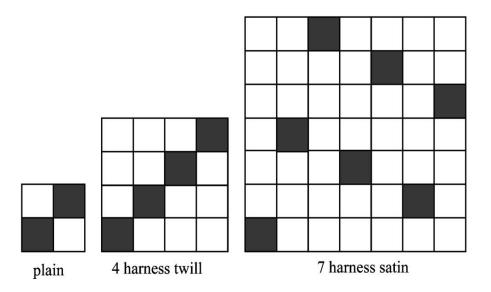


Figure 1. 1: Three fundamental ways to weave for woven fabric composites (Onal, 2007)

For industrial purposes, there are several basic patterns of woven composite reinforcements: plain weave, basket weave, leno weave, four harness satin, eight harness satin, and twill weave (Hexcel, 2010). They are shown in Figures 1.2-1.4.In the plain weave, yarns interlace in an alternating pattern. The pattern has each warp yarn intersecting with each weft yarn. The plain weave pattern could provide good fabric stability, but it does not have good pliability. In the basket weave pattern, similar to the plain weave, two or more warp yarns alternately interlace over two or more weft yarns. Besides providing more pliability, the basket weave pattern is flatter and stronger. However, its stability is not very good. The leno weave pattern has less yarn than the other types. Crossing two or more warp threads over each and interlacing with the weft threads can help to lock the yarns for this kind of weave reinforcement. For four harness satin, its weave reinforcement has a three-by-one interfacing as shown in the Figure 1.3.



It is more pliable than the plain weave, more suitable for curved surfaces, and typically used in reinforced plastics. Like the four harness satin, in the eight harnesses satin, one filling yarn floats over seven warp yarns and under one. It is also more pliable than the plain weave. The twill weave produces diagonal lines on the face of the fabric. The diagonal line is often formed by one warp yarn floating over two or more weft yarns. So this kind of weave reinforcement is often more pliable and stable than the plain weave (Hexcel, 2010).

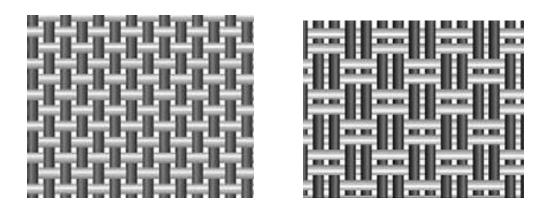


Figure 1. 2: Plain weave (left) and basket weave (right)(Hexcel, 2010)

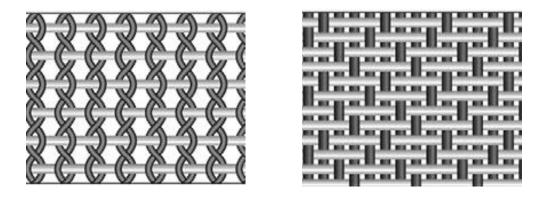


Figure 1. 3: Leno weave(left) and four harnesses satin(right)(Hexcel, 2010)



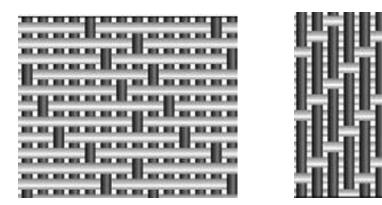


Figure 1. 4: Eight harness (left) and satin twill weave(right) (Hexcel, 2010)

In the directions of warp and weft, woven fabrics often have good stability and provide high plane strength. Moreover, it has good formability due to its low shear rigidity. However it does not have good in-plane shear resistance. Compared to other kinds of fabric composites, it provides anisotropy and less extensibility for molding. Some parameters, like the size and length of yarns, weave architecture, fiber orientation angle and volume fraction, can conduct the mechanical properties of woven fabrics (P. Tan, 1997).

Knitted fabric composites are often characterized by interlocking loops of yarns. There are two types of knitted fabrics: warp knitted fabric and weft knitted. Generally, the loops in the longitudinal direction are warp, and the loops in the width direction are weft. This kind of fabric composite is shown in Figure 1.5.



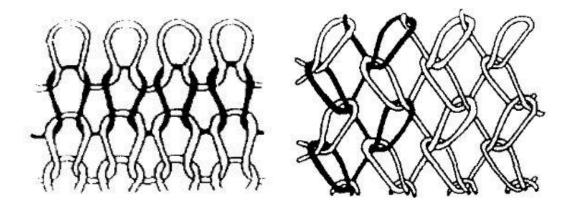


Figure 1. 5: Weft (left) and warp (right) knitted fabrics (P. Tan, 1997)

Compared to other kinds of textile fabrics, knitted fabrics have high productivity, low cost, and high extensibility. These good characteristic can provide good formability to get complicated shapes. Moreover, the knitted fabric composite has better impact resistance. Due to the low fiber volume fraction and the loop configuration of fibers, the knitted fabric composites have lower in-plane mechanical properties, so they are not often used as reinforcement. Knit architecture, mechanical properties of warp and weft, matrix properties, fiber volume fraction, and yarn orientation angle are the major parameters that affect the mechanical properties of knitted fabrics (P. Tan, 1997).

Braided fabric composite materials are often characterized by intertwining or orthogonally interlacing three or more threads when they cross one another to form an integral structure. There are two kinds of yarns in this kind of fabric: axial yarns and braided yarns. Generally, sets of parallel axial yarns interconnect with the braided yarns, which follow the  $+\theta$  and  $-\theta$  pattern. The braided fabrics are shown in Figures 1.6 and 1.7 (P. Tan, 1997).



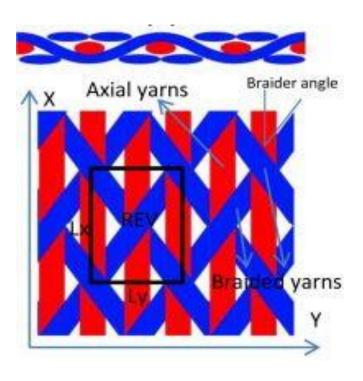


Figure 1. 6: Braided fabrics composite (Hallal, 2013)

This braided fabric structure can help gain higher impact resistance and tolerance. In addition, braided fabrics have better stability and conformability under tension. A braided fabric can be designed for multi-directional conformity. However, under axial compression, it has less stability. Like other types of textile composites, the braid architecture, yarn size and spacing length, fiber volume fraction, fiber orientation angle, and the mechanical properties of the fiber and matrix are the major parameters that affect the mechanical properties of braided fabrics.



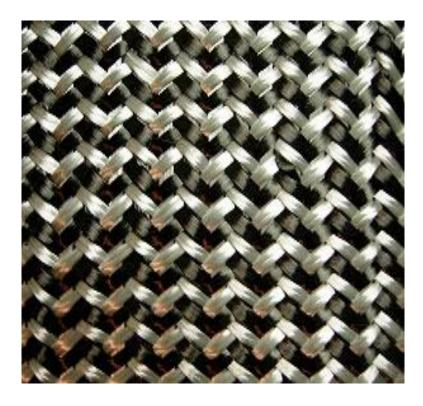


Figure 1. 7: Braided carbon fabrics (A&P Technology, 2013)

### 1.3 Manufacturing of Textile Composites

To manufacture textile composite materials, yarn must first be converted into fabrics. Generally speaking, there are six steps in the process. They are warping, slashing, entering, weaving, heating cleaning, and finishing.

With the machine, these yarns are transferred to the section beams. Then these section beams are consolidated into several sets for the next step. The second step is slashing. It combines the several section beams into a single beam for weaving. This single beam is called a warp beam. During this step, sizing is often used to avoid individual strand abrasion. During the entering step, the warp beam is set up for installation in the loom. This step can arrange and control the warp yarn spreadsheet during the weaving process on the loom. After the step of entering, the warp beam is

ready to be woven in the loom. Then rapier technology or air jet technology is used to interlace the yarns on the loom. The fabric is then wound into a roll or steel drums. The next step is heating cleaning, where the roll or the steel drums are loaded into large ovens and exposed to high temperature. This step can help to remove the binders. Then the pure clean fabrics are produced.

During the final step, some chemical treatments are used to offer good adhesion between the fiber surface and matrix resin. Therefore, this step can make the fabric more stable and provide some chemical protection (Hexcel, 2010).

After the formation of yarns from the fibers, the yarns are woven into the weave fabric. They are then laid up and stitched together and infiltrated with the resin to consolidate in the mold to get the final textile composites. Figure 1.8 shows the steps in the procedure.

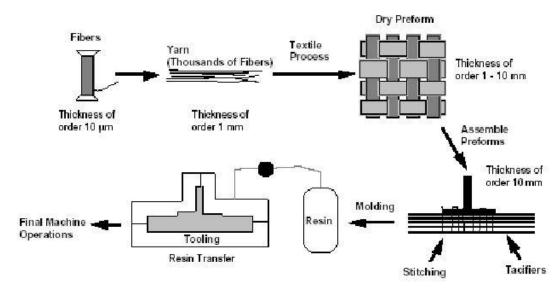


Figure 1. 8: Procedure to manufacture the textile composite (Chretien, 2002)

For the braided fabric composites, the braided fabrics are manufactured by the cylindrical mandrel. The yarns are intertwined to form a tubular fabric. Then, the rotational speed of the yarns is changed so as to get the proper transverse speed of the mandrel to control the braid angle. It is shown in Figure 1.9 (Chretien, 2002).

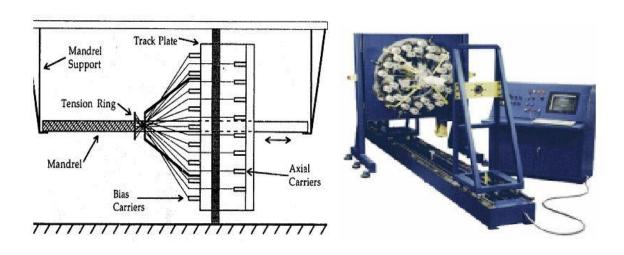


Figure 1. 9: The cylindrical mandrel to manufacture a braided composite (Chretien, 2002)

Traditional composite laminates have no fibers in the through-thickness direction. However, due to their special structure, textile composites gain thickness direction reinforcement by interlacing the yarns. So, compared to traditional composite laminates, textile composites have better impact resistance, higher strength and extensibility, longer fatigue life, and better shear properties.



In summary, textile composites provide good performance and have a low fabrication cost because they can be manufactured on automated machines.

## 1.4 Application of Textile Composites

Interest in the use of composite materials has increased gradually during the last two decades. They can be applied in the aircraft, space structures, automotive, marine, and biomedical industries because of their superior mechanical properties and low cost. Figures 1-10-1.13 show some applications of textile composites in these fields.



Figure 1. 10: The application of textile composites (Wordpress, 2013)

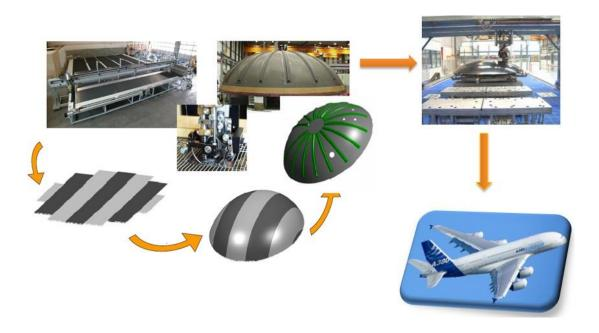


Figure 1. 11: Procedure to manufacture the textile composite pressure bulkhead (Wordpress, 2013)



Figure 1. 12: CFM International new LEAP engine with 18 blades made from 3D woven composite (Composites Manufacturing Online, 2013)





Figure 1. 13: New Tegris baggage made from the textile composite (Core77, 2012)

# 1.5 Literature Review of the Impact on Woven Textile Composites

Interest in the use of composite materials has increased gradually during the last two decades. They can be applied in the aircraft, space structures, automotive, and biomedical fields. Although composite materials have a lot of advanced properties compared to traditional materials, there are still unknowns about their mechanical behavior. One of the major concerns is their behavior under low-velocity impact loading. The impact tests are used to simulate the real impacts on composite structures. Generally, there are two types of impacts: high-velocity impact and low-velocity impact. However, there is not a clear transition between these two categories. Generally, low-velocity impact, impacts occur for impact speeds of less than 10 m/s. To simulate low-velocity impact,



gravity driven machines are used. A weighted indenter falls freely under gravity and then impacts certain composite sample (Abrate, 1998).

Since the impact can occur in the process of manufacturing, normal operations, and maintenance, there are several types of damage that may reduce the structural strength and stability, such as delamination, matrix cracking, and fiber failures (Mathivanan, 2010). The matrix mode is cracking that occurs parallel to the fibers due to tension, compression, or shear; the delamination mode is produced by interlaminar stresses; the fiber mode is tension fiber breakage and compression fiber buckling; and penetration occurs when the impactor completely perforates the impacted surface. It is very important to identify the mode of failure since it is related to the residual strength (Richardson, 1996). Matrix deformation, micro-cracking, and delamination are generally the possible modes of failure in composites subjected to impact loading. Since damage initiates in the form of matrix cracking or delamination, fiber breakage is the final failure during the impact process (Naik, 2000).

Failure mode in composites depends not only on the energy carrying by the impactor, but also velocity and mass. It is known that "a large mass with low initial velocity may not cause the same amount of damage as a smaller mass with higher velocity, even if the kinetic energies of the two masses are exactly the same" (Abrate, 1998). Generally, a larger-massed projectile at a low velocity would cause larger damage in the specimen than a high-velocity low-weight one. If complete penetration is not achieved after impact, the damage type would include delaminations, matrix crack, and fiber failures. The experimental results indicate that delaminations are generated only between plies with different orientations. The area was shaped like a peanut in the direction of the fibers (Abrate, 1998). Figure 1.14 shows the delamination in the composites.



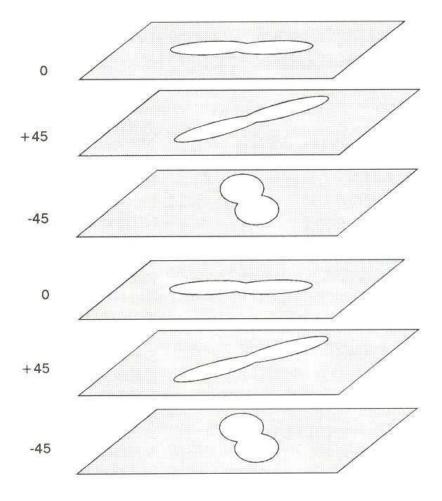


Figure 1. 14: Orientation of delaminations (Abrate, 1998).

Generally speaking, there is a gradual process of damage progression during the impact on the composite material. When delamination occurs, it generates the matrix cracking, which could lead to the fiber failure of the composite material. There are two types of matrix cracks (see Figure 1-15): tensile cracks, which occur under the condition



that the value of the in-plane normal stresses is more than the ply transverse tensile strength in the composite material, and shear cracks, which happen at an angle from the mid-surface(Abrate, 1998).

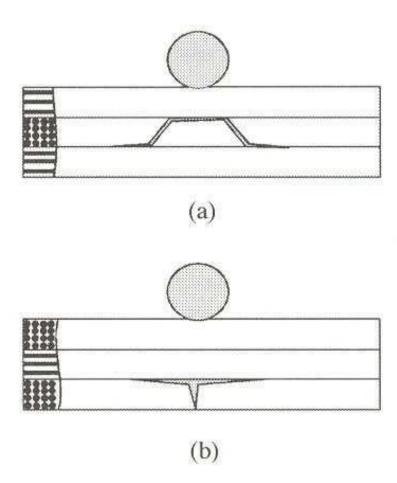


Figure 1. 15: Two types of matrix Cracks (a) Tensile crack (b) Shear crack (Abrate, 1998).



For a thick composite specimen, when the damage occurs at the top surface, it will go down in a pine tree pattern. For a thin composite specimen, the matrix cracks are generated by the bending stresses from the back side of the specimen and make a reverse pine tree pattern as shown in Figure 1.16(Abrate, 1998).

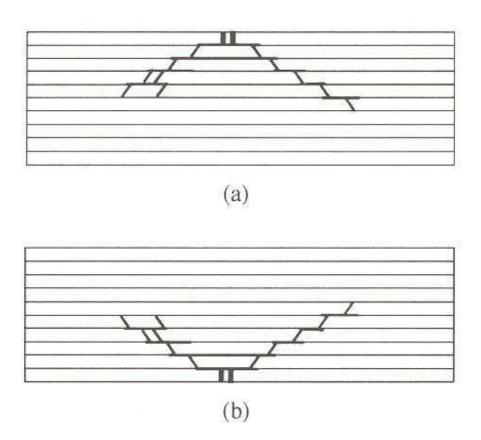


Figure 1. 16: Damage patterns of composite after impact (a) The damage pattern for thick composite (b) The damage pattern for thin composite (Abrate, 1998).



Impact resistance of textile composites has been also extensively studied in the past. In 1985, Winkel and Adams used the instrumented drop weight impact test (DWIT) system to explore impact response differences between balanced-weave fabric laminates and equivalent cross-ply tape laminates. The DWIT system could provide useful insights into the impact behavior of composite materials. The results of the DWIT were strongly dependent on the changes in specimen thickness. They demonstrated smaller post-impact damage areas for graphite and E-glass fabric laminates than for comparable cross-ply laminates. There were no significant damage area differences between Kevlar fabric and cross-ply laminate forms (Winkel, Adams, 1985).

In various reinforced fabric structures with different numbers of layers, it is worth noting that the threshold energy of the major damage occurred when the laminates were subjected to 16 and 24 J/layer nominal impact energies.

In 2003, Shyr researched the impact behavior and damage characteristics in different thickness of laminates. Non-crimp fabric, woven fabric, and discontinuous nonwoven mat (three E-glass fabrics, multiaxial warp-knit blanket, woven fabric, and nonwoven mat) were used to research the efficiency of impact resistance. For the energy-absorbing mechanism, results show that fiber fracture dominated the impact failure model in the thirteen-layer laminate, whereas delamination became more important in the seven-layer laminate. Therefore, it was concluded that the layernumber is an important parameter for the energy-absorbing mechanism in composite laminates. The impact damage absorption energy of laminates varying with the fabric structure was clarified. Due to the impact resistance efficiency, the non-crimp fabric is a valuable option for increasing the impact resistance property of composite laminates (Shyr, 2003).

In 2005, Baucom investigated the progression of damage and the capacity for energy absorption of 2D and 3D woven composite systems and biaxially reinforced warp-knit composite systems subjected to multiple impacts. Until complete perforation occurred, the material response was determined as a function of absorbed energy areal

density and fabric architecture. He used a 3D monolithic orthogonal weave 3TEX style and a 2D plain-weave laminate to investigate the response. The 3D systems survived more strikes before perforating and absorbed more total energy than the 2D laminates. Normalization by areal density confirmed the greater damage tolerance of the 3D systems. This is because 3D reinforcement geometries have unique damage mechanisms. Extensive straining of the z-reinforcement of3D orthogonal weaves was noted. In many cases, these tows were fractured, and surface weft tows were frequently pulled through unbroken crimps of the z-tows. The tensile failure of z-crimps and the frictional sliding of surface weft through z-crimps are new and significant modes of energy dissipation. Manipulation of the relative properties of these enforcements can provide a means of controlling failure evolution in these systems (Baucom, 2005).

In 2005, Hosur studied the low-velocity impact response of woven hybrid composites. His experimental investigations were carried out to fabricate four different combinations of hybrid laminates consisting of twill weave carbon fabric and plain weave S2-glass fabric using a vacuum-assisted resin molding process with an SC-15 epoxy resin system. He compared the response of hybrid laminates with that of carbon/epoxy and glass/epoxy laminates. An instrumented impact testing system at four energy levels of 10, 20, 30, and 40 J was used. Peak load, energy to peak load, time to peak load, deflection at peak load, and absorbed energy were studied by the experimental data. According to his research, hybrid composites exhibited stiffness that was greater than that of S2-glass/epoxy laminates and less than that of carbon/epoxy laminates. By providing S2-glass fabrics on the back surface, the impact response of hybrid laminates can be enhanced because S2-glass fibers have higher strain to failure. This results in delayed fracture of the back surface. Further, the initiation and growth of subsurface damages will be delayed. Damage tolerance of structures can be greatly enhanced by hybridization. Hybrid composite structures with woven carbon and S2-glass layers at the top and bottom



surfaces and unidirectional carbon layers in the inside of the laminate provide optimal inplane properties while enhancing damage resistance and tolerance (Hosur, 2005).

Ballistic impact is normally a low-mass, high-velocity impact by a projectile propelled by a source onto a target. Since ballistic impact is a high-velocity event, the effects on the target can be only near the location of impact. During ballistic impact, energy transfer takes place from the projectile to the target. For ballistic impact problems, there are three basic approaches to analyze :(1) empirical prediction models, which require lot of experimental tests and results, (2) prediction models, which require typical ballistic impact experimental data as input, and (3) analytical models, which take only mechanical and fracture properties and geometry of the target and projectile parameters as input. There are three types of damage mechanisms: (1) the projectile perforates the target and exits with a certain velocity, (2) the projectile partially penetrates the target, and (3) the projectile perforates the target completely with zero exit velocity (Naik, 2005). In Naik's work on the plain weave fabric E-glass/epoxy composite, he studied the effect of various target geometrical and material parameters and projectile parameters. In the ballistic impact event, the kinetic energy of the projectile transferred to the target. The major energy-absorbing mechanisms are deformation of secondary yarns and fracture of primary yarns. The increase in cone surface radius is nearly linear with respect to time and the rate increase of cone depth and height decreases with time. When the impact velocity increases, the contact duration decreases between the projectile and the target. For the same mass, ballistic limit velocity increases when the diameter of the projectile increases. For the same projectile diameter, the ballistic limit velocity decreases as the mass of the projectile increases. For the same projectile mass and diameter, the ballistic limit velocity increases as the target thickness increases (Naik, 2005).

In 2005, Shim researched the effects of impact and laminate parameters on residual mechanical properties such as Young's modulus and failure strength. In his work, the post-impact properties of damaged crowfoot-weave carbon/epoxy laminates are



tested. It was proposed that stresses arising from flexure induced in laminates subjected to low-velocity impact dominate the generation of damage. In this work, a damage severity parameter Q was established to define the degree of damage (Shim, 2005).

$$Q = \sqrt{\frac{m}{h}} v_0 \frac{\ln(\frac{a}{5R} \times 10^2)}{\ln(\frac{a}{5R_S} \times 10^2)}.$$
 (1.1)

Here Q is defined such that the maximum bending stress in a laminate subjected to impact is proportional to it. The mass of a striker is m, and h is the thickness of the plate. The initial velocity is  $v_0$ . The radius of plate is a. R is the impactor tip radius.  $R_s$  can be used as a reference dimension to describe the effect of impactor tip curvature on the bending stress induced in laminates (Shim, 2005). The residual mechanical properties of laminates are linearly dependent on Q. This study demonstrates that theoretical analysis based on impact energy governing impact damage corresponds to a failure criterion that depends on flexural stress. Generally, the impacted damage is assumed as a function of impact energy, but the mechanism has not been explicitly identified. The influence of lay-up on impact damage arises from the mismatch in bending stress between adjacent laminate (Shim, 2005).

In the impact response of woven composite materials, the weaving angles between interlacing yarns can also have some effects on impact characteristics such as peak force, contact duration, maximum deflection, and absorbed energy. The energy absorption capability and perforation threshold of woven composite materials can be significantly improved by using the weaving angle between interlacing yarns. Woven composites with smaller angles, such as 20° and 30°, have slightly lower peak force, larger contact duration, larger maximum deflection, and higher absorbed energy than those with larger weaving angles, such as 75° and 90° (Atas, 2008).



Atas studied the impact response of the woven fabric glass/epoxy composite plates, which were fabricated by the unbalanced plain weave E-glass fabric. Based on an energy profile diagram, Atas reconstructed the damage process of individual woven composite with the curves of contact force-displacement, absorbed energy-time, velocity-displacement, and images of damaged specimens. To assess the damage process after the impact experiment, the impact energy and absorbed energy are the two main parameters. With the examination of the damaged specimens, load-deflection curves, and energy profile diagram, the damage process in composite for various impact energies can be summarized. In his work, the critical damage threshold between matrix cracking and fiber breakage is 11 J. After the impact energy is 23 J, the absorbed energy will have a sudden increase. The woven composite will experience an unstable damage around this point. In this study, the penetration threshold and perforation threshold were also presented. For higher-impact energies resulting in perforation of specimens, it is shown that an "extending method" maybe employed to eliminate post-perforation frictional effects on the energy absorption. It is also stressed that the shape of the energy profile diagram may be affected by factors such as geometry of fibers, thickness and stacking sequence of target, and shape of striker (Atas, 2008).

Experimental results have shown that laminated composites with small laminating angles, such as 15° between adjacent laminas, have a higher energy absorption capability and perforation threshold than the orthogonal counterparts. In 2008, Atas worked on the advantages and disadvantages of using small weaving angles in woven composites focused on the impact response. Based on his study, woven composites with smaller weaving angles like 20° and 30° between interlacing yarns have slightly lower peak force, larger contact duration, larger maximum deflection, and higher absorbed energy than those with larger weaving angles like 75° and 90° (Atas, 2008)

In 2010, Mathivanan studied the low-velocity impact on glass fiber epoxy matrix laminate plates of EP3 grade by two parameters—the saturation impact energy (the

maximum energy bearable by the material without perforation) and the damage degree (the ratio between the total energy transformed (stored and dissipated) and the dissipated part of it)—of a plate specimen subjected to a drop-dart test according to the ASTM D 3029 standard. When subjected to impact at different energy levels, the impactor had three conditions: rebound, stop, and puncture. Based on these three conditions, the glass fiber epoxy matrix laminated plates showed no sensitivity to the strain rate effect because the composite sensitivity to the strain rate is mostly driven by the resin behavior (Mathivanan, 2010).

For the behavior of the plain weave, double- and triple-layer fabric composite structures based on E-glass/epoxy, the perforation threshold was 50 J for plain weave and 60 J for double and triple layer fabric composite structures. The maximum deflection of layer fabrics increased linearly up to the perforation threshold, and after this energy level it increased rapidly for all layer fabrics. The excessive energy of layer fabrics decreased with the increasing impact energy. For compression after impact (CAI) strength, plain weave fabrics were higher than those of double- and triple layer fabrics in the range of 5-22.5 J. But, in the range of 22.5-52.5 J, the triple layer fabrics had the highest CAI strength (Aktas, 2012).

Although there has been a lot of research on the impact behavior of woven composite plates, almost no work has been done on impact and post-impact behavior of layer fabric composites. So, Aktas investigated the impact and post-impact behavior of plain weave (1D), double (2D), and triple (3D) layer fabrics based on E-glass/epoxy at room temperature. The epoxy based on CY225 resin and HY225 hardener was used to manufacture the composite plate. In the low-velocity impact experiment, the perforation threshold was50 J for 1D and 60 J for 2D and 3D. So the perforation threshold of the 2D and 3D layer fabrics was nearly 20% higher than that of 1D. The maximum deflection of layer fabrics increased linearly upto the perforation threshold, and after this energy level it increased rapidly for all layer fabrics. When increasing impact energy, the excessive

energy of layer fabrics decreased. For 1D layer fabric, the absorbed impact energy was lower than 2D and 3D, but the excessive energy was higher. In all layer fabrics, the Compression after impact (CAI) strength decreased, when impact energy increased. The dominant damage mode was delamination and matrix cracking under 25J. The CAI damage generally started around the impact damage and progressed up to edge of the specimens. However, it started from the edge of the specimen up to the impact damage at the penetrated energy level for each layer fabric (Aktas, 2012).

### 1.6 Literature Review of the Imaging Techniques

Damage evaluation due to low velocity impact is an important problem that attracted a lot of attention in the past (Usamentiaga, 2013). During the last decades, different non-destructive evaluation methods have been developed to detect impact damage in composite structures. The most common non-destructive evaluation methods are ultrasonic testing, X-rays, and acoustic emission (Klepka, 2013).

Among these methods, ultrasonic testing is a very common method to detect defects and damage in composite structures. Usually, the traditional ultrasonic scan cannot provide the detailed information about the damage in microstructure of certain materials. In composites, due to their inherent inhomogeneous and orthotropic properties, ultrasonic waves suffer high acoustic attenuation and scattering effect, so that it is difficult to make data interpretation. However, though proper selection of probe, probe parameter settings like pulse width, pulse amplitude, pulse repetition rate and so on, these difficulties can be overcome (Hosur, 1998).

One of the most advanced non-destructive evaluation methods is computed tomography (CT). It has become a familiar technique, mainly due to its medical applications. Computed tomography enables to obtain high resolution three dimensional images of the internal damage in the composites (Fidan, 2012).



Micro-computed tomography (micro-CT) delivers images with micrometer size pixel and widely used in both medical imaging and industrial computed tomography. The application of micro-CT is relatively limited as it requires expertise in X-ray techniques and instrumentation. However, with the development of recent commercial micro-CT systems in the market, the micro-CT technology has been widely used by engineers as a tool to detect damages in composite material structures (Schilling, 2005).

X-ray micro-CT has been applied to a variety of problems in materials research. Generally speaking, the term 'micro-tomography' is used to refer to results obtained with at least 50–100 µm spatial resolution (Stock, 1999).

There has been a number of works related to investigation of microstructures of various composite materials using micro-CT technology. This include studies on fiber location, waviness, fiber breakage, particle distribution, and particle fracture (Schilling, 2005). Most of the studies focused on metal-matrix composites. Fewer studies have been reported on carbon fiber reinforce composites and textile composites. One of the goals of the present thesis is fill out this gap.



## 1.7 Thesis Objectives

The objective of this thesis is three-fold. First is to study the low velocity impact response of layered carbon fiber polymer matrix textile composites subjected to different impact energy levels. Second is to evaluate impact damage in the layered textile composites using computed tomography (CT). Third is to assess and compare capabilities of ZEISS METROTOM 1500 and Siemens MicroCAT II computed tomography scanners for damage evaluation in layered carbon fiber polymer matrix textile composites.

The low velocity impact response of layered carbon fiber polymer matrix five harness satin textile composites was studied using Instron 8200 Dynatup impact tester. A series of impact characterization tests at different impact energy levels were performed to assess impact resistance of the composites. Impacted specimens were, then, evaluated using computed tomography. CT scans were obtained using two different systems, ZEISS METROTOM 1500 and Siemens MicroCAT II. Capabilities of both systems in evaluation of the low velocity impact damage in the layered carbon fiber polymer matrix composites were investigated.



#### CHAPTER 2

#### LOW VELOCITY IMPACT TESTING OF TEXTILE COMPOISTES

### 2.1 Experimental Setup

In this work, an Instron 8200 Dynatup impact tester was used for low velocity impact testing of textile composites. The Instron 8200 Dynatup is designed to test the thin brittle plastics and composites in the numerous standards, like ASTM 3763 and NASA ST-1. Figure 2.1 shows us the Instron 8200 Dynatup impact tester (Dynatup, 2008).

The weight of the cross head of the impact tester can be adjusted from 1.1 to 13.6 Kg (6.7-25 lbs) with the single1.1 Kg (2.4 lbs) increment for the falling carriage. The maximum drop height is 39.37 inch (1 m), which allows to achieve a maximum impact velocity of 4.4 m/s (14.5 ft/sec). The impact energy range is 1.356 to 132.8 Joules (Dynatup, 2008). Instron 8200 impact tester dimension are 90.8 inch (2305 mm) in height, 16 inch (406 mm) in width, and 18 inch (457 mm) in depth. The tester is equipped with two pneumatic self-rebounding stoppers that help to stop the falling carriage to avoid more than one contact of the impactor with a tested specimen. Figure 2.2 shows the two pneumatic self-rebounding stoppers of the tester. The tester is also equipped with a data acquisition system that records the impact load, deflection, absorbed energy, and the duration of impact data. Figure 2.2 shows the two pneumatic self-rebounding stoppers of the tester.





Figure 2. 1: Instron 8200 Impact Tester



Figure 2. 2: Two Pneumatic Self-Rebounding Stoppers

A standard square clamping fixture (Dynatup, 2008) was used in the experiments performed in this study. The specimens were clamped around the entire perimeter with about half of inch. The fixture opening is five by five inches. Figure 2.3 shows the clamping fixture.

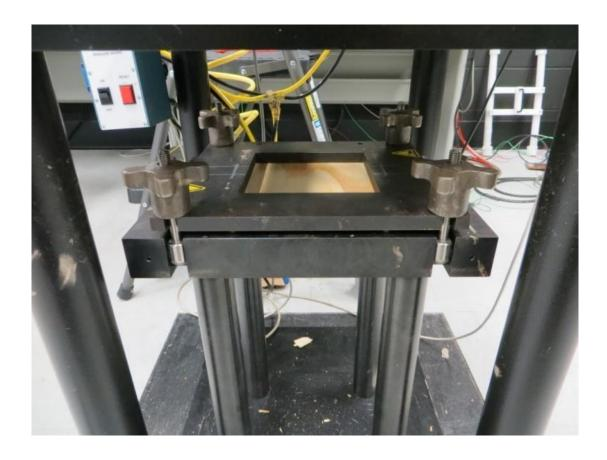


Figure 2. 3: The Clamping Fixture

As said above, Instron 8200 impact tester has a data acquisition system to collect the data. In the middle of the tester, a photo gate is used to activate the data acquisition system. There is a two-pronged flag attached to the falling carriage. The data would begin to be collected when the first prong of the flag brakes the photo gate beam, moreover the flag could also be used to measure the velocity of the falling tup head. The velocity of the falling tup head would be obtained when the prongs of the flag is open so that the beam is unbroken. Thus the velocity that we got is the one that is based on the time when the beam is broken. Before the impact, the photo gate needed to stop at the set position in

order to make the flag to initiate the data collection. Figure 2.4 shows the photo gate and the flag (Dynatup, 2008).

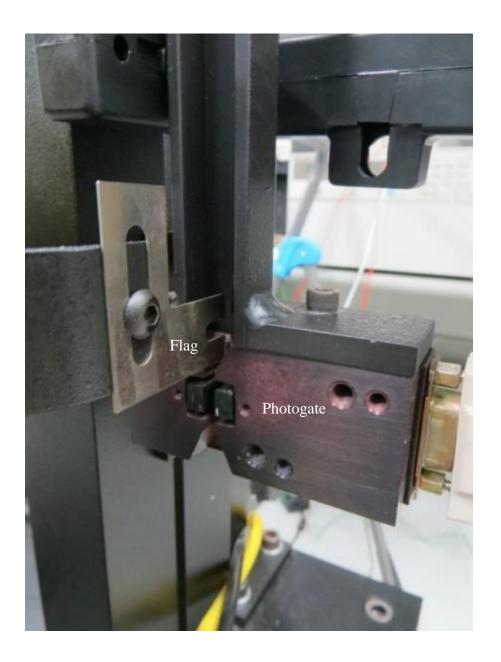


Figure 2. 4: The Photogate and Flag



The Instron 8200 Dynatup impact tester also has an instrumented load cell that is assembled at the bottom of the crosshead, so that the force and the absorption energy could be calculated. There is a tup mounting plate and a strain gage transducer assembled. The striker used in this work had a hemispherical head and diameter of 0.5 inches. Figure 2.5 shows the load cell of the tester (Dynatup, 2008).



Figure 2. 5: Instrumented Load Cell



A signal conditioning box was also assembled for the Instron 8200 Dynatup impact tester. When the flag breaks the photo gate beam, the data signals of the impact load, deflection, absorbed energy and the duration of impact would be transferred to the signal conditioning box and then be transferred to the computer for analysis. The signal conditioning box is two-channel to maintain sampling rates from 1.25 and 5 MHz .It can be used for isolation, signal amplification and direct transducer conditioning functions. The Instron software was installed in the computer to handle all the conditioned signals (Dynatup, 2008). Figure 2.6 shows the signal conditioning box of the tester.



Figure 2. 6: Impact Tester Signal Conditioning Box



An Instron data acquisition software was used to process the data (Dynatup, 2008).

# 2.2 Composite Specimens

In this study a low velocity impact damage of carbon fiber polymer matrix textile composites has been studied. The composite specimens are layered five harness satin composites as seen in Figure 2.7. The laminate is symmetric with orientation of layers in  $0^{\circ}$ ,  $90^{\circ}$ ,  $45^{\circ}$ , and  $-45^{\circ}$  directions. The top and bottom layers are oriented in  $45^{\circ}$  directions, as shown in Figure 2.7



Figure 2. 7: Textile of the Specimen (the arrow indicates a 0° direction)



Square six by six inches specimens were cut from two large panels using a water jet. Dimensions of the original composite panels and cutting layout are shown in Figure 2.8 and Figure 2.9. All dimensions are shown in inches. Note that the panel shown in Figure 2.9 had a hole from the previous impact test on that panel.

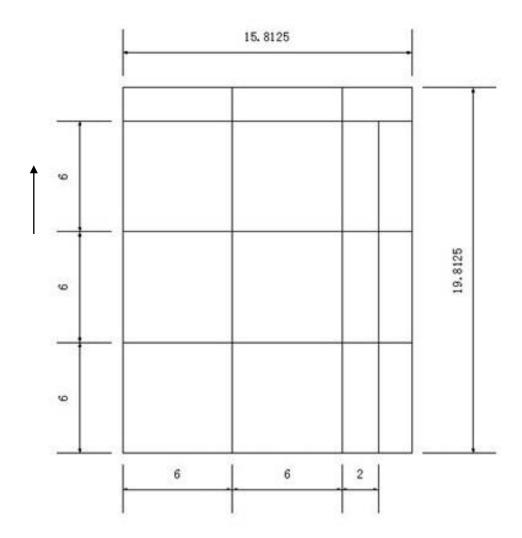


Figure 2. 8: Cutting Layout of Composite Panel 1 (the Arrow Indicates 0° Direction)



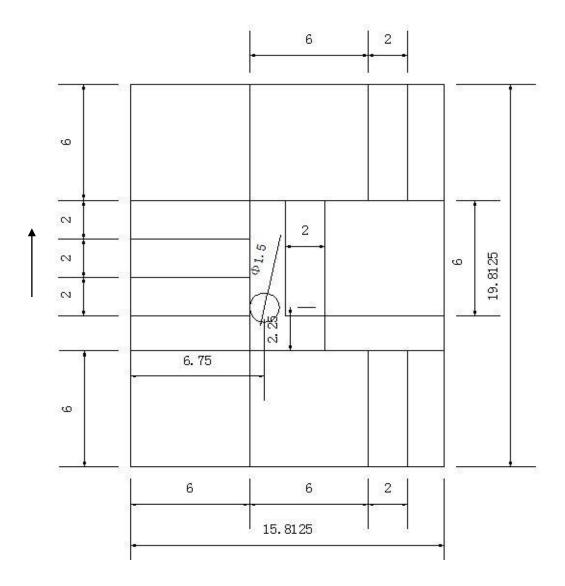


Figure 2. 9: Cutting Layout of Composite Panel 2 (the Arrow Indicates 0° Direction)

Figure 2.10 shows the specimen after cutting. A two number identification system was used to track specimens. The first number represents the panel, from which the specimen was cut, and the second indicates the specimen number. An identification



number and an arrow indicating a 0° direction were written on each specimen. Table 2.1 shows dimensions of each square specimen used in this study.



Figure 2. 10: Impact Test Samples (1-4, 1-5, 1-6)

Table 2. 1: The Measurement of the Specimen

Sample	Average Width (mm)	Average Length(mm)	Average Thickness (mm)
1-4	150.75	152.11	4.57
1-5	149.95	150.83	4.61
1-6	147.90	156.92	4.59
2-4	153.10	153.45	4.50
2-5	153.45	153.36	4.59
2-1	147.57	153.48	4.58
2-2	153.22	153.34	4.54
2-3	153.18	153.53	4.69



## 2.3 ImpactTesting

After clamping the composite specimen in the custom fixture, the tup head was put down to see if it rested on the top surface of the composite specimen correctly. In order to line up the velocity detector, its height was adjusted to the proper position. After that, the rebound brake tower height was adjusted. In this way, it would have an about 0.8 inches (20.32 mm) gap between the top of the compressed rebound brakes and the falling carriage. After that the falling carriage was moved to its drop height position. The compressed air was turn on for the rebound brake system. Then the impact tester signal conditioning box was also turned on and the data acquisition software was open. After importing the specimen identification into the software, click the "next" icon. The impact test was initiated within 30 seconds. Then the release knob was pushed down to release the falling carriage in order to start the low velocity impact test. After the impact, the rebound brakes stopped automatically by the software. All the data from the impulse was saved in the computer for the future analysis. After the test, the power supply was turned off and the impact carriage was lifted back to its drop position.

Eight impact tests were performed at three different impact energy levels. All impact tests produced visible damage on the surface of the specimens. Table 2.2 shows the initial test conditions for each specimen. Table 2.3 shows impact test results. The required height this three different impact energy levels are 0.350 m, 0.411 m, and 0.244 m. The actual height from each specimen is shown in Table 2.2.As one can see all impact tests were performed with the same mass but at different height. The height represents position of the falling weight relatively of the origin of ruler attached to the GRC 8100 Impact Machine column. The direction of the ruler axis is from up to down.



Table 2. 2: Impact Test Conditions

Test #	Mass (kg)	Height (m)	Temperature (°C)	Impact Energy (J)	
1-4	6.69	0.344	20	22.6061	
1-5	6.69	0.343	20	22.5044	
1-6	6.69	0.342	20	22.4770	
2-4	6.69	0.405	20	26.5491	
2-5	6.69	0.400	20	26.2521	
2-1	6.69	0.244	20	15.9917	
2-2	6.69	0.242	20	15.8658	
2-3	6.69	0.247	20	16.2049	

Table 2. 3: Results of the Impact Tests

	Impact	Energy	Total	Impact	Maximum	Time to	Deflection
Sample	energy	to max	penetration	velocity	load (N)	max	at max
	(J)	load (J)	energy (J)	(m/s)		load (s)	load (mm)
1-4	22.6061	16.2252	11.4983	2.5977	7352.8017	8.2275	4.1970
1-5	22.5044	16.6991	11.0278	2.5919	8474.8902	8.1970	4.2844
1-6	22.4770	17.1960	11.4697	2.5903	8319.5370	8.2581	4.3169
2-4	26.5491	20.6971	16.5510	2.8152	9188.2920	8.6853	4.6599
2-5	26.2521	20.2148	14.6525	2.7994	8686.9310	8.6548	4.7464
2-1	15.9917	16.5684	0.3359	2.1849	8032.5135	6.6528	4.3053
2-2	15.8658	15.9191	0.3549	2.1762	7062.6789	6.5613	4.1546
2-3	16.2049	16.6733	5.5965	2.1994	7810.7599	7.0007	4.2750



Figure 2.11 shows variation of the impact load with time for all eight specimens tested. Figure 2.12shows the corresponding variation of the impact load with deflection. Figure 2.13 shows deflection versus time for all eight specimens tested. Figures 2.14-2.22 show impact tests results for the specimens impacted at the same energy levels. Figures 2.23-2.25 show impact tests results for three specimens impacted at three different impact energies.

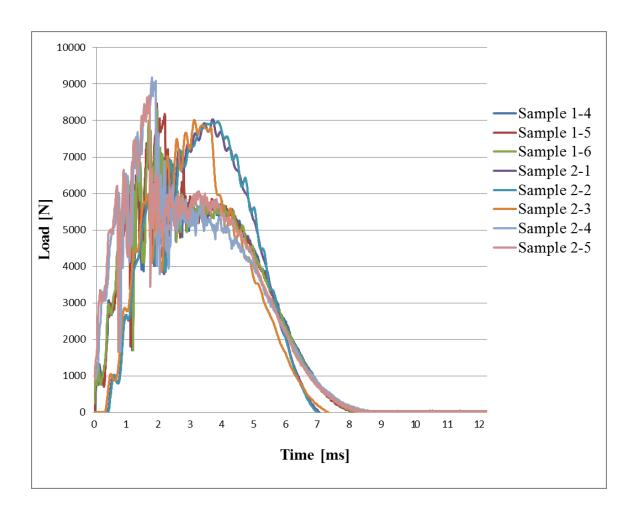


Figure 2. 11: Impact Load vs. Time



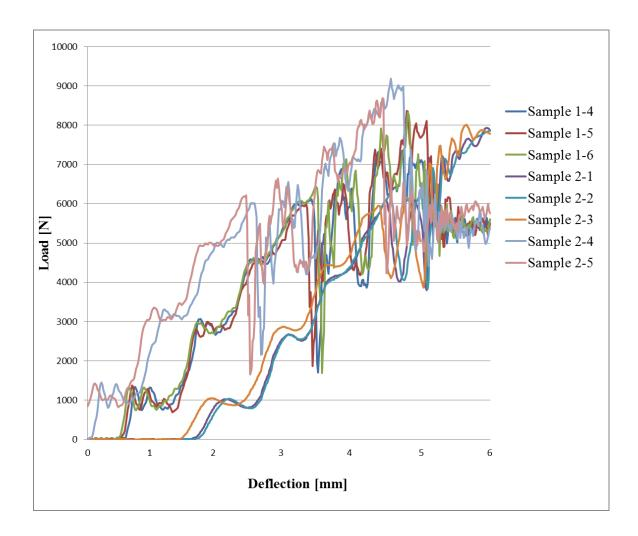


Figure 2. 12: Impact Load vs. Deflection

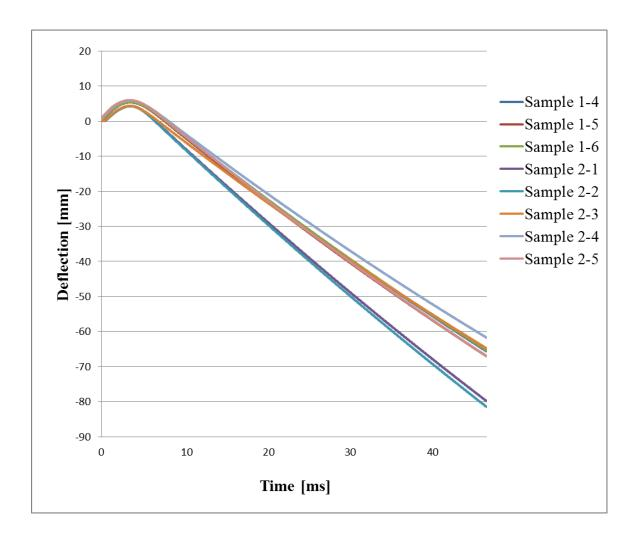


Figure 2. 13: Deflection vs. Time.

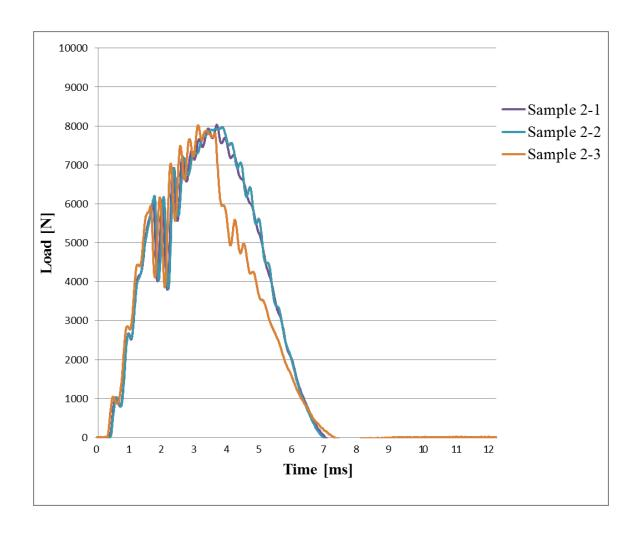


Figure 2. 14: Impact Load vs. Time for the Specimens Impacted at the Lowest Energy, 16 J.

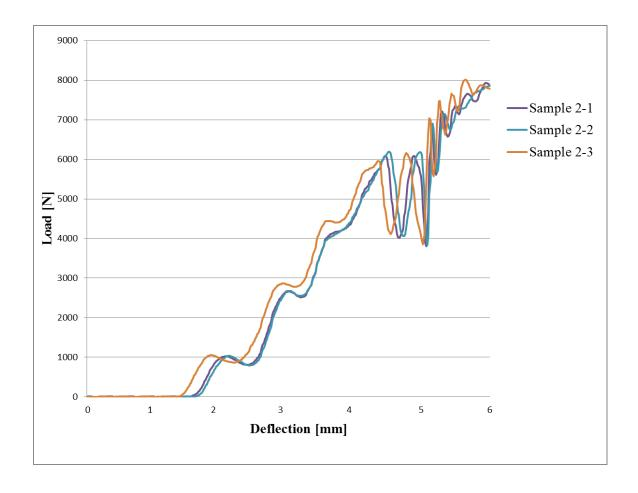


Figure 2. 15: Impact Load vs. Deflection for the Specimens Impacted at the Lowest Energy, 16 J.

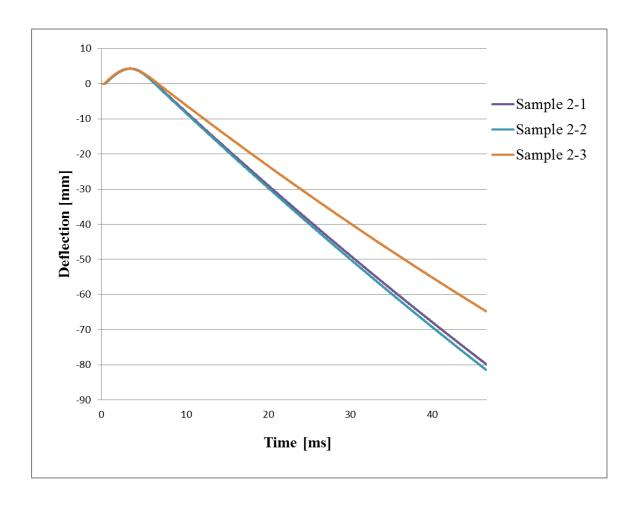


Figure 2. 16: Deflection vs. Time for the Specimens Impacted at the Lowest Energy, 16 J.

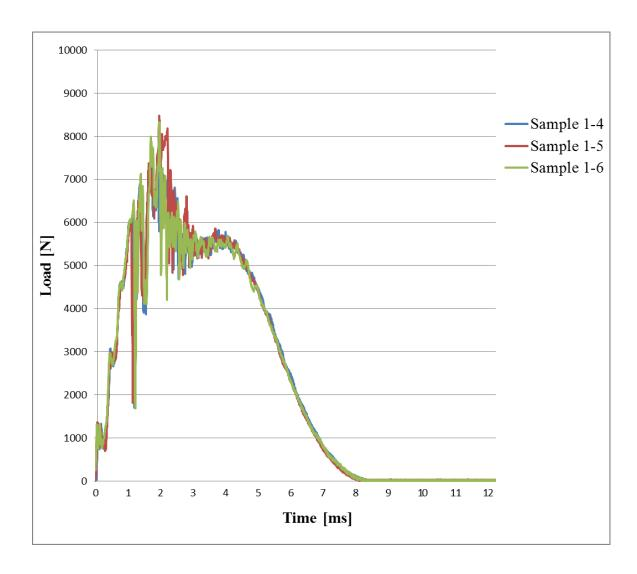


Figure 2. 17: Impact Load vs. Time for the Specimens Impacted at the Intermediate Energy, 22.5 J.

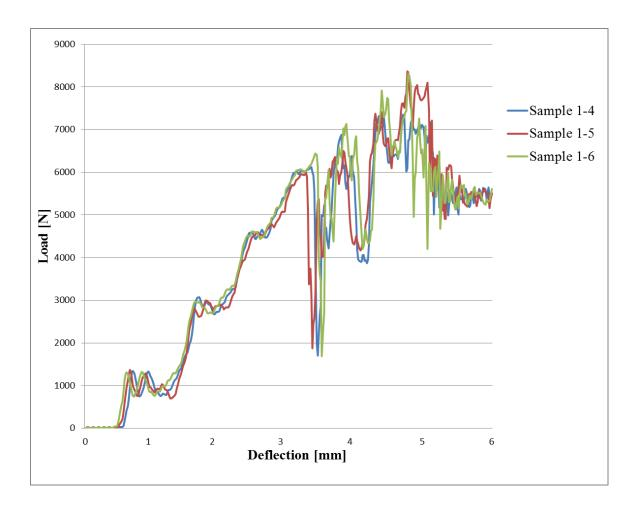


Figure 2. 18: Impact Load vs. Deflection for the Specimens Impacted at the Intermediate Energy, 22.5 J.

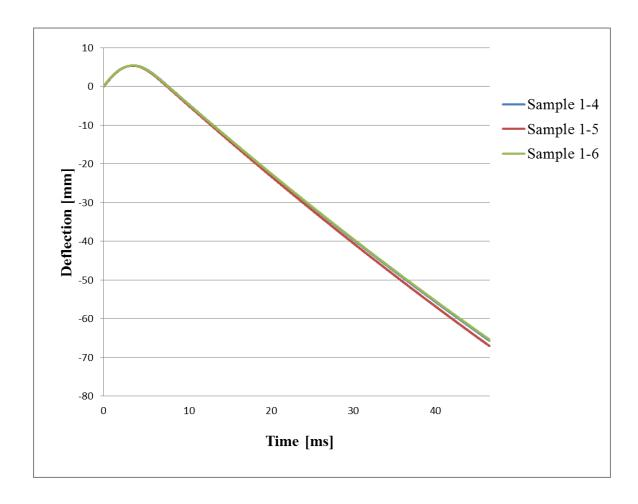


Figure 2. 19: Deflection vs. Time for the Specimens Impacted at the Intermediate Energy, 22.5 J.

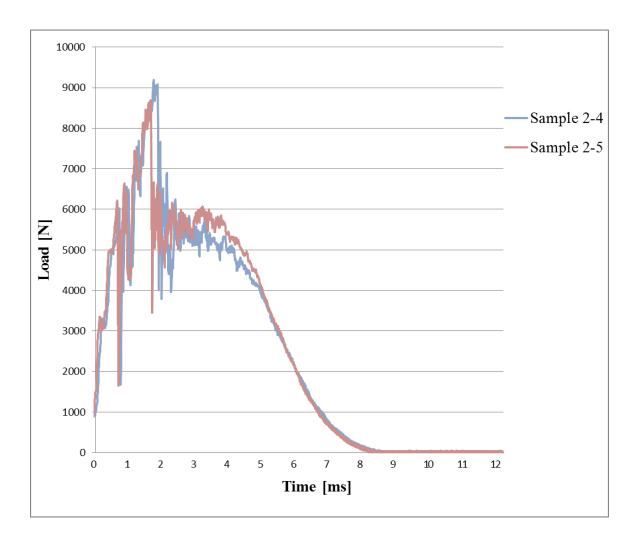


Figure 2. 20: Impact Load vs. Time for the Specimens Impacted at the Highest Energy,  $26\,\mathrm{J}.$ 

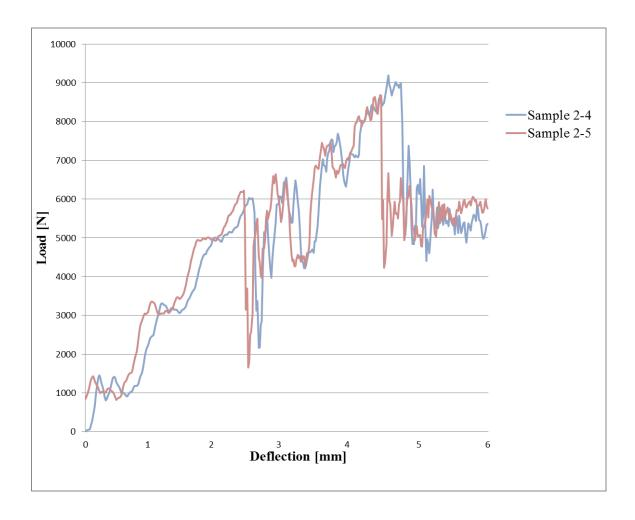


Figure 2. 21: Impact Load vs. Deflection for the Specimens Impacted at the Highest Energy, 26 J.

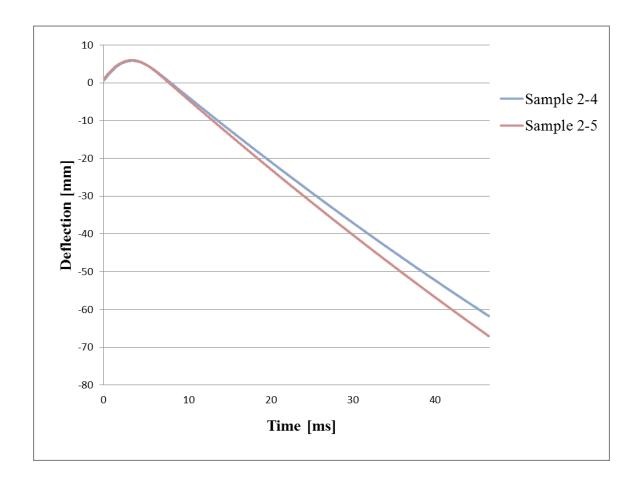


Figure 2. 22: Deflection vs. Time for the Specimens Impacted at the Highest Energy, 26 J.

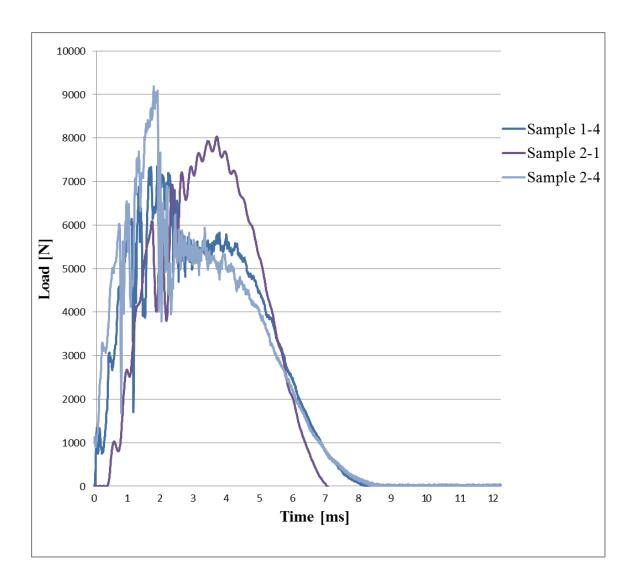


Figure 2. 23: Impact Load vs. Time for Three Representative Specimens.

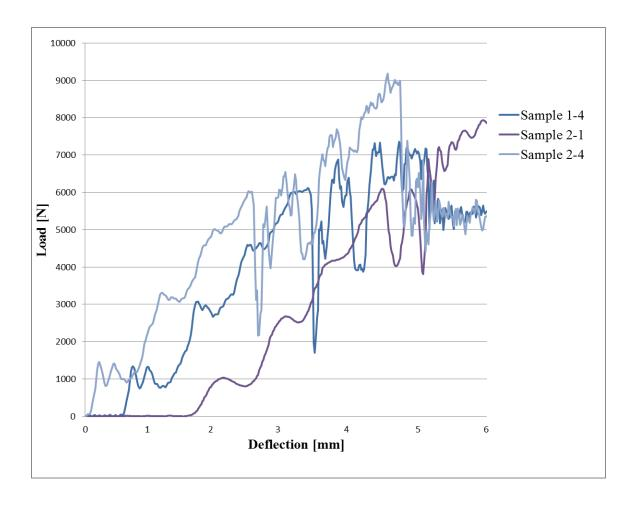


Figure 2. 24: Impact Load vs. Deflection for Three Representative Specimens.

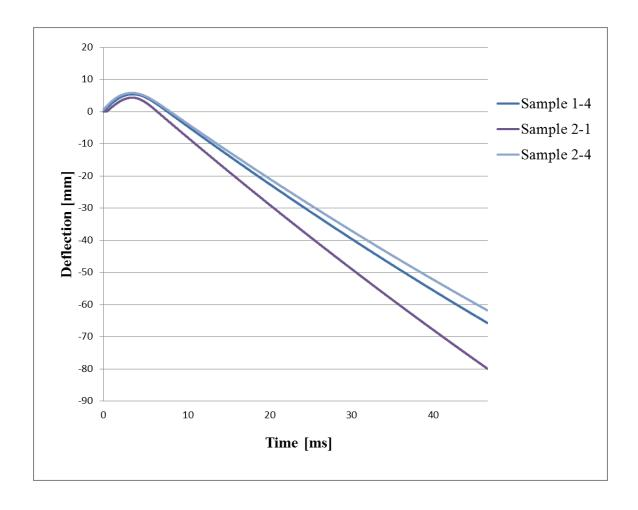


Figure 2. 25: Deflection vs. Time for Three Representative Specimens.

The failure of the specimens impacted at the lowest energy, 16 J, intermediate energy, 22.5 J, and the highest energy, 26 J. can be seen in Figures 2.26, 2.27, and 2.28, respectively. Front side of specimens is shown on the left and back side of specimens is shown on the right. As expected, the size of the damage increases with an increase in the impact energy and more damage is observed on the back size of the specimens than on the front size.



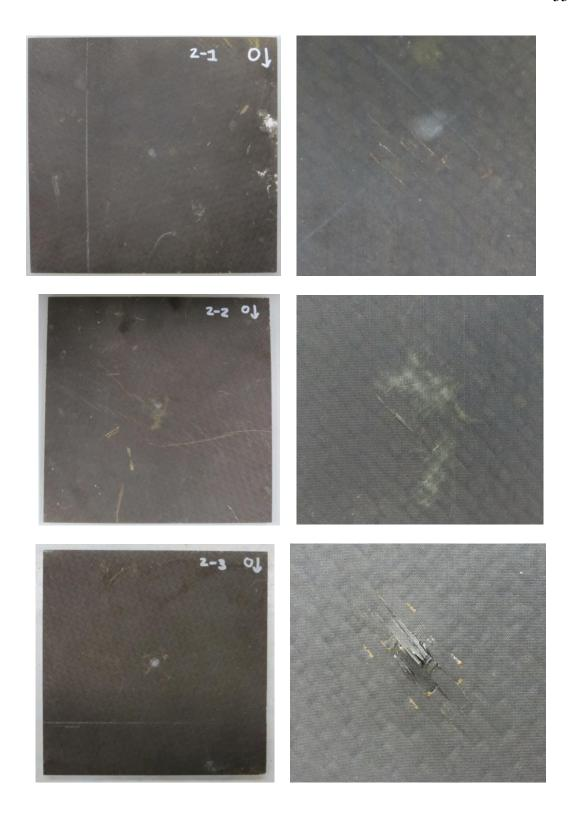


Figure 2. 26: Specimens Impacted at the Lowest Energy, 16 J.



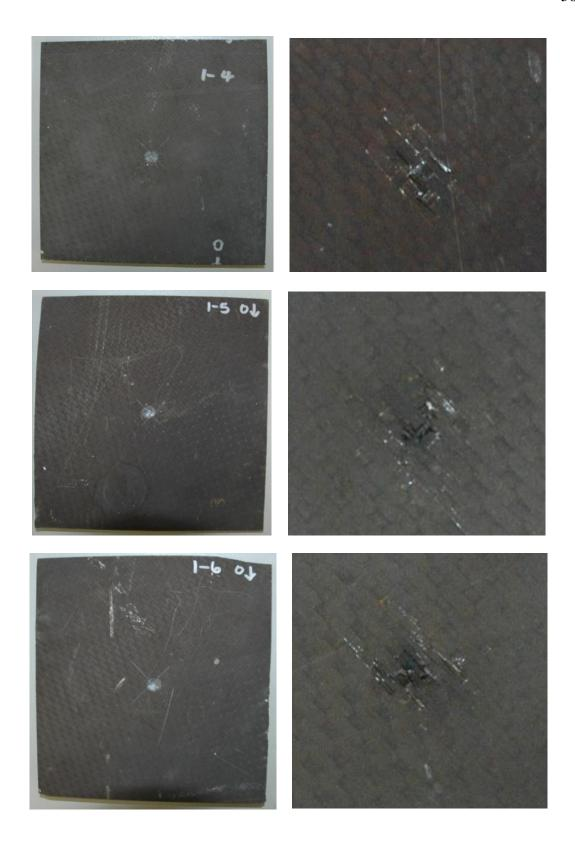


Figure 2. 27: Specimens Impacted at the Intermediate Energy, 22.5.



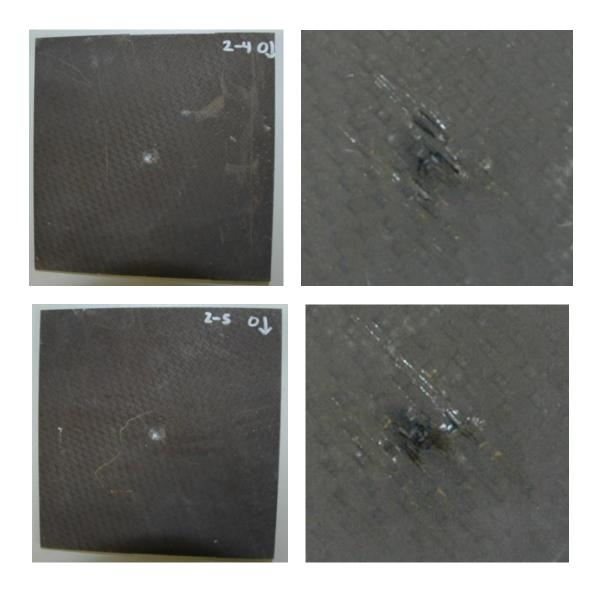


Figure 2. 28: Specimens Impacted at the Highest Energy, 26 J.

### CHAPTER 3

#### CT IMAGEANALYSIS

### 3.1 CT Technology Overview

Computed tomography (CT) is one of the most accurate non-destructive evaluation methods used in industry for evaluation of internal defects. A typical CT scanning process consists of a series of 2D x-ray images with the object rotating 360 degrees or 180 degrees. Figure 3.1 shows the general operation of the modern industrial CT system (Makeev 2010).

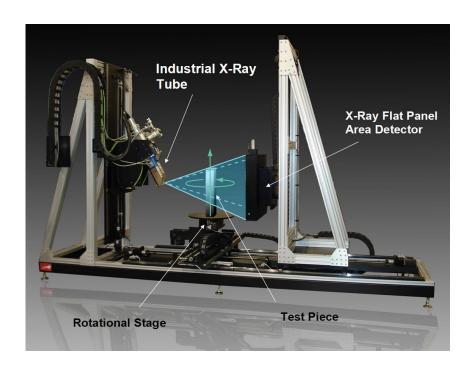


Figure 3. 1: General Operation and Major Components of the Modern Industrial CT System (Makeev 2011)



A typical CT system acquires between 120 and 3600 digital images, depending on the desired resolution. The size of the images is from 3 to 10 megapixels. When the scanning process is finished, CT reconstruction algorithms are used to generate the 3D volumetric information. Time required for image reconstruction has been significantly reduced in recent years with the assistance of advancements in the fast CT reconstruction software and computer hardware. A CT image is usually called a slice. A typical digital image is composed of pixels, whereas a CT slice is composed of voxels. The slice corresponds to a certain thickness of the object being scanned. A volumetric representation of the object being scanned is obtained by acquiring a contiguous set of CT slices (Richard, 2012). When using CT technology, a grayscale image is usually obtained. It carries only intensity information of the object being scanned. Images of this sort are composed exclusively of shades of gray that range from black to white when the intensity of object varies from weakest to strongest (Stephen, 2006). This is because the gray levels correspond to X-ray attenuation when the CT slice image is obtained. The gray level reflects the proportion of X-ray scattered or absorbed when it passes through each voxel of the object (Richard, 2012). Figure 3.2 shows a multi-scale CT scan of aerospace-grade material. Changes in the gray level in the CT images allow one to see the shape, structure, and internal structure of the material.



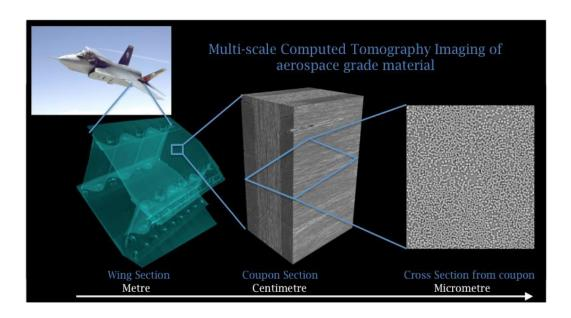


Figure 3. 2: Multi-scale Computed Tomography of Aerospace-Grade Material (Anna, 2012)

In this thesis, impact damage in the layered textile composites was evaluated using the ZEISS METROTOM 1500 and Siemens MicroCAT II computed tomography systems. The capabilities of these CT systems are discussed in the next sections.

## 3.2 ZEISS METROTOM 1500 Computed Tomography

Scanner and Image Analysis Software

The ZEISS METROTOM 1500 is an industrial CT scanner produced by Carl Zeiss AG, a German manufacturer of industrial measurement systems. The CT images were reconstructed using VGStudio MAX.

Carl Zeiss is known for introducing the term "metro tomography" to describe the fusion of metrology and tomography into a new technology. The superior total system



METROTOM 1500 computer tomography is built by Carl Zeiss to generate and evaluate high-quality 3D image data.

In the METROTOM 1500 system, the measuring, inspection processes, and objectification of measuring results are automatic. The METROTOM 1500 system is often used for inspection of new lightweight materials. It also can be applied to precisely measure the smallest parts and mounted components like ESP sensors and electric toothbrushes. With the METROTOM 1500 system, coordinate measuring and non-destructive inspection can be achieved. The system can also help to optimize the volume production processes for precision-manufactured and injection-mold work pieces in industries (Lettenbauer, 2007). Figure 3.3 and Figure 3.4 show the ZEISS METROTOM 1500 system and its internal structure.





Figure 3. 3: ZEISS METROTOM 1500 System (Lettenbauer, 2007)



Figure 3. 4: ZEISS METROTOM 1500 System Internal Structure (Lettenbauer, 2007)

In this work, the CT images were created from the Volume Graphics products. The Volume Graphics product line for industrial and scientific computed tomography consists of three software applications: VGStudio MAX, VGStudio, and MyVGL. VGStudio MAX is the most comprehensive tool, enabling the user to analyze, measure, segment, and compare voxel data sets. VGStudio is the inexpensive entry-level product that is the world-wide standard of industrial and scientific voxel data processing and visualization. VGStudio can be upgraded to VGStudio MAX and can therefore grow with



users' requirements for advanced analysis tools. Finally, MyVGL is the 3D viewer that can be installed on any standard PC for presenting projects created using VGStudio and VGStudioMAX (VGStudio MAX 2.2, 2013).

In this analysis, VGStudio MAX 2.2 was employed. Then, My VGL 2.2 was used for the CT reconstruction and analysis. MyVGL is a software package for the visualization and documentation of voxel data projects (.vgl files) created in VGStudio MAX 2.2 or VGStudio 2.2. It has been used in a variety of application areas, such as industrial CT, medical research, life sciences, and many others (My VGL 2.2, 2013).

With the assistance of this software, the 3D volume inside the sample can be visualized. In addition, it provides the windows to detect the sample defects from the x, y, and z directions. The directions of each scan plane are shown in Figure 3.5.



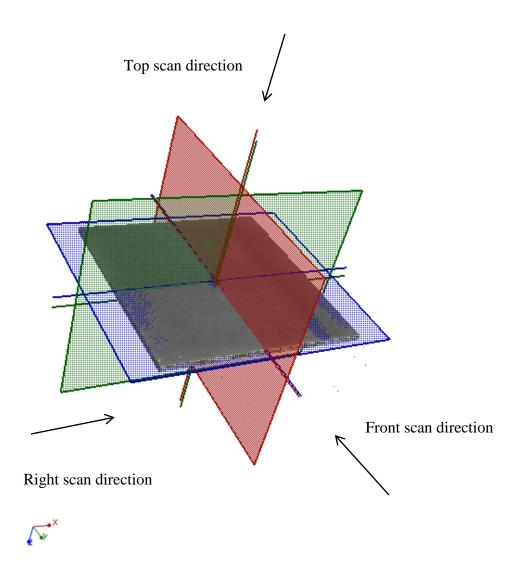


Figure 3. 5: Scan Direction of Each Scan Plane

## 3.3 Siemens MicroCAT II Computed Tomography Scanner and Image Analysis Software

A Siemens MicroCAT II scanner was also used in this work. The Siemens MicroCAT II was designed to scan small animals. After adjusting the detector and the X-ray source, image resolution can be from 27 microns to 100 microns. The CT images from the Siemens MicroCAT II are of superb modality for visualizing and quantifying the bone and tissue of small rodents (MicroCAT II, 2014).

By rotating the X-ray detector and sources, the object is scanned, and Micro-CT images are acquired (MicroCAT II, 2014). The MicroCAT II scanner that was used in this work has an X-ray source with maximum operating energies of 140 kVp and 500 micro-amperes. During high-magnification scanning, high photon flux is provided by the X-ray source with large cone-beam angles in order to improve spatial resolution. The small-pixel CCD detector provides isotropic resolution of 28 microns at an image size of  $1536 \times 1536 \times 1024$  pixels at a binning of 2. In other words, it can go as low as 14 micron resolution, but due to increased image noise in most specimens, the 28 micron resolution was set. With the Siemens software, the reconstructed images can be easily transferred and visualized. The scanner and reconstructed image are shown in Figures 3.6 to 3.8



Figure 3. 6: Siemens MicroCAT II Scanner (MicroCAT II, 2014)



Figure 3. 7: The Scanner Bed in the Siemens MicroCAT II Scanner (MicroCAT II, 2014)

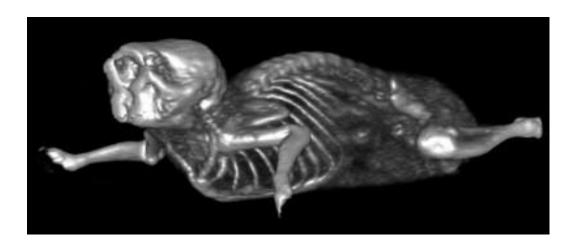


Figure 3. 8: 3D Rendering CT Scan of a Mouse from the Siemens MicroCAT II Scanner (MicroCAT II, 2014)



### 3.4 CT Results

This section presents analysis of CT images of the impacted textile composites described in Chapter 3. The images were obtained using ZEISS METROTOM 1500 and Siemens MicroCAT II computed tomography systems.

3.4.1 ZEISS METROTOM 1500 CT Results for the Specimens Impacted at the Lowest Impact Energy

In this section, CT scans of the textile composite samples 2-1, 2-2, and 2-3 impacted at the lowest impact energy, 16 J, are discussed. The CT scans were obtained using a ZEISS METROTOM 1500 CT scanner.

When using ZEISS METROTOM 1500 CT scanner, a grayscale image with intensity information of the object is obtained. Because the gray level reflects the proportion of X-ray scattered or absorbed when it passes through each voxel of the object, adjusting the opacity manipulation area in software, the different parts of object will be observed. Figure 3.9 shows gray-values setting of human head.



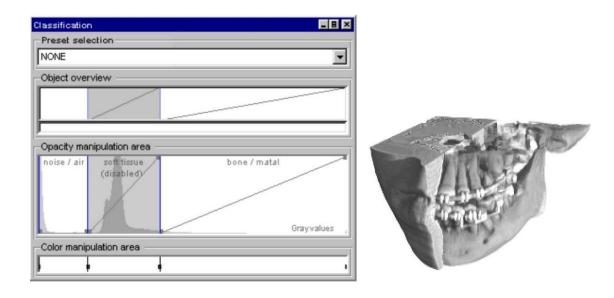


Figure 3. 9: Gray-Values Setting of Human Head.

When analyzing the ZEISS METROTOM 1500 CT results, the gray scale values of the undamaged areas and noise air were set into blue. The gray scale values of the damage area was set into yellow. Figure 3.10 shows the gray values setting.



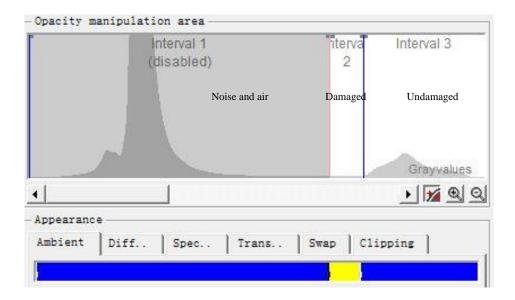


Figure 3. 10: Gray-Values Setting of samples scanned using the ZEISS METROTOM 1500.

Figures 3.11-3.26 show damage zones at different depths from the impacted surface of samples 2-1, 2-2, and 2-3. As one can see, damage was detected inside the samples at about 2 mm depth from the impacted surface. Sample 2-3 received the largest damage. This was confirmed by the analysis of the surfaces of the samples (see Figure 2-26).



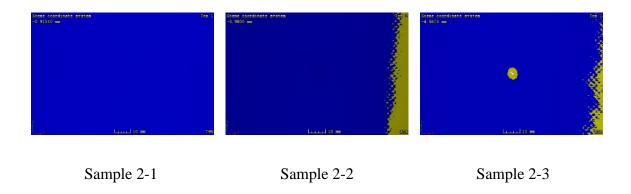


Figure 3. 11: CT image at the plane located 0.22 mm away from the impacted surface

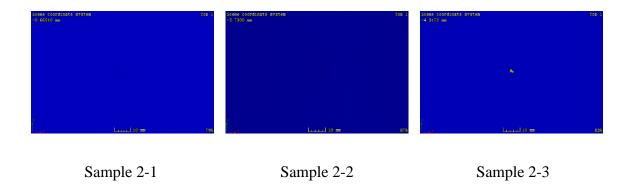


Figure 3. 12: CT image at the plane located 0.47 mm away from the impacted surface

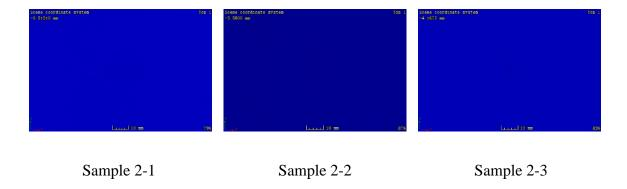


Figure 3. 13: CT image at the plane located 0.62 mm away from the impacted surface



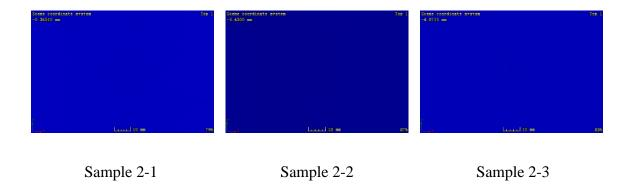


Figure 3. 14: CT image at the plane located 0.77 mm away from the impacted surface

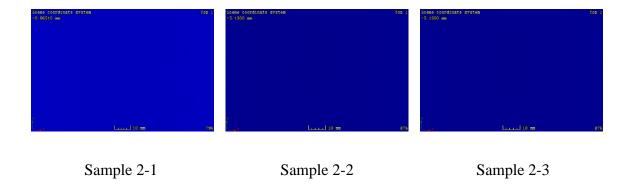


Figure 3. 15: CT image at the plane located 1.07 mm away from the impacted surface

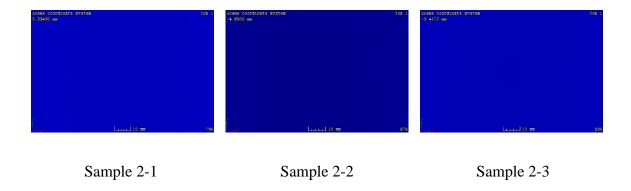


Figure 3. 16: CT image at the plane located 1.37 mm away from the impacted surface



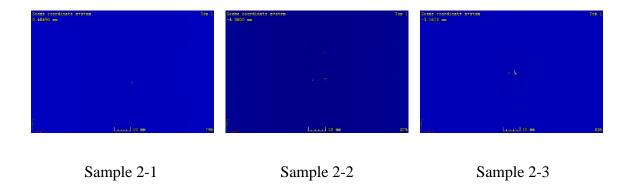


Figure 3. 17: CT image at the plane located 1.62 mm away from the impacted surface

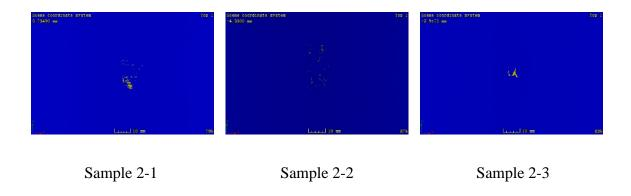


Figure 3. 18: CT image at the plane located 1.87 mm away from the impacted surface

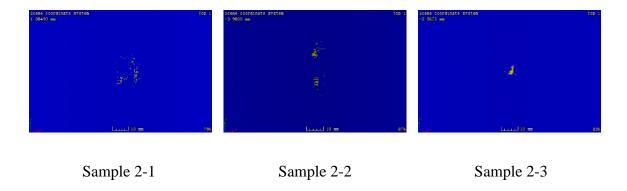


Figure 3. 19: CT image at the plane located 2.22 mm away from the impacted surface



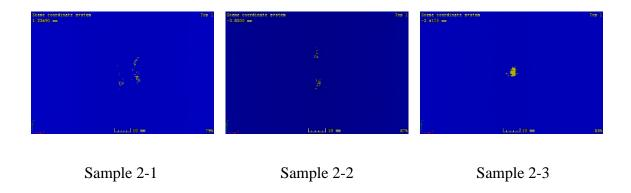


Figure 3. 20: CT image at the plane located 2.37 mm away from the impacted surface

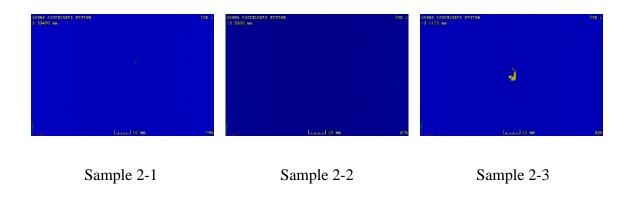


Figure 3. 21: CT image at the plane located 2.67 mm away from the impacted surface



Figure 3. 22: CT image at the plane located 2.92 mm away from the impacted surface





Figure 3. 23: CT image at the plane located 3.12 mm away from the impacted surface

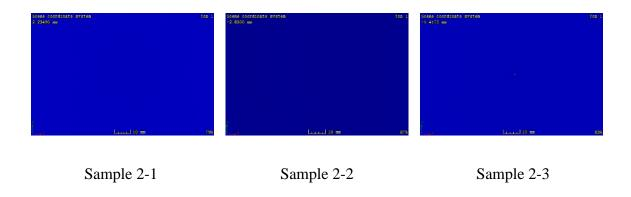


Figure 3. 24: CT image at the plane located 3.37 mm away from the impacted surface



Figure 3. 25: CT image at the plane located 3.57 mm away from the impacted surface



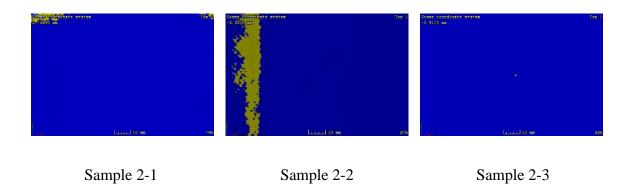


Figure 3. 26: CT image at the plane located 3.87 mm away from the impacted surface

A detailed discussion of the CT scanning process and image analysis of samples 2-1, 2-2, and 2-3 is given in Appendix A.

# 3.4.2 ZEISS METROTOM 1500 CT Results for the Specimens Impacted at the Intermediate Impact Energy

In this section, the results of the image analysis of CT scans of the specimens impacted at the intermediate impact energy, 22.5 J, are discussed. The CT scans were obtained using a ZEISS METROTOM 1500 CT scanner. Figures 3.27-3.42 show damage zones at different depths from the impacted surface. As one can see, the damage in the samples impacted at the energy level of 22.5 J was present through the entire thickness of the samples. Moreover, the damage zone size increased with depth.



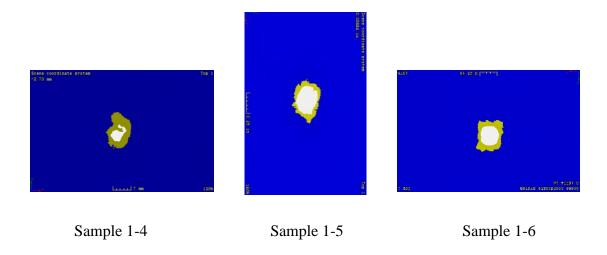


Figure 3. 27: CT image at the plane located 0.22 mm away from the impacted surface

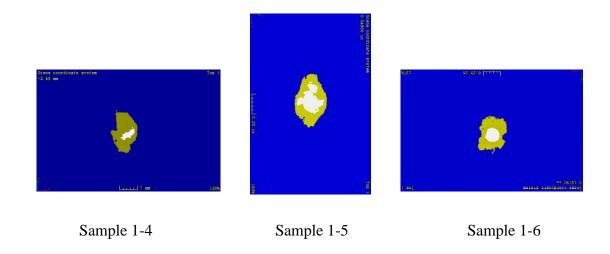


Figure 3. 28: CT image at the plane located 0.47 mm away from the impacted surface

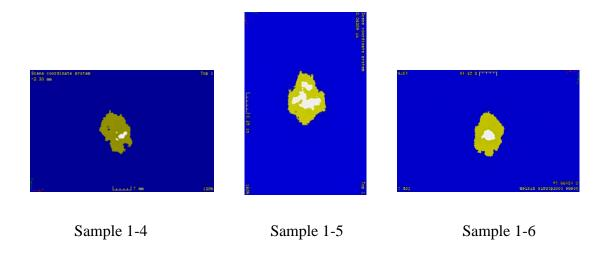


Figure 3. 29: CT image at the plane located 0.62 mm away from the impacted surface

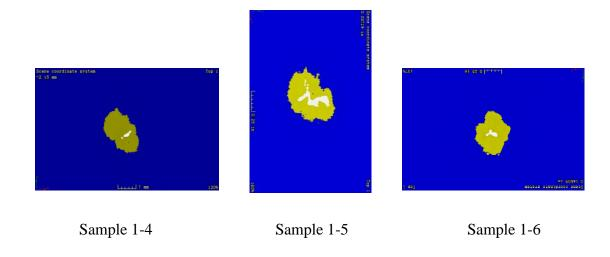


Figure 3. 30: CT image at the plane located 0.77 mm away from the impacted surface

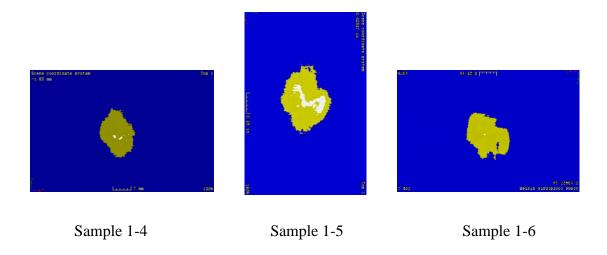


Figure 3. 31: CT image at the plane located 1.07 mm away from the impacted surface

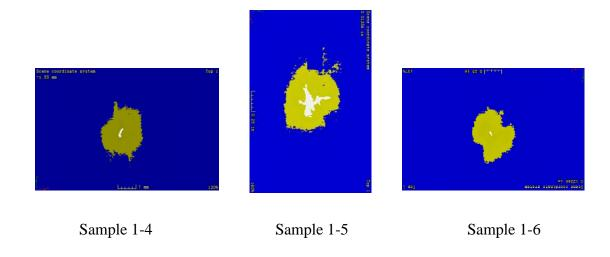


Figure 3. 32: CT image at the plane located 1.37 mm away from the impacted surface

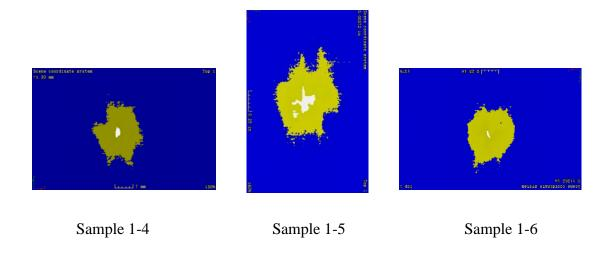


Figure 3. 33: CT image at the plane located 1.62 mm away from the impacted surface

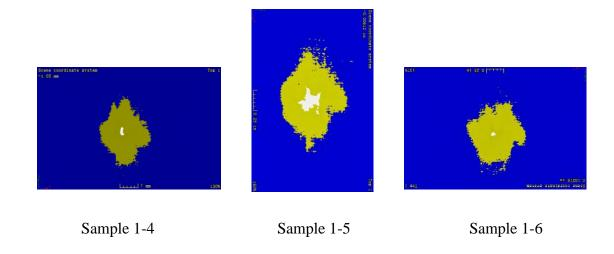


Figure 3. 34: CT image at the plane located 1.87 mm away from the impacted surface

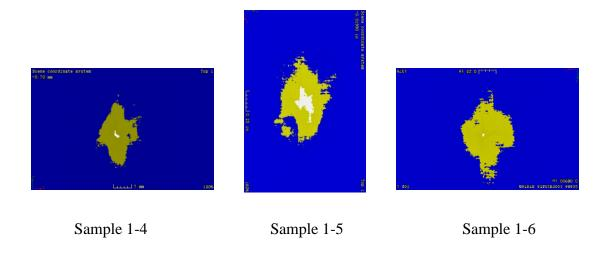


Figure 3. 35: CT image at the plane located 2.22 mm away from the impacted surface

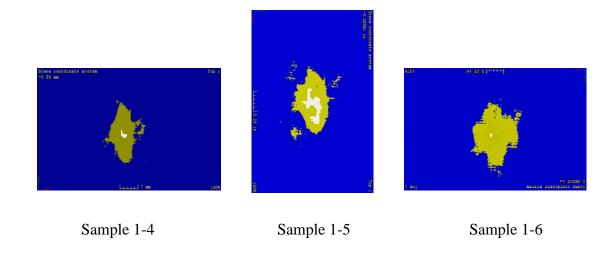


Figure 3. 36: CT image at the plane located 2.37 mm away from the impacted surface

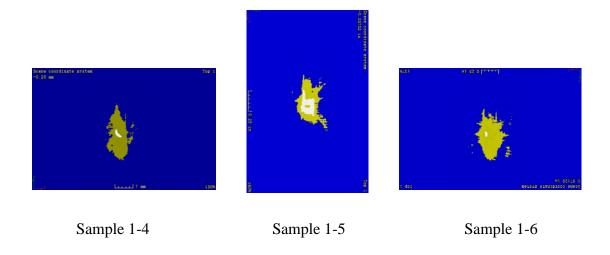


Figure 3. 37: CT image at the plane located 2.67 mm away from the impacted surface

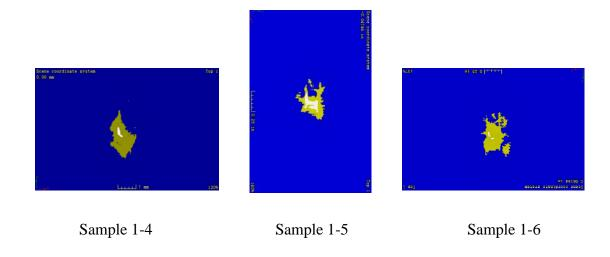


Figure 3. 38: CT image at the plane located 2.92 mm away from the impacted surface

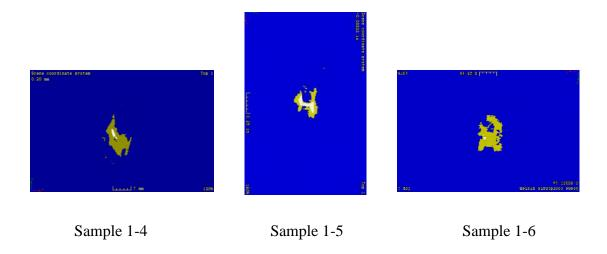


Figure 3. 39: CT image at the plane located 3.12 mm away from the impacted surface

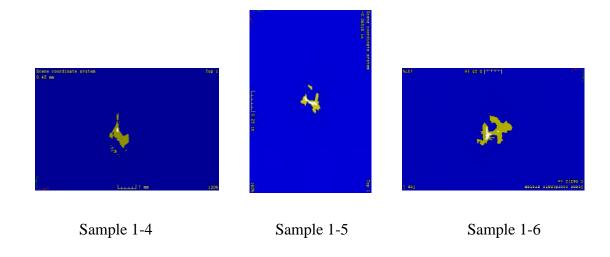


Figure 3. 40: CT image at the plane located 3.37 mm away from the impacted surface

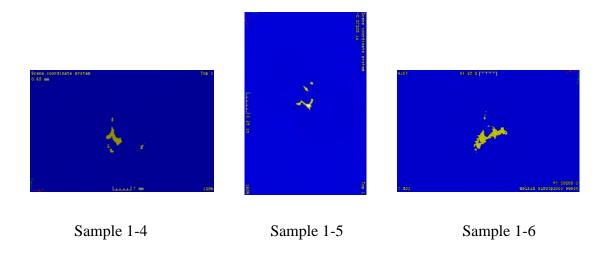


Figure 3. 41: CT image at the plane located 3.57 mm away from the impacted surface

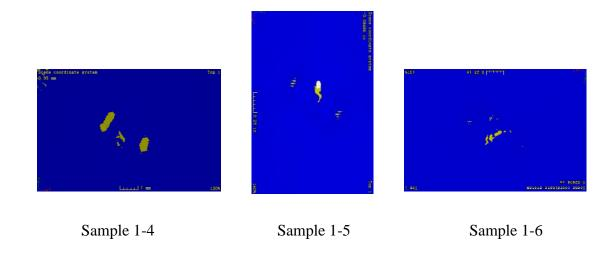


Figure 3. 42: CT image at the plane located 3.87 mm away from the impacted surface

In sample 1-4, the damage zone reached maximum size at the depth of 2.17 mm away from the impacted surface. Note that the thickness of sample 1-4 was 4.57 mm. The size of the largest damage area was measured by the software MyVGL and was 26.37



mm (see Fig. 3.43; the arrow at the left indicates the 0° orientation). It is also worth noticing that the orientation of the damage zone changes with depth. This is due to the fact that the tested samples are laminated composites that have multiple lamina of various orientations, i.e., 45°, -45°, 0°, and 90°.

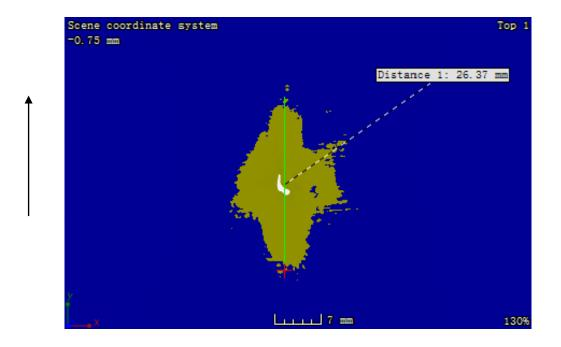


Figure 3. 43: CT image at the plane with the largest damage size in sample 1-4 (located 2.17 mm away from the impacted surface)

In sample 1-5, the damage zone reached maximum size at the depth of 1.87 mm away from the impacted surface. Note that the thickness of sample 1-5 was 4.61 mm. The



size of the largest damage area was measured by the software MyVGL and was 33.31 mm (see Fig. 3.44; the arrow at the top indicates the 0° orientation).

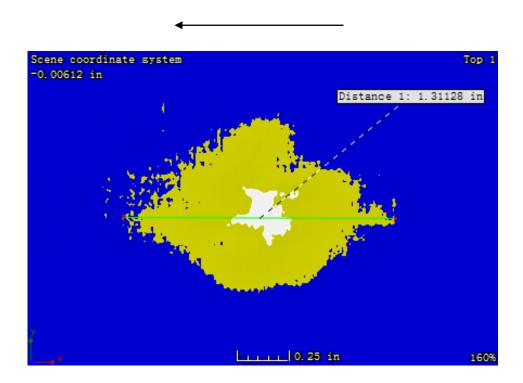


Figure 3. 44: CT image at the plane with the largest damage size in sample 1-5 (located 1.87 mm away from the impacted surface)

In sample 1-6, the damage zone reached maximum size at the depth of 2.22 mm away from the impacted surface. Note that the thickness of sample 1-6 was 4.61 mm. The size of the largest damage area was measured by the software MyVGL and was 36.38 mm (see Fig. 3.45; the arrow at the left indicates the 0° orientation).



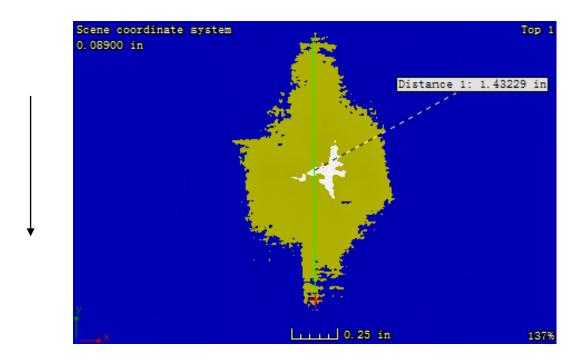


Figure 3. 45: CT image at the plane with the largest damage size in sample 1-6 (located 2.22 mm away from the impacted surface)

Therefore, the maximum measured damage in sample 1-4 is smaller than in samples 1-5 and 1-6. The maximum measured damage in samples 1-5 and 1-6 are similar. This observation corresponds well with the maximum impact load and deflection at the maximum impact load (see Table 2.3). The maximum impact load and deflection at the maximum impact load in sample 1-4 were lower than in samples 1-5 and 1-6, in which the maximum impact load and deflection were similar. It is also worth noting that the impact energy in sample 1-4 was slightly higher than in samples 1-5 and 1-6. Further results for the impact damage size at the different depths in samples 1-4, 1-5, and 1-6 are



shown in Table 3.1. The measurements in the vertical direction (see Figs. 3.27-3-42) are shown.

Table 3. 1: Damage size at different depths away from the impact surface with intermediate impact energy

Depth	Sample 1-4 Damage size	Sample 1-5 Damage size	Sample 1-6 Damage size
(mm)	(mm)	(mm)	(mm)
0.22	14.31	9.89	12.34
0.47	16.02	16.91	14.51
0.62	17.11	17.13	16.52
0.77	17.51	17.31	17.19
1.07	19.18	21.05	17.65
1.37	20.97	21.12	21.38
1.62	21.31	25.88	21.65
1.87	25.42	33.05	26.54
2.22	24.73	27.30	36.38
2.37	22.79	21.01	29.41
2.67	20.94	15.07	20.26
2.92	18.79	12.81	17.00
3.12	15.68		15.04
3.37	13.63		
3.57	10.91		
3.87			

The detailed discussion of the CT scanning process and image analysis of samples 1-4, 1-5, and 1-6 is given in Appendix B.

## 3.4.3 ZEISS METROTOM 1500 CT Results for the Specimens Impacted at the Highest Impact Energy

In this section, the results of image analysis of CT scans of the samples impacted at the highest impact energy, 26 J, are discussed. The CT scans were obtained using a ZEISS METROTOM 1500 CT scanner. Figures 3.46-3.61 show damage zones at different depths from the impacted surface of samples 2-4 and 2-5. As one can see, the highest impact energy produced the largest damage that was detectable through the thickness of the samples, and the extent of the damage zone increased with depth.

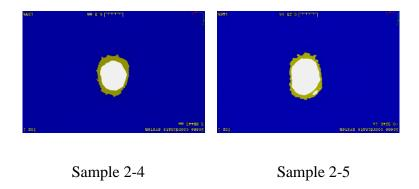


Figure 3. 46: CT image at the plane located 0.22 mm away from the impacted surface

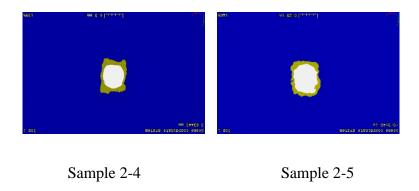


Figure 3. 47: CT image at the plane located 0.47 mm away from the impacted surface

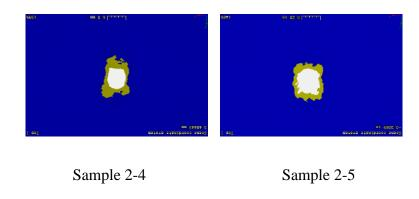


Figure 3. 48: CT image at the plane located 0.62 mm away from the impacted surface

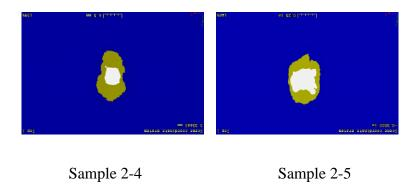


Figure 3. 49: CT image at the plane located 0.77 mm away from the impacted surface

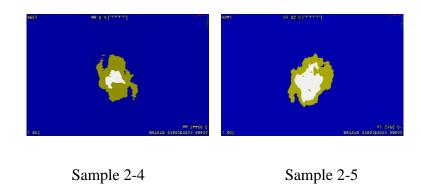


Figure 3. 50: CT image at the plane located 1.07 mm away from the impacted surface

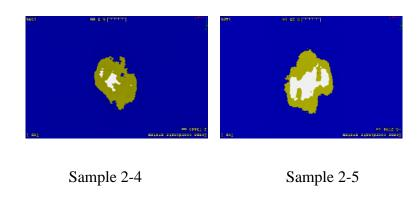


Figure 3. 51: CT image at the plane located 1.37 mm away from the impacted surface

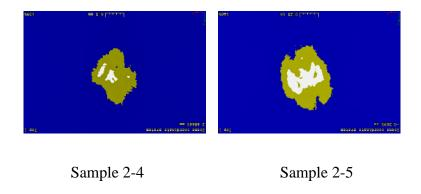


Figure 3. 52: CT image at the plane located 1.62 mm away from the impacted surface

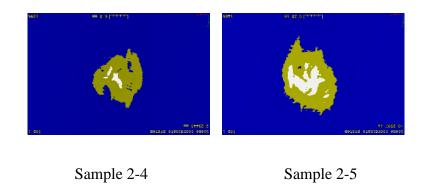


Figure 3. 53: CT image at the plane located 1.87 mm away from the impacted surface

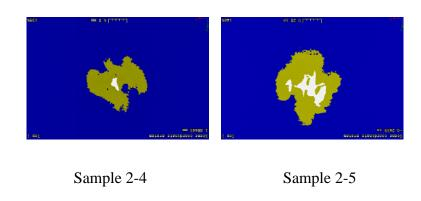


Figure 3. 54: CT image at the plane located 2.22 mm away from the impacted surface

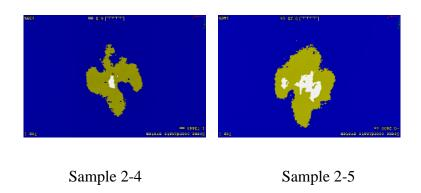


Figure 3. 55: CT image at the plane located 2.37 mm away from the impacted surface

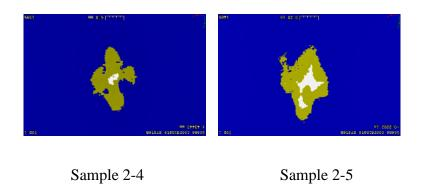


Figure 3. 56: CT image at the plane located 2.67 mm away from the impacted surface

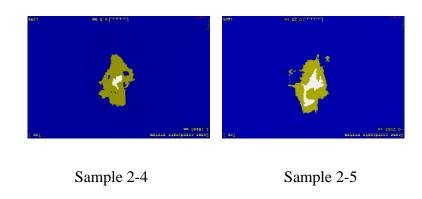


Figure 3. 57: CT image at the plane located 2.92 mm away from the impacted surface

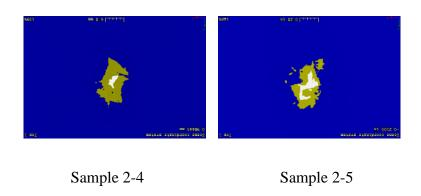


Figure 3. 58: CT image at the plane located 3.12 mm away from the impacted surface

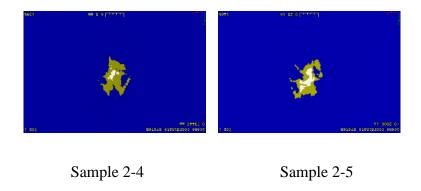


Figure 3. 59: CT image at the plane located 3.37 mm away from the impacted surface

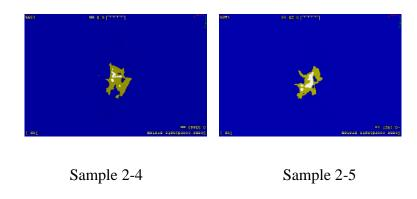


Figure 3. 60: CT image at the plane located 3.57 mm away from the impacted surface

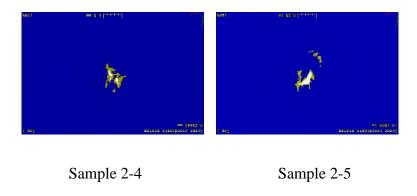


Figure 3. 61: CT image at the plane located 3.87 mm away from the impacted surface

In sample 2-4, the damage zone reached a maximum size at the depth of 2.43 mm away from the impacted surface. Note that the thickness of sample 2-4 was 4.50 mm. The size of the largest damage area was measured by the software MyVGL and was 31.91 mm (see Fig. 3.62; the arrow at the left indicates the 0° orientation).

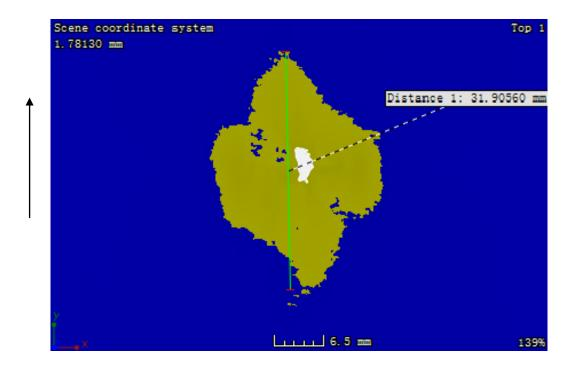


Figure 3. 62: CT image at the plane with the largest damage size in sample 2-4 (located 2.43 mm away from the impacted surface)

In sample 2-5, the damage zone reached a maximum size at the depth of 2.47 mm away from the impacted surface. Note that the thickness of sample 2-5 was 4.59 mm. The



size of the largest damage area was measured by the software MyVGL and was 28.85 mm (see Fig. 3.63; the arrow at the left indicates the 0° orientation).

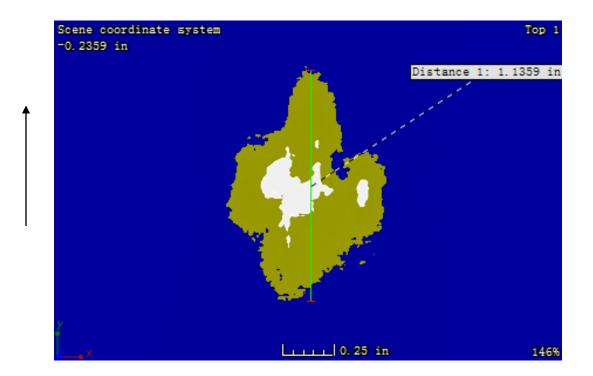


Figure 3. 63: CT image at the plane with the largest damage size in sample 2-5 (located 2.47 mm away from the impacted surface)

Therefore, the maximum measured damage in sample 2-4 is smaller than in the sample 2-5. This observation corresponds well with the maximum impact load and deflection at the maximum impact load (see Table 2.3). The maximum impact load and deflection at the maximum impact load in the sample 2-4 were higher than in the samples



2-5. It is also worth noting that the impact energy in sample 2-4 was very similar to that of sample 2-5. Further comparisons of the impact damage size at the different depths in samples 2-4 and 2-5 are shown in Table 3.2. The measurements in the vertical direction (see Figs. 3.46-3.61) are shown.



Table 3. 2: Damage size at different depths away from the impact surface with highest impact energy

Depth (mm)	Sample 2-4 Damage size (mm)	Sample 2-5 Damage size (mm)
0.22	16.15	16.26
0.47	14.88	13.24
0.62	15.26	14.35
0.77	18.40	17.80
1.07	18.88	19.04
1.37	20.70	22.38
1.62	21.16	22.90
1.87	22.67	26.97
2.22	22.98	27.34
2.37	27.21	28.94
2.67	24.25	25.99
2.92	19.48	20.82
3.12	18.83	17.86
3.37	15.09	13.72
3.57	13.54	11.84
3.87	10.83	

A detailed discussion of the CT scanning process and image analysis of samples 2-4 and 2-5 is given in Appendix C.

To obtain the damage volume of each sample, the CT images of each slice in samples were picked up to measure the damage area, which was yellow part as shown in



last figures. After that, the damage areas were summed up and multiplied by the thickness of each slice to calculate the damage volumes. Table 3.3 shows damage volumes, impact energy, max impact force and total absorbed energy. Figure 3.64 shows damage volume versus impact energy for all eight specimens tested. Figure 3.65 shows damage volume versus max impact force for all eight specimens tested. Figure 3.66 shows damage volume versus total absorbed energy for all eight specimens tested.

Table 3. 3: Damage Volume, Impact Energy, Max Impact Force and Total Absorbed Energy of each sample

Sample	Damage Volume	Impact Energy	Max Impact Force	Total Absorbed Energy
	$(mm^3)$	(J)	(N)	(J)
1-4	90.5636	22.6061	7352.8017	16.2252
1-5	88.2241	22.5044	8474.8902	16.6991
1-6	84.5200	22.4770	8319.5370	17.1960
2-4	101.0850	26.5491	9188.2920	20.6971
2-5	97.3522	26.2521	8686.9310	20.2148
2-1	4.3838	15.9917	8032.5135	16.5684
2-2	4.1607	15.8658	7062.6789	15.9191
2-3	21.2197	16.2049	7810.7599	16.6733

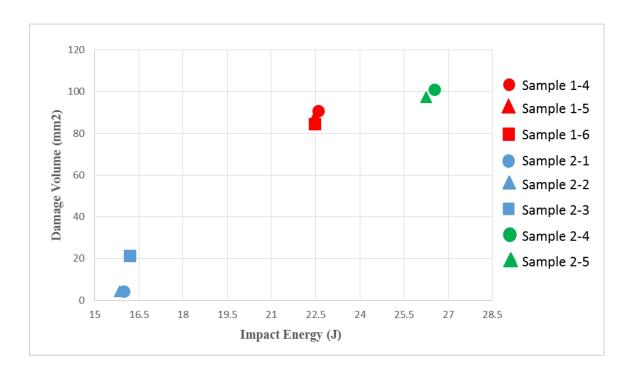


Figure 3. 64: Damage Volume vs. Impact Energy

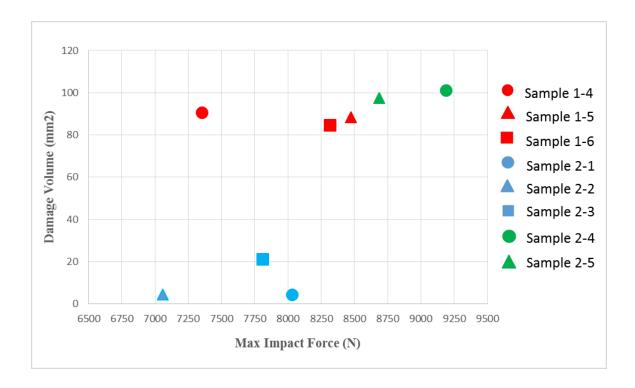


Figure 3. 65: Damage Volume vs. Max Impact Force



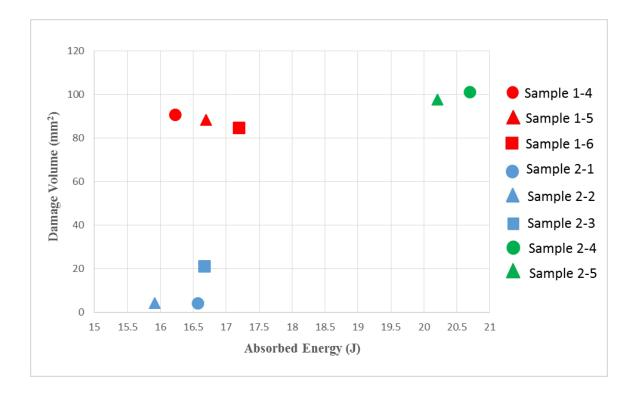


Figure 3. 66: Damage Volume vs. Absorbed Energy

As one can see, there is a strong nonlinear correlation between the impact energy and damage volume that needs further investigation. There is also some correlation between the absorbed energy and the damage volume. Figure 3.66 shows existence of some threshold, above which the delamination is limited and failure mode is mostly related to the fiber breakage within the impact zone. Below the threshold the damage zone increase is mostly driven by delamination. This is also confirmed by the analysis of the Micro CT results.



## 3.4.4 Siemens MicroCAT II CT Results

The ZEISS METROTOM 1500 CT scans were obtained by analyzing impacted 6 in. by 6 in. composite samples. The relatively large sample size did not allow for the detailed evaluation of the damage and enabled only assessment of the damage zone size. After this initial damage size assessment was done, samples 2-1, 1-6, and 2-4 impacted at the lowest, intermediate, and highest energy, respectively, were selected for further evaluation. The smaller square samples, 35 mm by 35 mm, with enclosed impact damage zone, were cut out and analyzed using a Siemens MicroCAT CT system. This section discusses the micro-CT results.

Figures 3.67-3.82 show damage zones in samples 2-1, 1-6, and 2-4 impacted at 16 J, 22.5 J, and 26.5 J. As one can see, the micro-CT allowed more detailed damage visualization with a clear view of delamination and cracks in the damage zone. As expected, the damage zone increased with an increase in the impact energy. The direction of delamination (i.e., the dark grey area around the impact zones) is different at the different depths. This is due to different orientations of the plies in the laminate. Recall that in the studied textile samples, plies with warp directions 45°, -45°, 90°, and 0° were present. In textile composites, delamination tends to propagate more in the warp than in the weft direction. This leads to an oblong shape of the impact damage zones with its major axis in the warp direction seen in CT images. It is interesting to note that the "peanut" shape of the delaminated zone often observed in the laminates reinforced with continuous fibers was not seen in the CT images of the impacted textile composites.

It should also be noted the black circular area in the center of the images of samples 1-6 and 2-4 shown in Figures 3.67-3.70 indicates an air-filled cavity. This is due to the dent caused by the impactor tup that deformed initially flat material surfaces into concave material surfaces (see, e.g., images of the impacted surfaces of the tested specimens in Chapter 2). Dents were present only in the samples impacted at the



intermediate (samples 1-4, 1-5, and 1-6) and highest (samples 2-4 and 2-5) energies. It was found that the dent depth in sample 1-6 was around 0.62 mm and the dent depth in the sample 2-4 was about 0.77 mm. It is also worth mentioning that some insignificant distortion in the micro-CT images was present due to small declination of the sample during the scanning process.

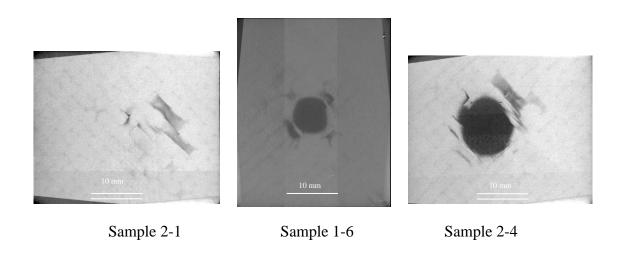


Figure 3. 67: Micro-CT image at the plane located 0.22 mm away from the impacted surface

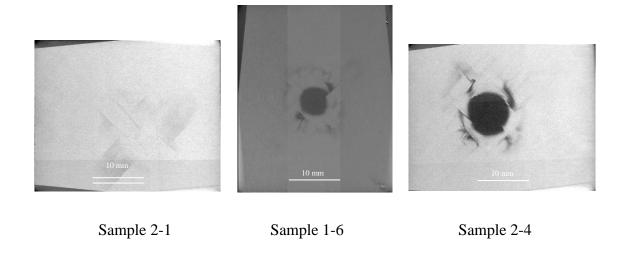


Figure 3. 68: Micro-CT image at the plane located 0.47 mm away from the impacted surface

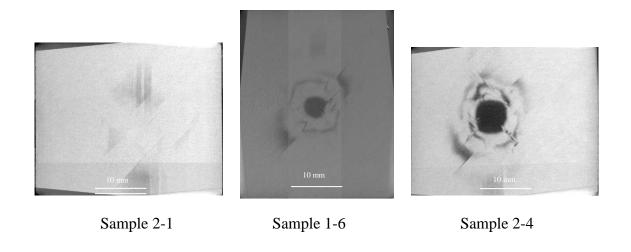
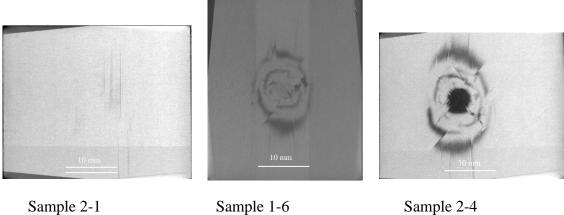


Figure 3. 69: Micro-CT image at the plane located 0.62 mm away from the impacted surface



Sumple 2 1 Sumple 1 6 Sumple 2

Figure 3. 70: Micro-CT image at the plane located 0.77 mm away from the impacted surface

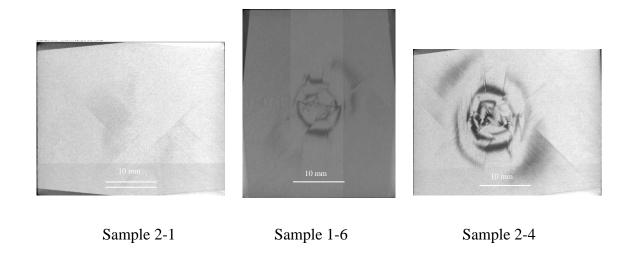


Figure 3. 71: Micro-CT image at the plane located 1.07 mm away from the impacted surface

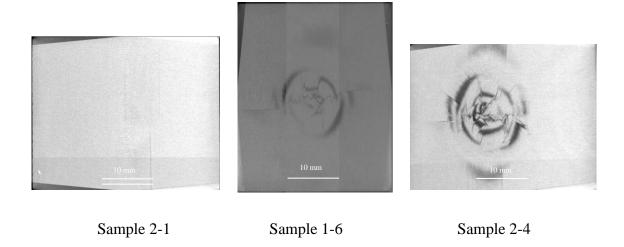


Figure 3. 72: Micro-CT image at the plane located 1.37 mm away from the impacted surface

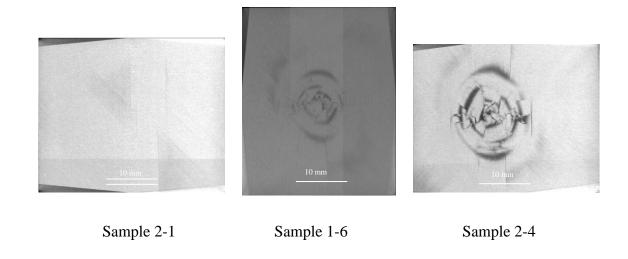


Figure 3. 73: Micro-CT image at the plane located 1.62 mm away from the impacted surface

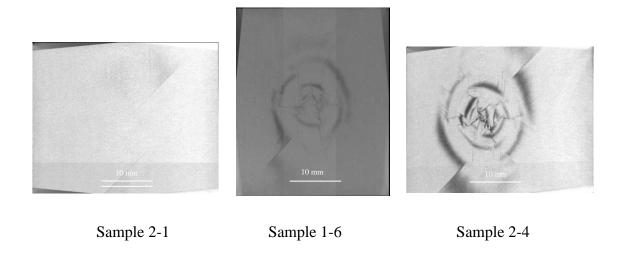


Figure 3. 74: Micro-CT image at the plane located 1.87 mm away from the impacted surface

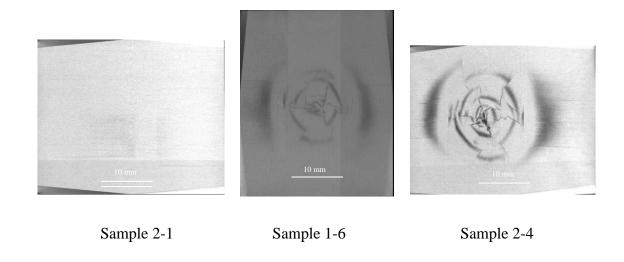


Figure 3. 75: Micro-CT image at the plane located 2.22 mm away from the impacted surface

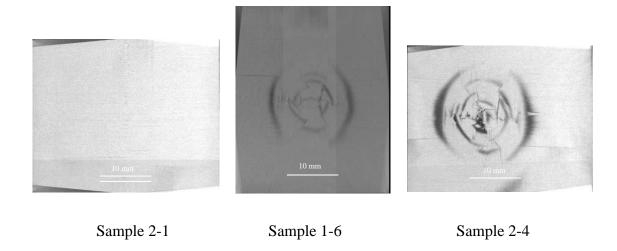


Figure 3. 76: Micro-CT image at the plane located 2.37 mm away from the impacted surface

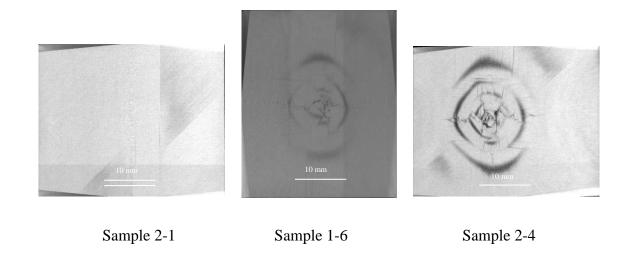


Figure 3. 77: Micro-CT image at the plane located 2.67 mm away from the impacted surface

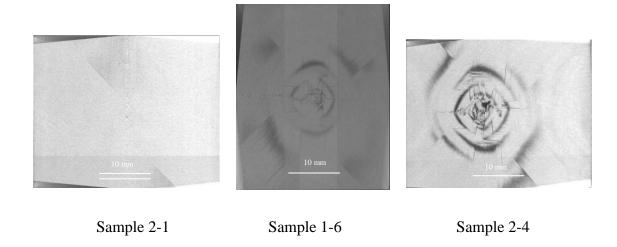


Figure 3. 78: Micro-CT image at the plane located 2.92 mm away from the impacted surface

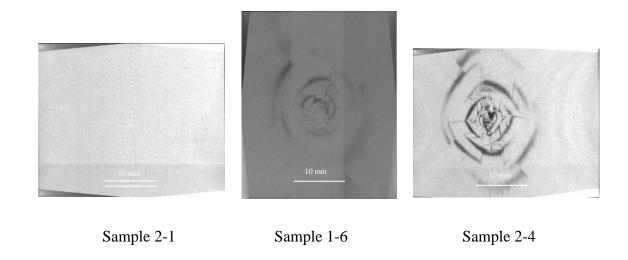


Figure 3. 79: Micro-CT image at the plane located 3.12 mm away from the impacted surface

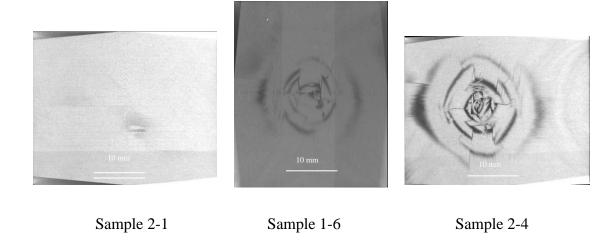


Figure 3. 80: Micro-CT image at the plane located 3.37 mm away from the impacted surface

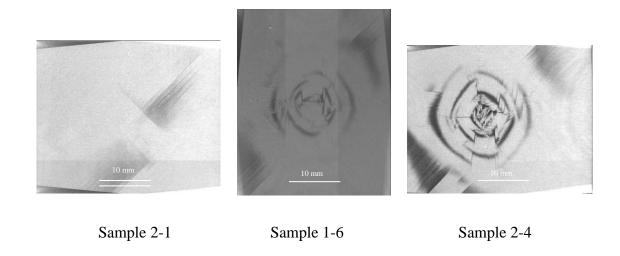


Figure 3. 81: Micro-CT image at the plane located 3.57 mm away from the impacted surface

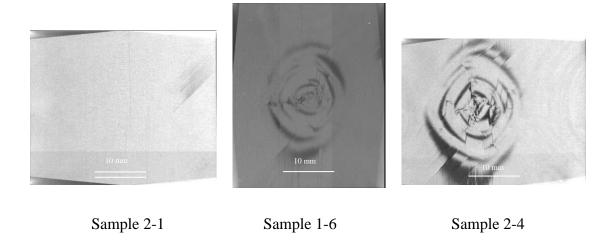


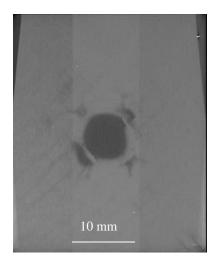
Figure 3. 82: Micro-CT image at the plane located 3.87 mm away from the impacted surface

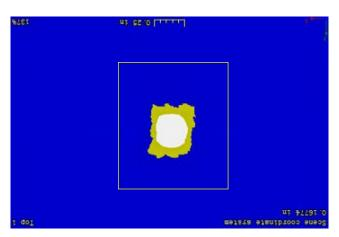
Figures 3.83-3.98 and Figures 3.99-3.114 compare the CT results at different depths obtained using Siemens MicroCAT II (left images) and ZEISS METROTOM 1500 (right images) scanners for samples 1-6 and 2-4, respectively. The comparisons for sample 2-1 were not carried out as the damage zone detected by the ZEISS METROTOM 1500 was too small for any meaningful analysis. Note that micro-CT scans (left images) show the area inside the white box shown in the CT scans obtained using the ZEISS METROTOM 1500 (right images).

The large black area shown in the micro-CT images is air filled cavity. It is also worth mentioning that some insignificant distortion in the micro-CT images is present due to a small declination of the sample during scanning process. The white areas in the images produced by the ZEISS METROTOM 1500 (see, i.e., Figures 3.83-3.86) are concave and correspond to the black areas shown in the micro-CT images. The shape of these white areas is also similar to that of the black areas. As one can see, the shapes of



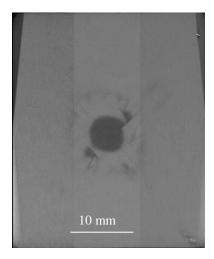
the damage areas in the images produced by the MicroCAT II and METROTOM 1500 are similar. However, images produced by the METROTOM 1500 lack the details with respect to crack direction and delamination. At the same time, these details are very visible in Micro-CT images.

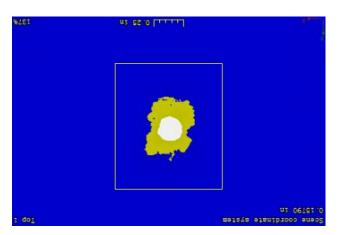




Sample 1-6

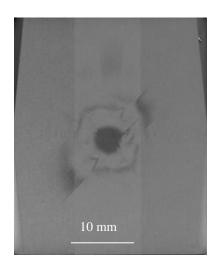
Figure 3. 83: CT image comparison at the plane located 0.22 mm away from the impacted surface

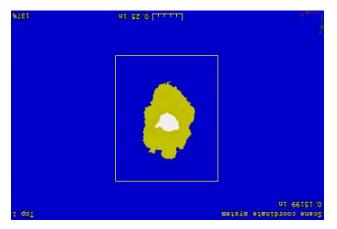




Sample 1-6

Figure 3. 84: CT image comparison at the plane located 0.47 mm away from the impacted surface

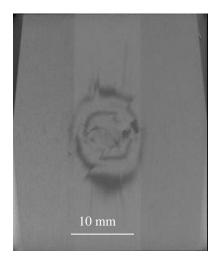


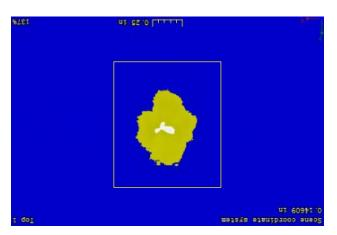


Sample 1-6

Figure 3. 85: CT image comparison at the plane located 0.62 mm away from the impacted surface

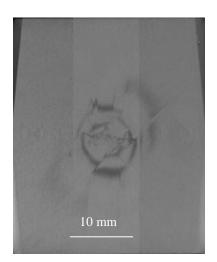


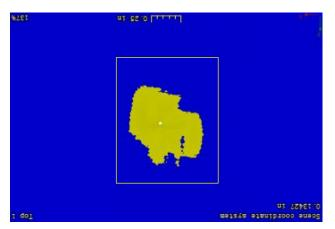




Sample 1-6

Figure 3. 86: CT image comparison at the plane located 0.77 mm away from the impacted surface

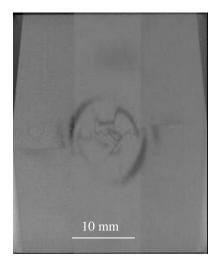


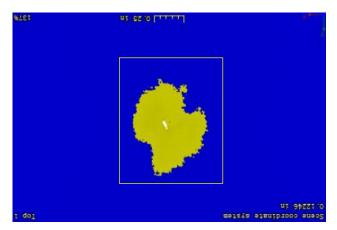


Sample 1-6

Figure 3. 87: CT image comparison at the plane located 1.07 mm away from the impacted surface

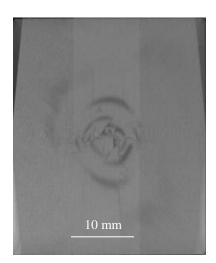


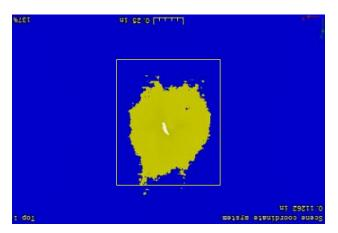




Sample 1-6

Figure 3. 88: CT image comparison at the plane located 1.37 mm away from the impacted surface

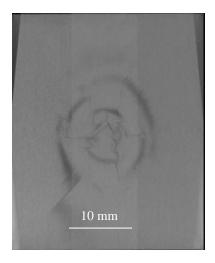


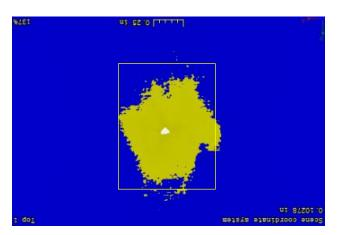


Sample 1-6

Figure 3. 89: CT image comparison at the plane located 1.62 mm away from the impacted surface

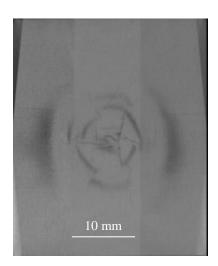


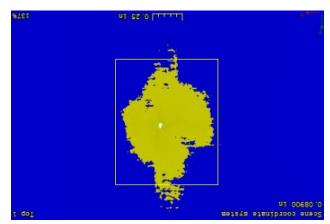




Sample 1-6

Figure 3. 90: CT image comparison at the plane located 1.87 mm away from the impacted surface

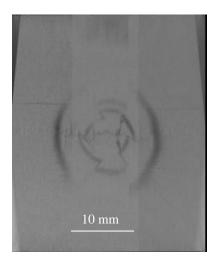


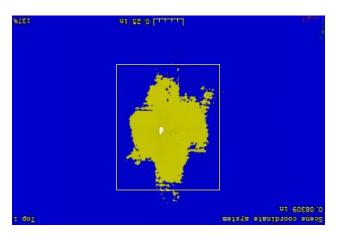


Sample 1-6

Figure 3. 91: CT image comparison at the plane located 2.22 mm away from the impacted surface

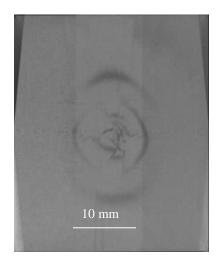


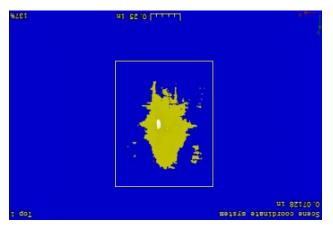




Sample 1-6

Figure 3. 92: CT image comparison at the plane located 2.37 mm away from the impacted surface

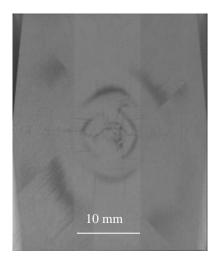


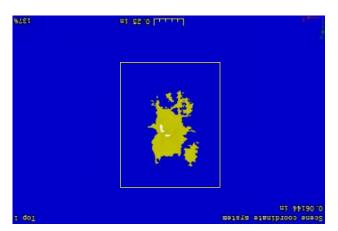


Sample 1-6

Figure 3. 93: CT image comparison at the plane located 2.67 mm away from the impacted surface

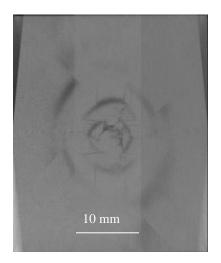


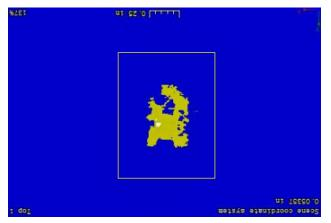




Sample 1-6

Figure 3. 94: CT image comparison at the plane located 2.92 mm away from the impacted surface

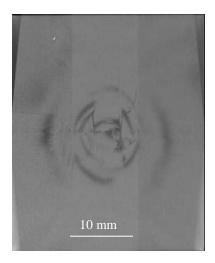


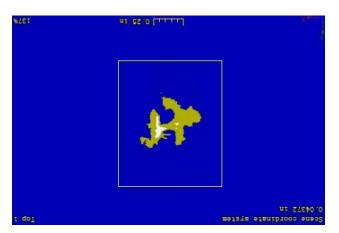


Sample 1-6

Figure 3. 95: CT image comparison at the plane located 3.12 mm away from the impacted surface

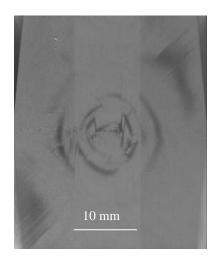


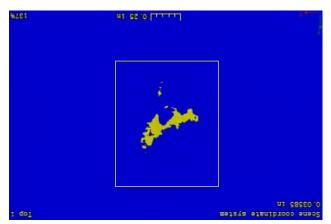




Sample 1-6

Figure 3. 96: CT image comparison at the plane located 3.37 mm away from the impacted surface

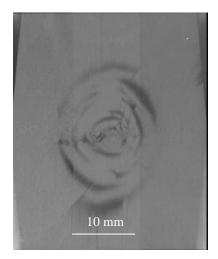




Sample 1-6

Figure 3. 97: CT image comparison at the plane located 3.57 mm away from the impacted surface

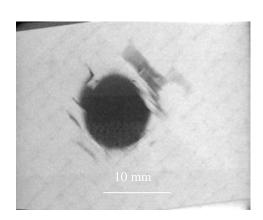


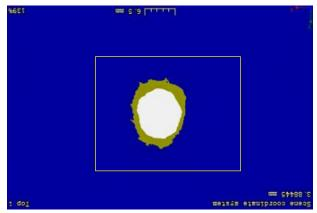




Sample 1-6

Figure 3. 98: CT image comparison at the plane located 3.87 mm away from the impacted surface

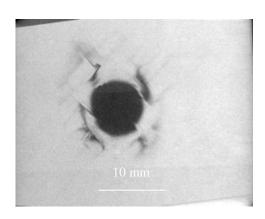


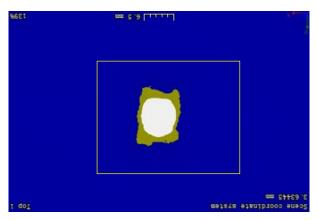


Sample 2-4

Figure 3. 99: CT image comparison at the plane located 0.22 mm away from the impacted surface

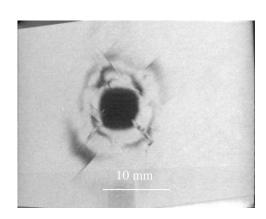


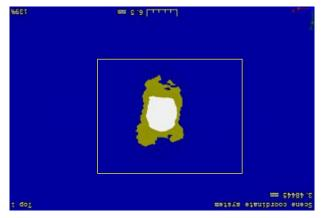




Sample 2-4

Figure 3. 100: CT image comparison at the plane located 0.47 mm away from the impacted surface

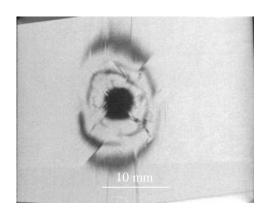


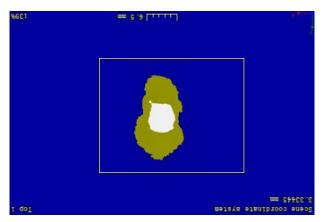


Sample 2-4

Figure 3. 101: CT image comparison at the plane located 0.62 mm away from the impacted surface

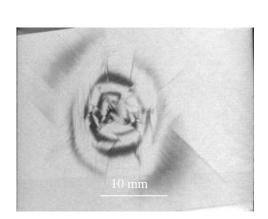


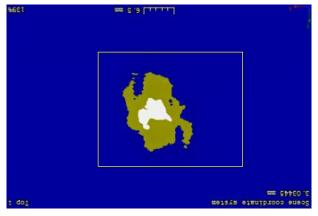




Sample 2-4

Figure 3. 102: CT image comparison at the plane located 0.77 mm away from the impacted surface

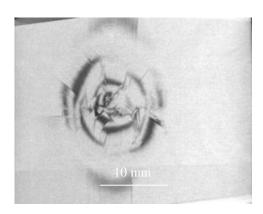


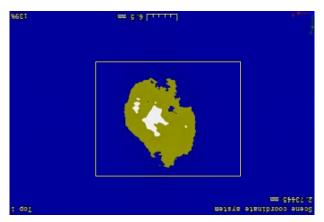


Sample 2-4

Figure 3. 103: CT image comparison at the plane located 1.07 mm away from the impacted surface

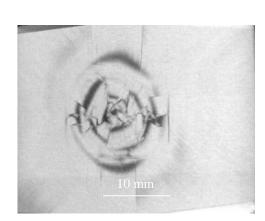






Sample 2-4

Figure 3. 104: CT image comparison at the plane located 1.37 mm away from the impacted surface

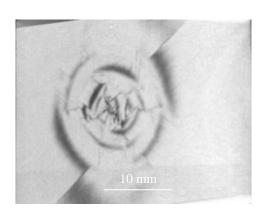


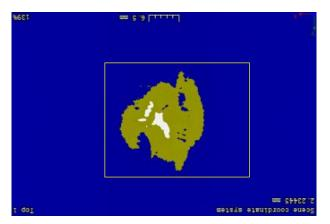


Sample 2-4

Figure 3. 105: CT image comparison at the plane located 1.62 mm away from the impacted surface

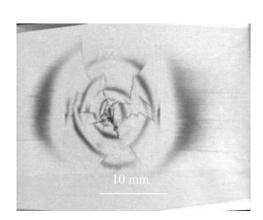


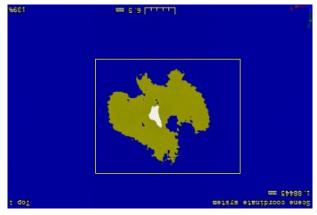




Sample 2-4

Figure 3. 106: CT image comparison at the plane located 1.87 mm away from the impacted surface

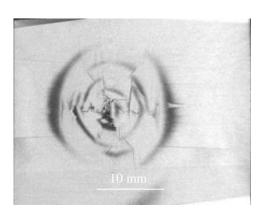


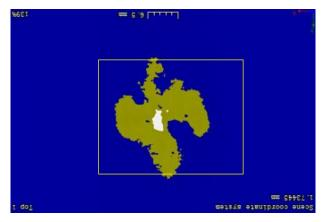


Sample 2-4

Figure 3. 107: CT image comparison at the plane located 2.22 mm away from the impacted surface

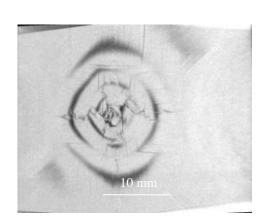


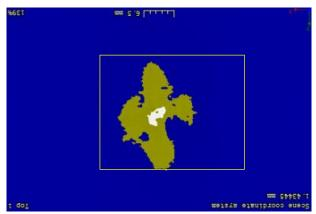




Sample 2-4

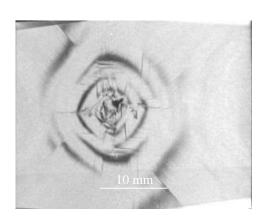
Figure 3. 108: CT image comparison at the plane located 2.37 mm away from the impacted surface

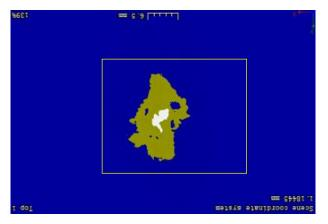




Sample 2-4

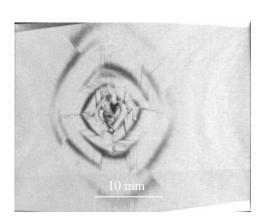
Figure 3. 109: CT image comparison at the plane located 2.67 mm away from the impacted surface

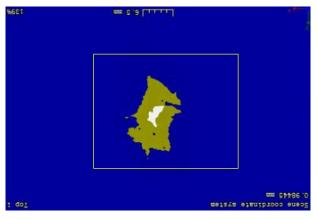




Sample 2-4

Figure 3. 110: CT image comparison at the plane located 2.92 mm away from the impacted surface

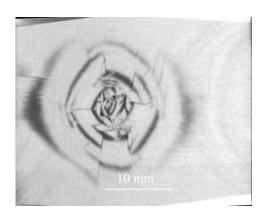




Sample 2-4

Figure 3. 111: CT image comparison at the plane located 3.12 mm away from the impacted surface

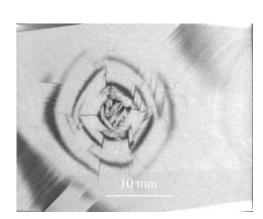


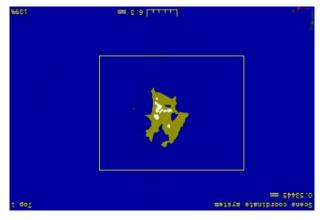




Sample 2-4

Figure 3. 112: CT image comparison at the plane located 3.37 mm away from the impacted surface

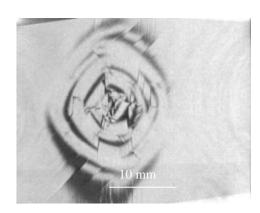




Sample 2-4

Figure 3. 113: CT image comparison at the plane located 3.57 mm away from the impacted surface







Sample 2-4

Figure 3. 114: CT image comparison at the plane located 3.87 mm away from the impacted surface



#### **CHAPTER 4**

### SUMMARY AND RECOMMENDATIONS

## 4.1 Summary

In this work, the low-velocity impact resistance of layered carbon fiber polymer matrix five harness satin textile composites has been studied. A series of impact characterization tests at different impact energy levels was performed using an Instron 8200 Dynatup impact tester. Real-time measurements of impact load, deflection, and energy were recorded and analyzed, and impact damage was assessed.

Impact damage in the textile composites with respect to different impact energy levels has also been studied using computed tomography (CT). Two different CT systems, ZEISS METROTOM 1500 and Siemens MicroCAT II, were used for the quantitative damage assessment. The capabilities of both systems to evaluate low-velocity impact damage in layered carbon fiber polymer matrix composites were investigated.

ZEISS METROTOM 1500 CT scans were obtained by analyzing impacted 6 in. by 6 in. composite samples. The relatively large sample size did not allow for detailed evaluation of the damage (cracks and delamination were not visible) and enabled only assessment of the damage zone size. After this initial damage size assessment was done, smaller square samples, 35 mm by 35 mm, with enclosed impact damage zones, were cut out and analyzed using a Siemens MicroCAT CT system. The micro-CT scans produced detailed visualization of cracks and delamination in the damage zones of the impacted textile composite specimens. However, the MicroCAT CT system is limited to the analysis of small articles and is unable to scan composite specimens of the standard size (squares of 6 in. by 6 in.) used in the low-velocity impact characterization tests.



### 4.2 Recommendations

The first recommendation is to improve the CT scanning procedure. The position of the specimens during CT scanning should be the same, as should the scanning parameters. In this work, specimens scanned using the ZEISS METROTOM 1500 were positioned differently, which required rotation of images for comparisons of damage. Moreover, the scanning direction was different. In some specimens, the top scanning surface was the impacted (front) surface, while for others the top scanning surface corresponded to the back (non-impacted) specimen surface. Furthermore, scanning parameters were set differently (e.g., mm vs. in.), which created some inconvenience when comparing damage at the same depth.

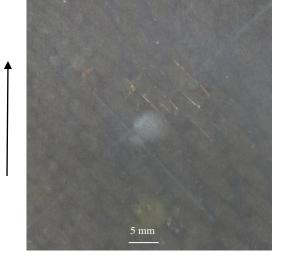
The second recommendation is to investigate the capabilities of the ZEISS METROTOM 1500 for scanning samples of smaller size. This study found that, although the MicroCAT II was an excellent tool for the detailed evaluation of cracks and delamination, the Micro-CT slices were not thin enough (i.e., the resolution of the micro-CT was not high enough) to allow visualization of all interfaces between lamina in the laminate. Delamination (i.e., debonding between adjacent plies) is a serious concern since it significantly reduces the strength of the laminate. Thus, detailed evaluation of all interlaminar surfaces is desirable for accurate damage assessment.

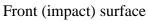


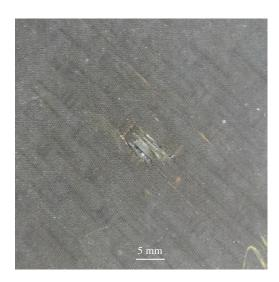
#### APPENDIX A

# ZEISS METROTOM 1500 CT RESULTS FOR THE SPECIMENS IMPACTED AT THE LOWEST IMPACT ENERGY

For samples 2-1, 2-2, and 2-3, the impact energy level was 16 J. Figure A.1 shows pictures of Sample 1-4 after the impact test. The arrow on the left indicates the 0° direction. Figures A.2- A.6 show damage zones at different depths from the impacted surface of sample 2-1. As one can see, the extent of the damage zone increases with depth. The arrow on the left of Figure A.2 indicates the 0° orientation.







Back surface

Figure A. 1: Sample 2-1





Figure A. 2: CT image at the plane located 0. 22 mm away from the impacted surface of sample 2-1

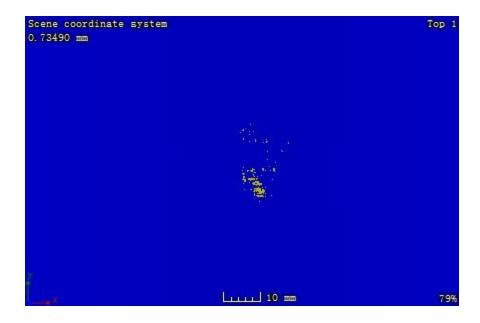


Figure A. 3: CT image at the plane located 1.87 mm away from the impacted surface of sample 2-1



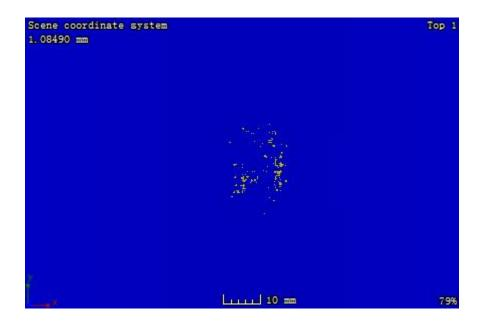


Figure A. 4: CT image at the plane located 2.22 mm away from the impacted surface of sample 2-1

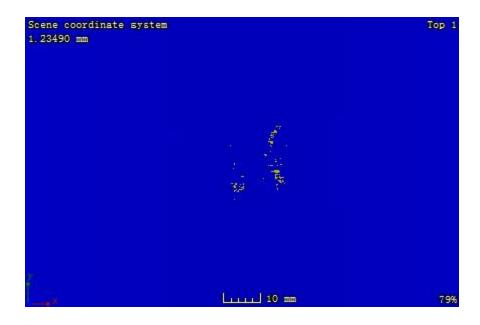


Figure A. 5: CT image at the plane located 2.37 mm away from the impacted surface of sample 2-1



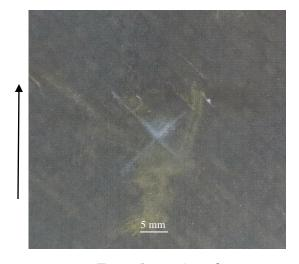


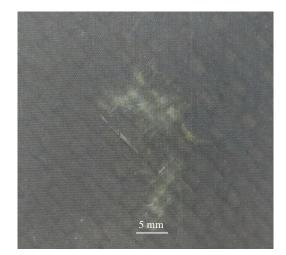
Figure A. 6: CT image at the plane located 3.87 mm away from the impacted surface of sample 2-1

As one can see, damage was detected inside sample 2-1 at about 2.22 mm depth from the impacted surface. This was also confirmed by Siemens MicroCAT II CT results.

Figures A.7- A.13 show damage zones at different depths from the impacted surface of sample 2-2. As one can see, the extent of the damage zone increases with depth. The arrow on the left of Figures A.7and A.8 indicates the 0° orientation.







Front (impact) surface

Back surface

Figure A. 7: Sample 2-2



Figure A. 8: CT image at the plane located 0. 22 mm away from the impacted surface of sample 2-2





Figure A. 9: CT image at the plane located 0.47 mm away from the impacted surface of sample 2-2

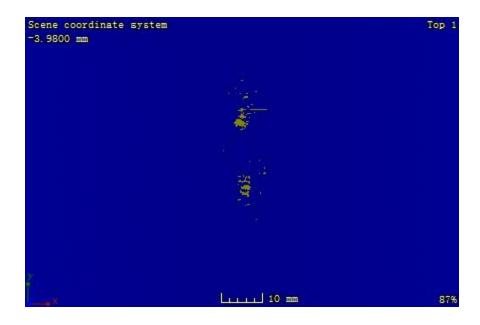


Figure A. 10: CT image at the plane located 2.22 mm away from the impacted surface of sample 2-2





Figure A. 11: CT image at the plane located 2.37 mm away from the impacted surface of sample 2-2



Figure A. 12: CT image at the plane located 2.67 mm away from the impacted surface of sample 2-2



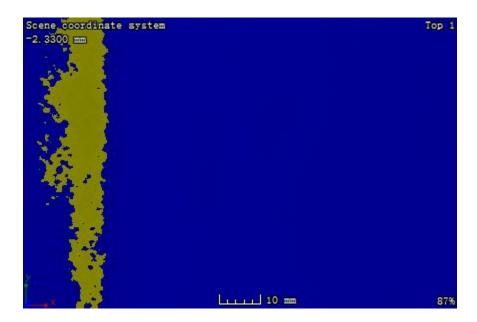
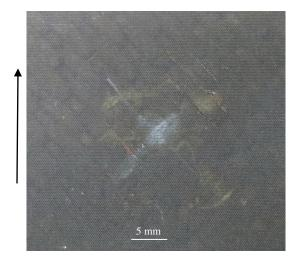


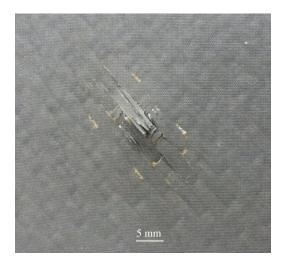
Figure A. 13: CT image at the plane located 3.87 mm away from the impacted surface of sample 2-2

As one can see, damage was detected inside sample 2-2 at about 2.22 mm depth from the impacted surface, the same depth as for sample 2-22. This was also confirmed by Siemens MicroCAT II CT results.

Figures A147- A.24 show damage zones at different depths from the impacted surface of sample 2-3. The arrow on the left of Figures A.14and A.15 indicates the 0° orientation.







Front (impact) surface

Back surface

Figure A. 14: Sample 2-3



Figure A. 15: CT image at the plane located 0. 22 mm away from the impacted surface of sample 2-3



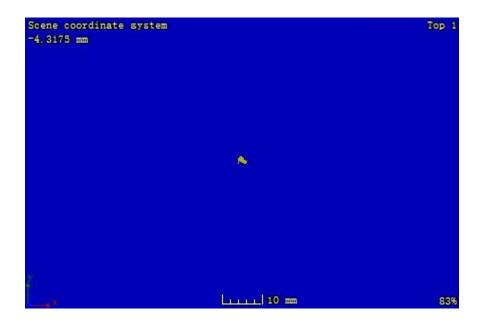


Figure A. 16: CT image at the plane located 0.47 mm away from the impacted surface of sample 2-3

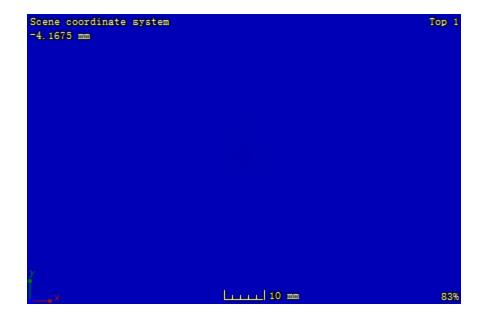


Figure A. 17: CT image at the plane located 0.62 mm away from the impacted surface of sample 2-2





Figure A. 18: CT image at the plane located 1.87 mm away from the impacted surface of sample 2-3



Figure A. 19: CT image at the plane located 2.22 mm away from the impacted surface of sample 2-3





Figure A. 20: CT image at the plane located 2.37 mm away from the impacted surface of sample 2-3



Figure A. 21: CT image at the plane located 2.67 mm away from the impacted surface of sample 2-3



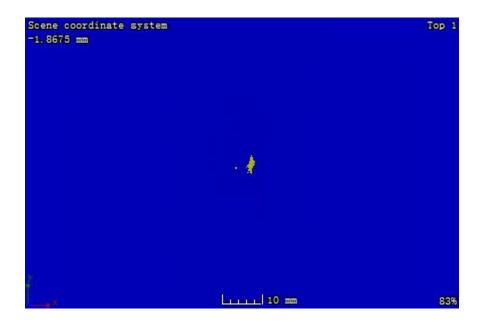


Figure A. 22: CT image at the plane located 2.97 mm away from the impacted surface of sample 2-3



Figure A. 23: CT image at the plane located 3.12 mm away from the impacted surface of sample 2-3



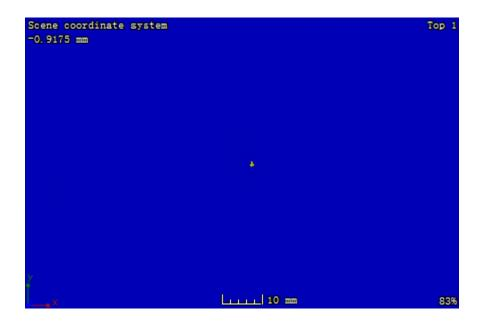


Figure A. 24: CT image at the plane located 3.87 mm away from the impacted surface of sample 2-3

As one can see, damage was detected inside sample 2-2 at about 1.87 mm depth from the impacted surface. This was also confirmed by Siemens MicroCAT II CT results. Sample 2-3 received the largest damage comparing with samples 2-1 ans 2-2. This was confirmed by the analysis of the surfaces of the samples (see Figures A.14, A.7, and A.1). The impact energy for sample 2-3 was 16.2049 J, which is slightly higher than for sample 2-1 (impact energy was 15.9917 J) and sample 2-2 (impact energy was 15.8658 J).

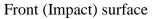


#### APPENDIX B

# ZEISS METROTOM 1500 CT RESULTS FOR THE SPECIMENS IMPACTED AT THE INTERMEDIATE IMPACT ENERGY

For samples 1-4, 1-5, and 1-6, the impact energy level was 22.5 J. Figure B.1 shows pictures of Sample 1-4 after the impact test. The arrow on the left indicates the 0° direction. Figure B.2 and Figure B.3 show images scanned from the right and front scan directions. These images also enable one to determine if the top direction was indeed pointing into the impacted side of a sample. It was determined that for sample 1-4 the scan direction was opposite to the impact direction and the top scanning surface corresponded to the back side of sample 1-4. The scan and impact direction are shown in Figure B.2 and Figure B.3.







Back surface

Figure B. 1: Sample 1-4



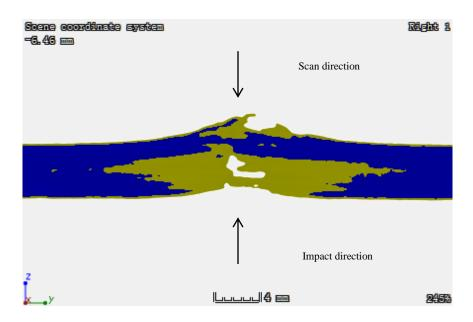


Figure B. 2: CT image in the center of sample 1-4 in the right scan direction

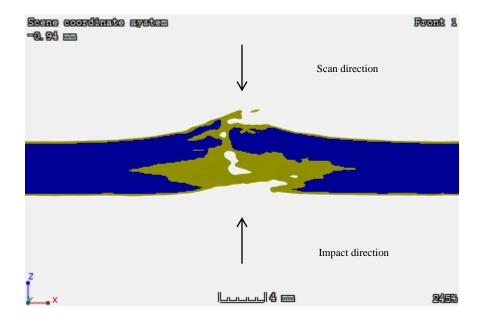


Figure B. 3: CT image in the center of sample 1-4 in the front scan direction



Figures B.4- B.20 show damage zones at different depths from the impacted surface of sample 1-4. As one can see, the extent of the damage zone increases with depth. The arrow on the left of Figure B.4 indicates the 0° orientation.



Figure B. 4: CT image at the plane located 0.22 mm away from the impacted surface of sample 1-4



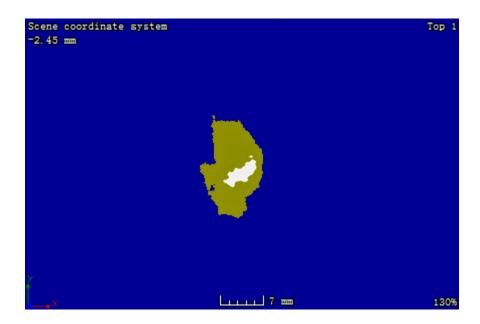


Figure B. 5: CT image at the plane located 0.47 mm away from the impacted surface of sample 1-4

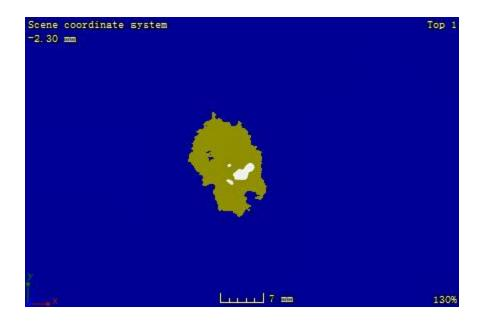


Figure B. 6: CT image at the plane located 0.62 mm away from the impacted surface of sample 1-4





Figure B. 7: CT image at the plane located 0.77 mm away from the impacted surface of sample 1-4

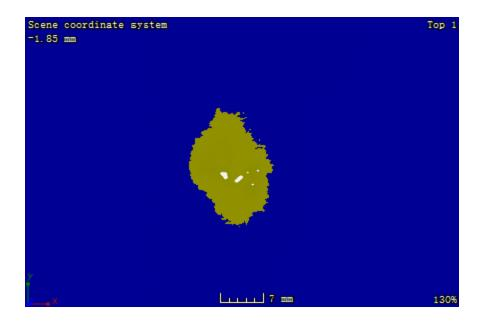


Figure B. 8: CT image at the plane located 1.07 mm away from the impacted surface of sample 1-4



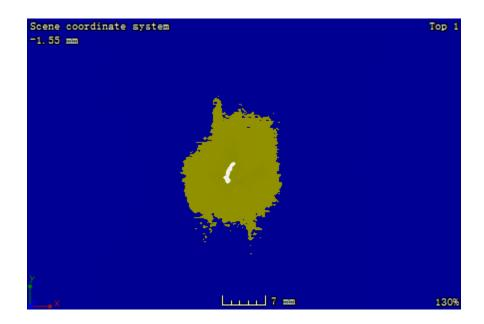


Figure B. 9: CT image at the plane located 1.37 mm away from the impacted surface of sample 1-4

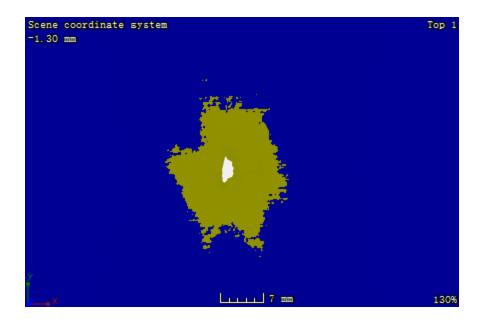


Figure B. 10: CT image at the plane located 1.62 mm away from the impacted surface of sample 1-4



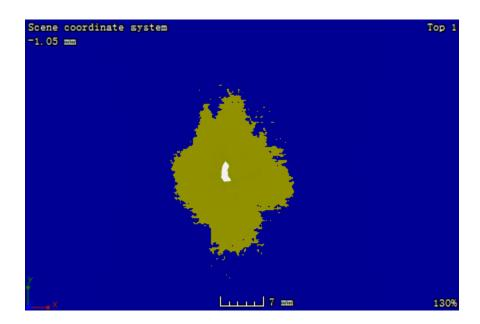


Figure B. 11: CT image at the plane located 1.87 mm away from the impacted surface of sample 1-4

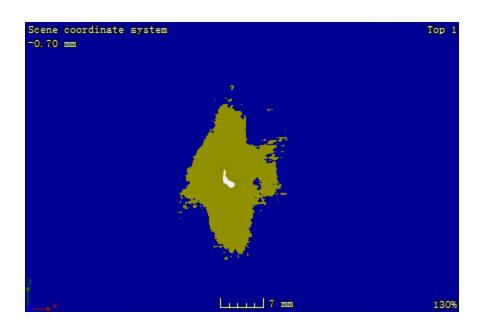


Figure B. 12: CT image at the plane located 2.22 mm away from the impacted surface of sample 1-4



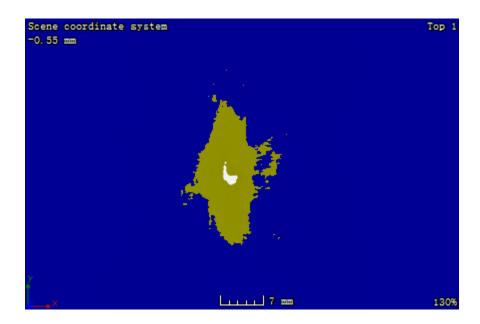


Figure B. 13: CT image at the plane located 2.37 mm away from the impacted surface of sample 1-4

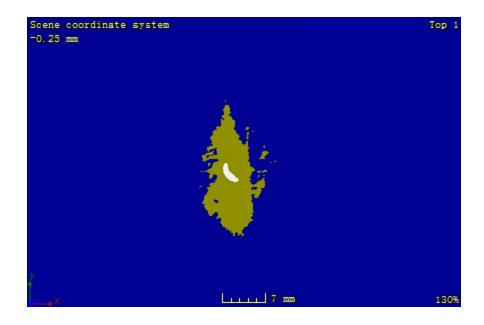


Figure B. 14: CT image at the plane located 2.67 mm away from the impacted surface of sample 1-4





Figure B. 15: CT image at the plane located 2.92 mm away from the impacted surface of sample 1-4

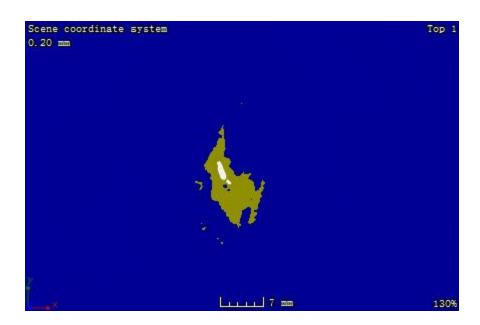


Figure B. 16: CT image at the plane located 3.12 mm away from the impacted surface of sample 1-4



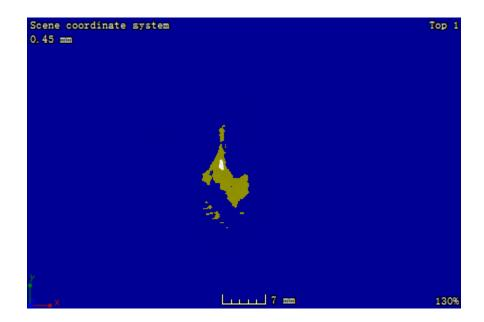


Figure B. 17: CT image at the plane located 3.37 mm away from the impacted surface of sample 1-4



Figure B. 18: CT image at the plane located 3.57 mm away from the impacted surface of sample 1-4





Figure B. 19: CT image at the plane located 3.87 mm away from the impacted surface of sample 1-4

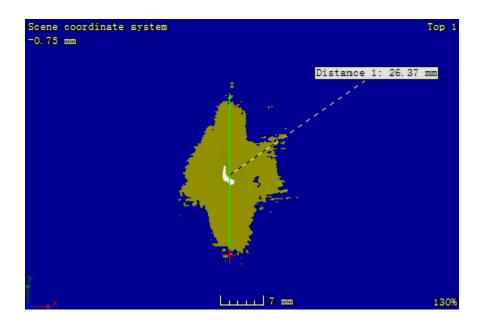


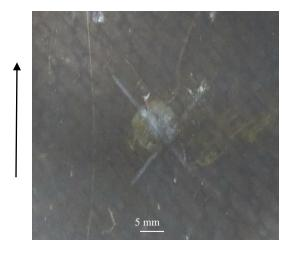
Figure B. 20: CT image at the plane with the largest damage size in sample 1-4 (located 2.17 mm away from the impacted surface)



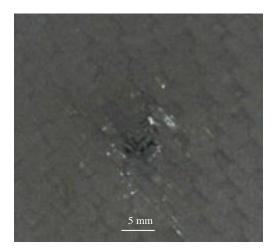
In sample 1-4, the damage zone reached maximum size at the depth of 2.17 mm away from the impacted surface. Note that the thickness of sample 1-4 was 4.57 mm. The size of the largest damage area was measured by the software MyVGL and was 26.37 mm. It is also worth noticing that the orientation of the damage zone changes with depth. This is due to the fact that the tested samples are laminated composites that have multiple lamina of various orientation, i.e., 45°, -45°, 0°, and 90°.

During CT scanning, sample 1-5 was placed in a reversed position compared with sample 1-4 (the top scanning surface corresponded to the impacted surface). In addition, it was turned 90 degrees with respect to the z-axis compared to sample 1-4.

Figure B.21 shows the impacted surface and a close view of the front (impacted side) and back surfaces of sample 1-5. The arrow on the left of Figure B.21 shows 0 degree orientation.







Back surface

Figure B. 21: Sample 1-5



Figure B.22 and B.23 show images scanned from the right and front scan directions. It was determined from these images that for sample 1-5 the scan direction was the same as the direction of the impact. The scan and impact direction are shown in Figures B.22 and B.23.

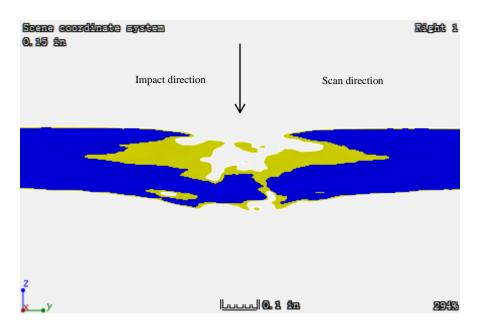


Figure B. 22: CT image in the center of sample 1-5 in the right scan direction



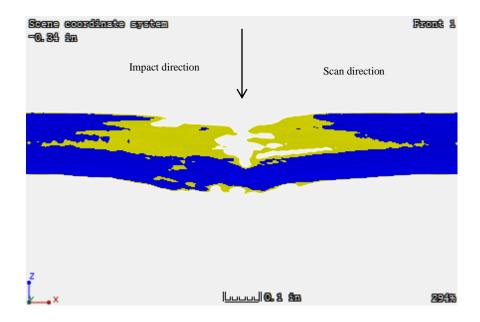


Figure B. 23: CT image in the center of sample 1-5 in the front scan direction

Figures B.24- B.40 show damage zones at different depths from the impacted surface of sample 1-5. The arrow on the top of Figure B.24 indicates the  $0^{\circ}$  orientation.



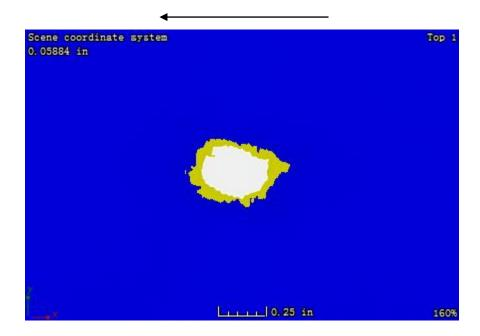


Figure B. 24: CT image at the plane located 0.22 mm away from the impacted surface of sample 1-5

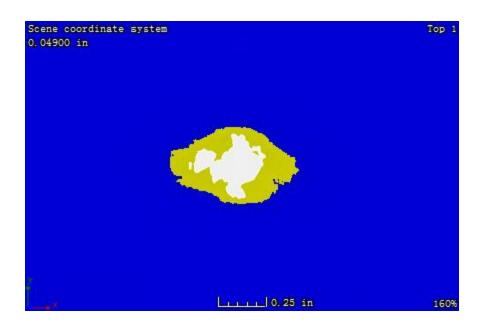


Figure B. 25: CT image at the plane located 0.47 mm away from the impacted surface of sample 1-5



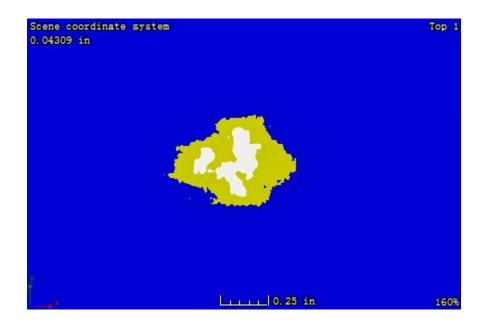


Figure B. 26: CT image at the plane located 0.62 mm away from the impacted surface of sample 1-5



Figure B. 27: CT image at the plane located 0.77 mm away from the impacted surface of sample 1-5



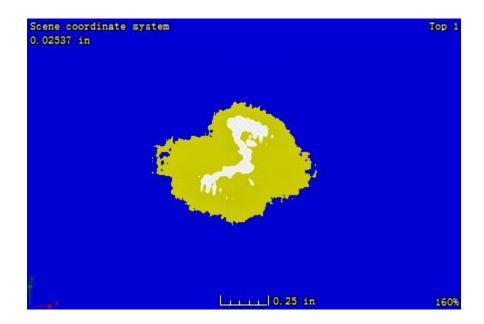


Figure B. 28: CT image at the plane located 1.07 mm away from the impacted surface of sample 1-5

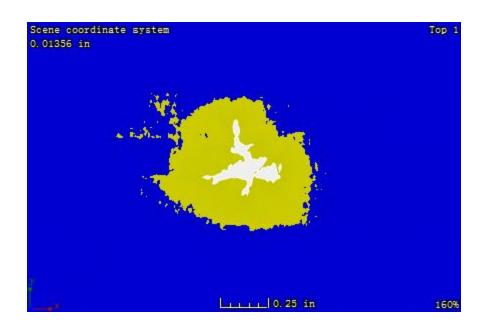


Figure B. 29: CT image at the plane located 1.37 mm away from the impacted surface of sample 1-5



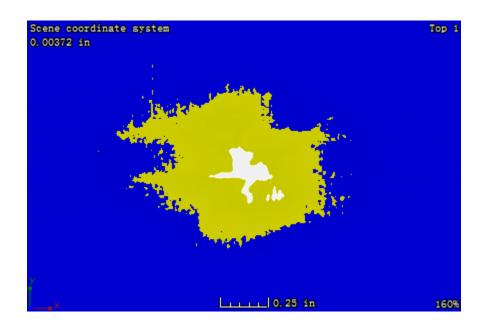


Figure B. 30: CT image at the plane located 1.62 mm away from the impacted surface of sample 1-5

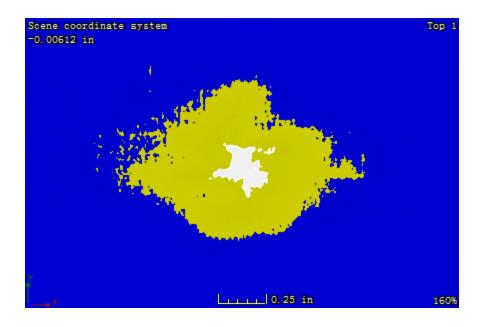


Figure B. 31: CT image at the plane located 1.87 mm away from the impacted surface of sample 1-5



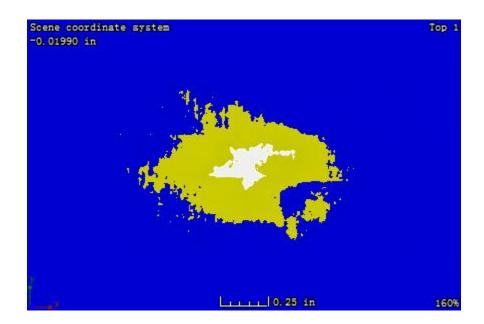


Figure B. 32: CT image at the plane located 2.22 mm away from the impacted surface of sample 1-5

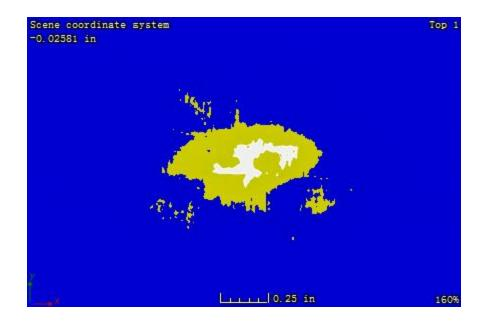


Figure B. 33: CT image at the plane located 2.37 mm away from the impacted surface of sample 1-5





Figure B. 34: CT image at the plane located 2.67 mm away from the impacted surface of sample 1-5



Figure B. 35: CT image at the plane located 2.92 mm away from the impacted surface of sample 1-5





Figure B. 36: CT image at the plane located 3.12 mm away from the impacted surface of sample 1-5



Figure B. 37: CT image at the plane located 3.37 mm away from the impacted surface of sample 1-5





Figure B. 38: CT image at the plane located 3.57 mm away from the impacted surface of sample 1-5



Figure B. 39: CT image at the plane located 3.87 mm away from the impacted surface of sample 1-5



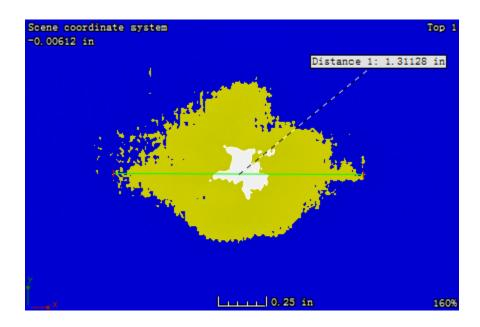
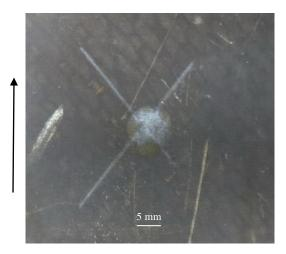


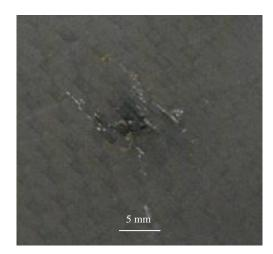
Figure B. 40: CT image at the plane with the largest damage size in sample 1-5 (located 1.87 mm away from the impacted surface)

As one can see, the extent of the damage zone increases with depth, and damage size reaches maximum at the depth of 1.87 mm away from the impacted surface. Note that the thickness of sample 1-5 was 4.61 mm. The size of the largest damage area was measured by the software MyVGL and was 33.31 mm (see Figure B.40). It is also important to notice that the view side of the slices shown in Figures B.24- B.40 is different from the view side of the slices shown in Figures B.4- B.20, although the images are shown at the same depth from the impacted surface. In sample 1-5, the scan direction was the same as the impact direction, and in sample 1-4, the scan direction was opposite to the impact direction. This also explains the difference in the orientation of the damage zones in samples 1-4 and 1-5 in the planes located at the same distance from the surface.



The CT images of sample 1-6 were analyzed in a similar manner. Figure B.41 shows the impacted surface of sample 1-6. It also shows a close view of the front (impacted side) and back surfaces of sample 1-6.





Front (Impact) surface

Back surface

Figure B. 41: Sample 1-6

It was determined from these images that for sample 1-6 the scan direction was the same as the direction of the impact. Figures B.42- B.58 show damage zones at different depths from the impacted surface of sample 1-6. The arrow on the left of Figure B.42 indicates the 0° orientation.

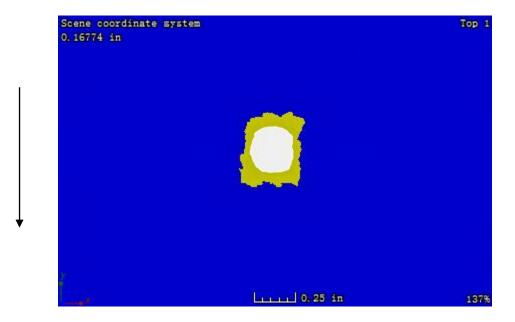


Figure B. 42: CT image at the plane located 0.22 mm away from the impacted surface of sample 1-6

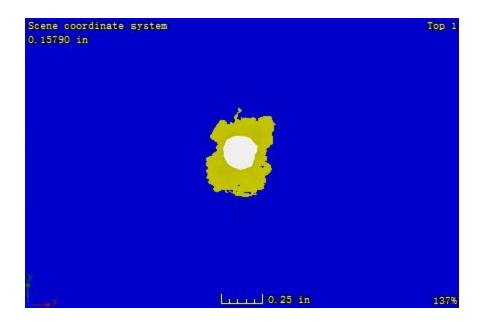


Figure B. 43: CT image at the plane located 0.47 mm away from the impacted surface of sample 1-6



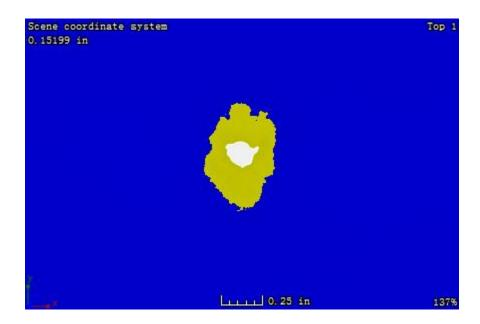


Figure B. 44: CT image at the plane located 0.62 mm away from the impacted surface of sample 1-6

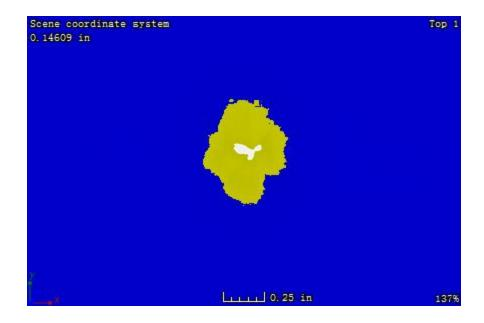


Figure B. 45: CT image at the plane located 0.77 mm away from the impacted surface of sample 1-6



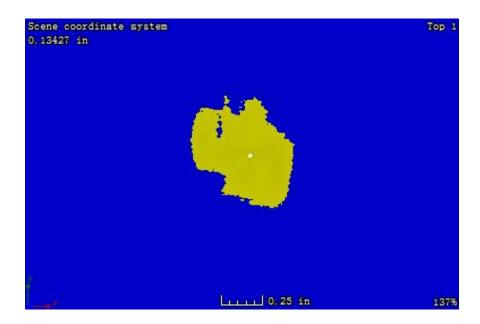


Figure B. 46: CT image at the plane located 1.07 mm away from the impacted surface of sample 1-6

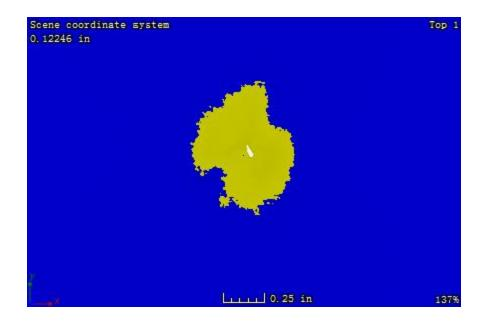


Figure B. 47: CT image at the plane located 1.37 mm away from the impacted surface of sample 1-6



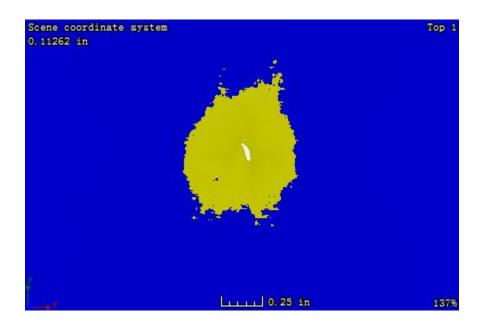


Figure B. 48: CT image at the plane located 1.62 mm away from the impacted surface of sample 1-6

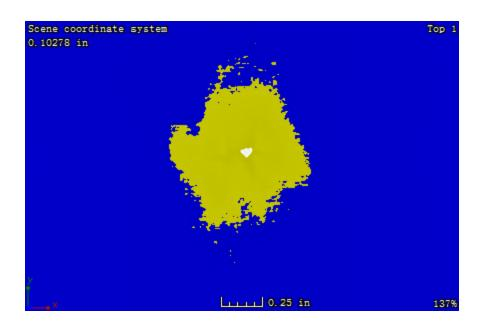


Figure B. 49: CT image at the plane located 1.87 mm away from the impacted surface of sample 1-6



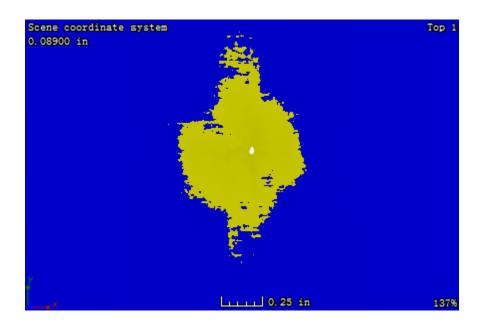


Figure B. 50: CT image at the plane located 2.22 mm away from the impacted surface of sample 1-6

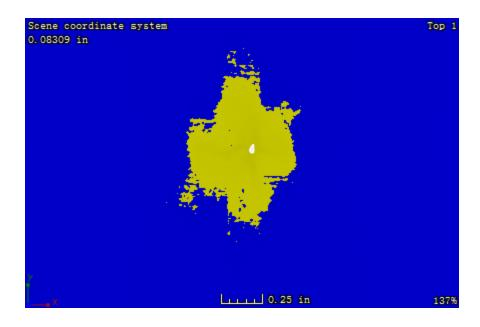


Figure B. 51: CT image at the plane located 2.37 mm away from the impacted surface of sample 1-6



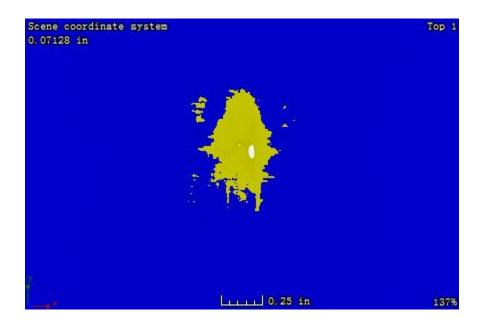


Figure B. 52: CT image at the plane located 2.67 mm away from the impacted surface of sample 1-6

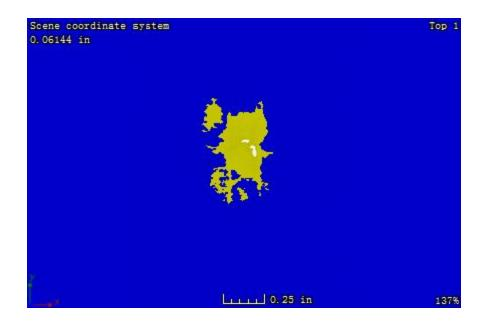


Figure B. 53: CT image at the plane located 2.92 mm away from the impacted surface of sample 1-6



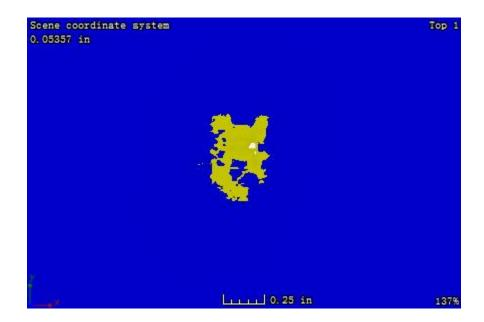


Figure B. 54: CT image at the plane located 3.12 mm away from the impacted surface of sample 1-6

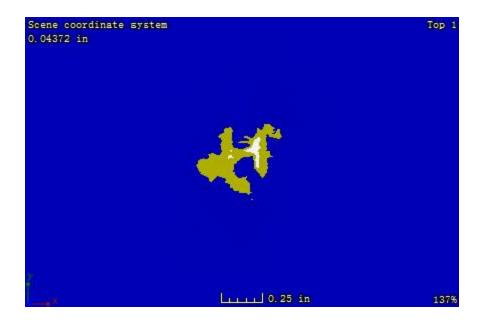


Figure B. 55: CT image at the plane located 3.37 mm away from the impacted surface of sample 1-6



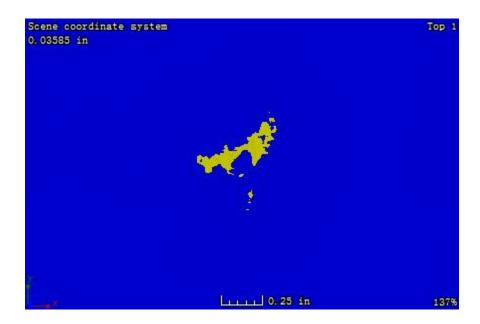


Figure B. 56: CT image at the plane located 3.57 mm away from the impacted surface of sample 1-6

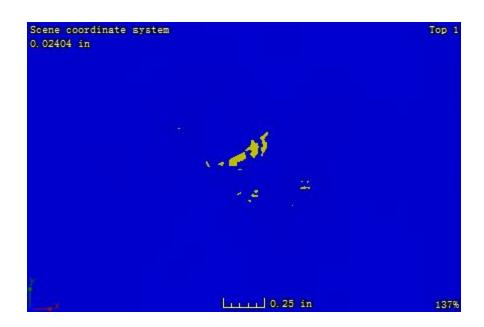


Figure B. 57: CT image at the plane located 3.87 mm away from the impacted surface of sample 1-6



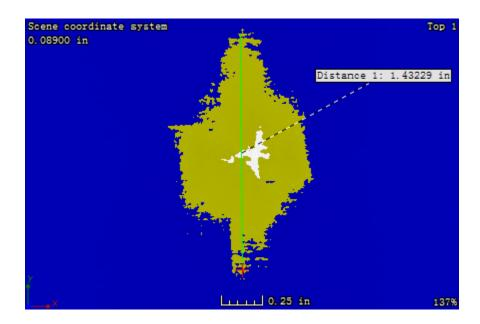


Figure B. 58: CT image at the plane with the largest damage size in sample 1-6 (located 2.22 mm away from the impacted surface)

As one can see, the extent of the damage zone increases with depth, and damage size reaches its maximum at the depth of 2.22 mm away from the impacted surface. Note that the thickness of sample 1-5 was 4.61mm. The size of the largest damage area was measured by the software MyVGL and was 36.38 mm (see Figure B.58). It is also important to notice that the view side of the slices shown in Figure B.42- B.58 is the same as in Figures B.24- B.40, but that it is different from the view side of the slices shown in Figures B.4- B.20, and the images are shown at the same depth from the impacted surface. In samples 1-5 and 1-6, the scan direction was the same as the impact direction, and in sample 1-4, the scan direction was opposite that of the impact direction. This also explains the similarity in the damage orientation in samples 1-5 and 1-6 and the



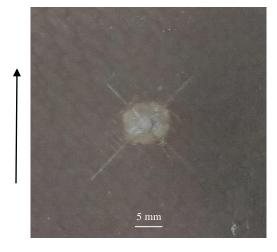
difference with sample 1-4, when comparing slices at the same distance from the impacted surface.

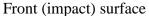


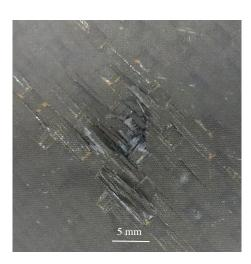
## APPENDIX C

## ZEISS METROTOM 1500 CT RESULTS FOR THE SPECIMENS IMPACTED AT THE HIGHEST IMPACT ENERGY

For samples 2-4, 2-5, the impact energy level was 26 J. Figure C.1 shows pictures of Sample 2-4 after the impact test. The arrow on the left of Figure C.1 and C.2 indicates the 0° orientation. Figures C.2- C.18 show damage zones at different depths from the impacted surface of sample 2-4. As one can see, the extent of the damage zone increases with depth.







Back surface

Figure C. 1: Sample 2-4

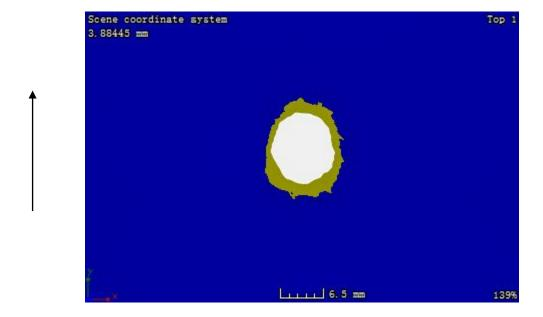


Figure C. 2: CT image at the plane located 0.22 mm away from the impacted surface of sample 2-4

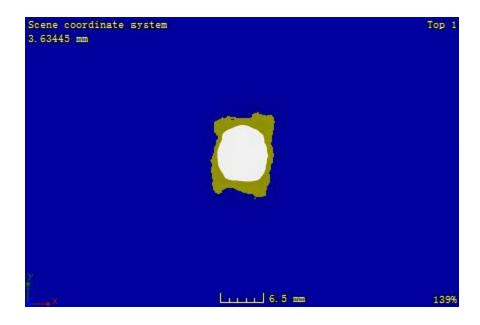


Figure C. 3: CT image at the plane located 0.47 mm away from the impacted surface of sample 2-4



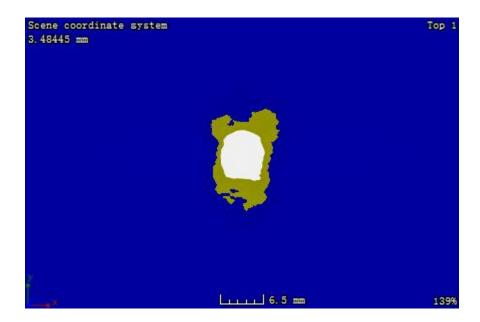


Figure C. 4: CT image at the plane located 0.62 mm away from the impacted surface of sample 2-4

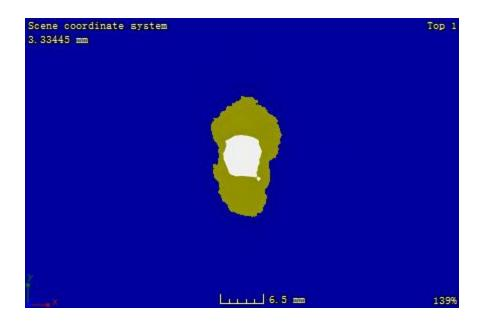


Figure C. 5: CT image at the plane located 0.77 mm away from the impacted surface of sample 2-4





Figure C. 6: CT image at the plane located 1.07 mm away from the impacted surface of sample 2-4

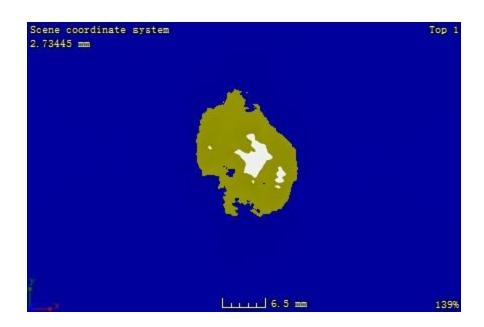


Figure C. 7: CT image at the plane located 1.37 mm away from the impacted surface of sample 2-4





Figure C. 8: CT image at the plane located 1.62 mm away from the impacted surface of sample 2-4

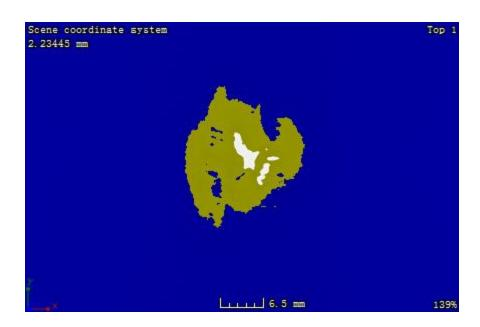


Figure C. 9: CT image at the plane located 1.87 mm away from the impacted surface of sample 2-4





Figure C. 10: CT image at the plane located 2.22 mm away from the impacted surface of sample 2-4

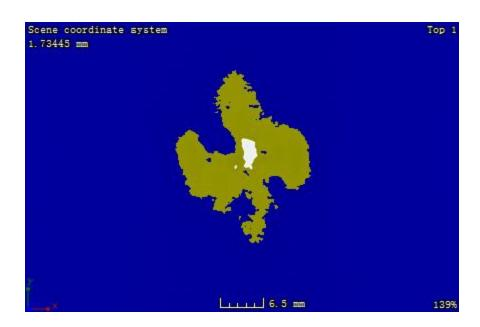


Figure C. 11: CT image at the plane located 2.37 mm away from the impacted surface of sample 2-4



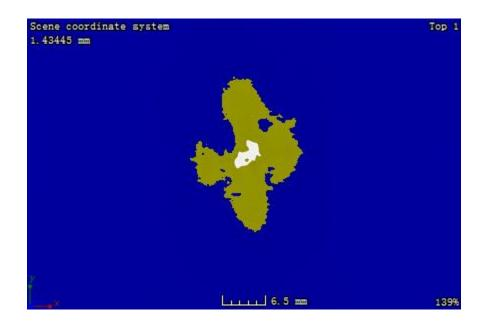


Figure C. 12: CT image at the plane located 2.67 mm away from the impacted surface of sample 2-4

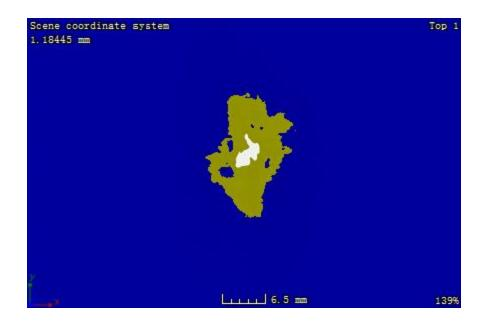


Figure C. 13: CT image at the plane located 2.97 mm away from the impacted surface of sample 2-4





Figure C. 14: CT image at the plane located 3.12 mm away from the impacted surface of sample 2-4

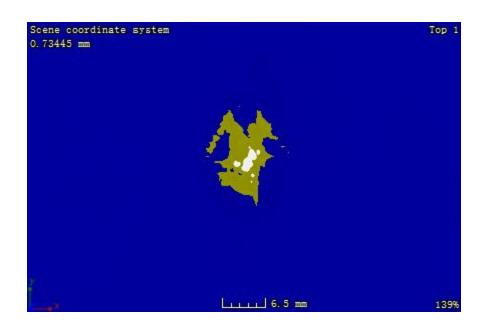


Figure C. 15: CT image at the plane located 3.37 mm away from the impacted surface of sample 2-4



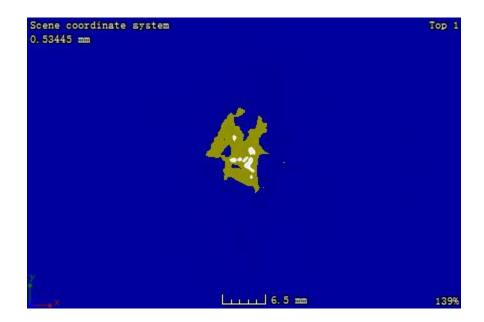


Figure C. 16: CT image at the plane located 3.57 mm away from the impacted surface of sample 2-4

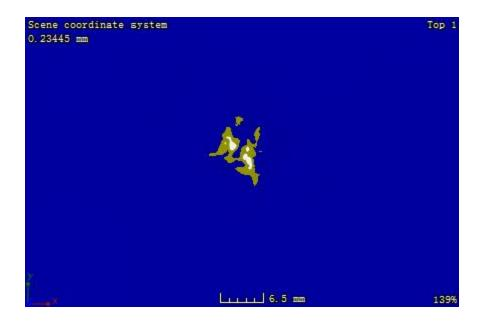


Figure C. 17: CT image at the plane located 3.87 mm away from the impacted surface of sample 2-4



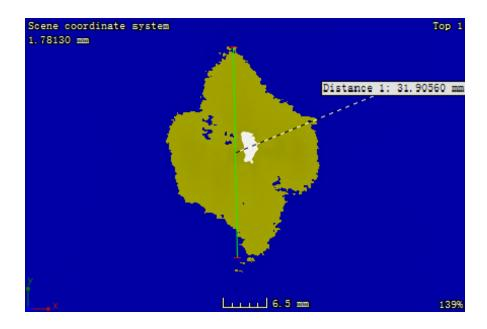
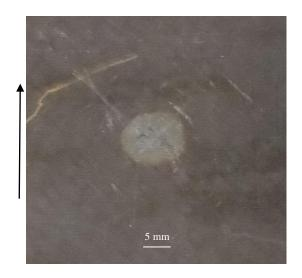


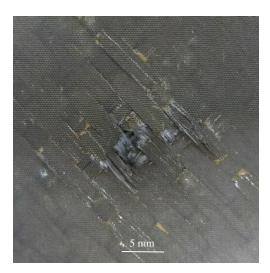
Figure C. 18: CT image at the plane with the largest damage size in sample 2-4 (located 2.43 mm away from the impacted surface)

In sample 2-4, the damage zone reached maximum size at the depth of 2.43 mm away from the impacted surface. Note that the thickness of sample 2-4 was 4.50 mm. The size of the largest damage area was measured by the software MyVGL and was 31.91 mm. It is also worth noticing that the orientation of the damage zone changes with depth. This is due to the fact that the tested samples are laminated composites that have multiple lamina of various orientation, i.e., 45°, -45°, 0°, and 90°.

Figure C.19 shows the impacted surface and a close view of the front (impacted side) and back surfaces of sample 2-5. The arrow on the left of Figure C.19 and C.20 shows 0 degree orientation. Figures C.20- C.36 show damage zones at different depths from the impacted surface of sample 2-5. As one can see, the extent of the damage zone increases with depth.







Front (impact) surface

Back surface

Figure C. 19: Sample 2-5

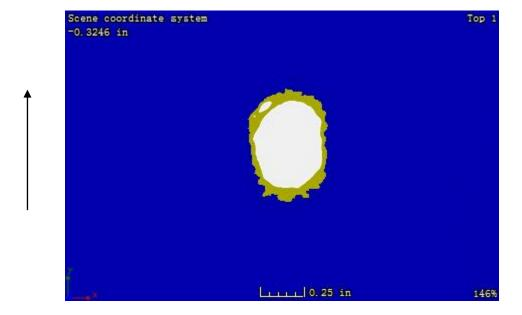


Figure C. 20: CT image at the plane located 0.22 mm away from the impacted surface of sample 2-5



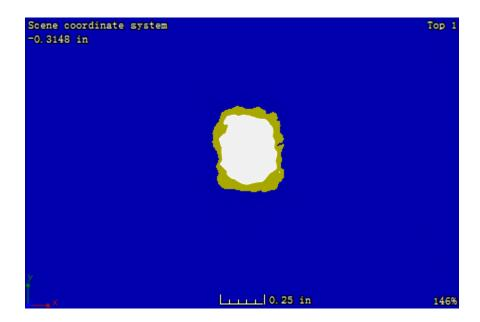


Figure C. 21: CT image at the plane located 0.47 mm away from the impacted surface of sample 2-5

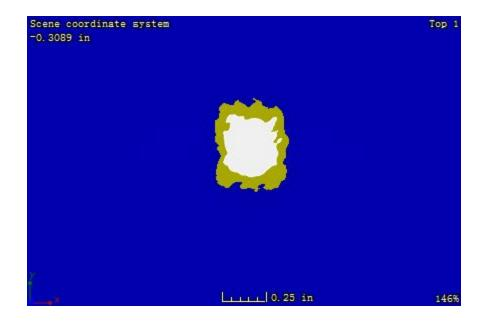


Figure C. 22: CT image at the plane located 0.62 mm away from the impacted surface of sample 2-5



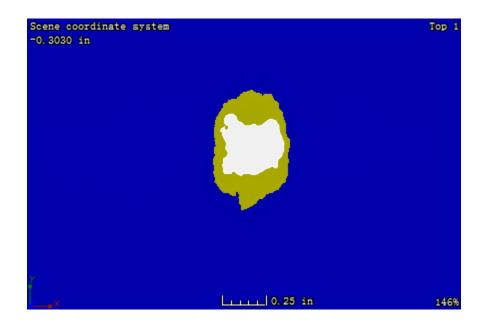


Figure C. 23: CT image at the plane located 0.77 mm away from the impacted surface of sample 2-5

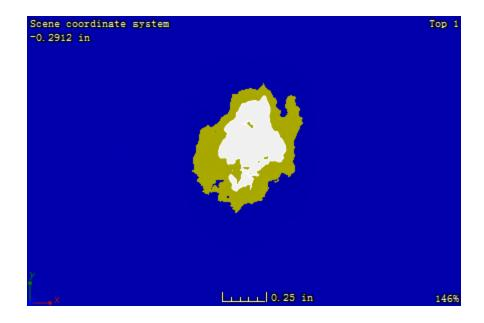


Figure C. 24: CT image at the plane located 1.07 mm away from the impacted surface of sample 2-5



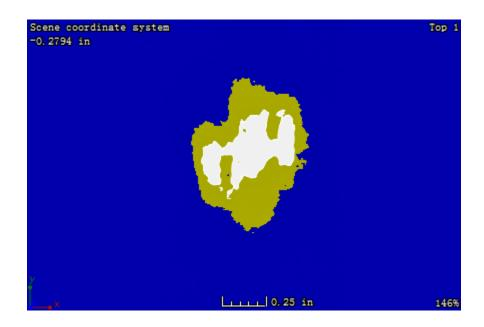


Figure C. 25: CT image at the plane located 1.37 mm away from the impacted surface of sample 2-5

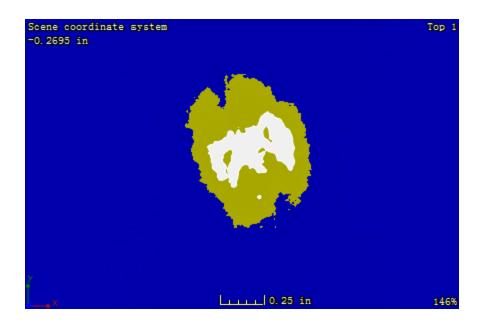


Figure C. 26: CT image at the plane located 1.62 mm away from the impacted surface of sample 2-5



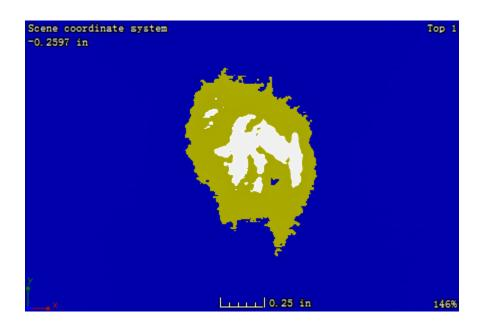


Figure C. 27: CT image at the plane located 1.87 mm away from the impacted surface of sample 2-5

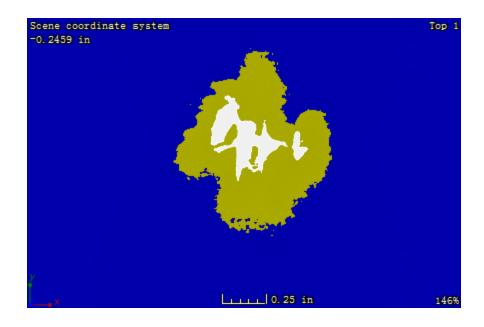


Figure C. 28: CT image at the plane located 2.22 mm away from the impacted surface of sample 2-5



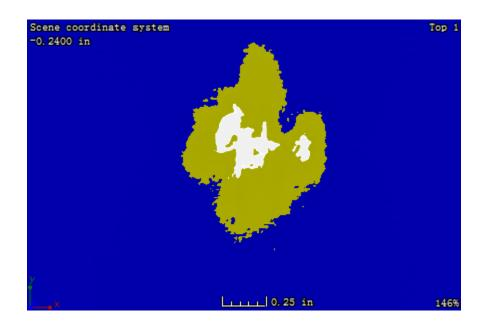


Figure C. 29: CT image at the plane located 2.37 mm away from the impacted surface of sample 2-5

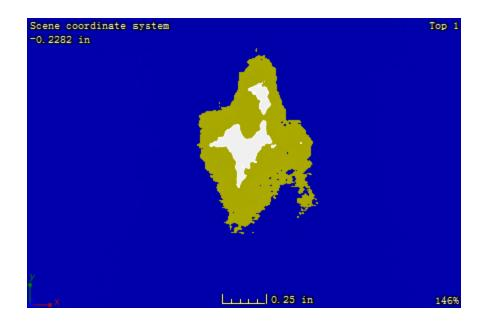


Figure C. 30: CT image at the plane located 2.67 mm away from the impacted surface of sample 2-5



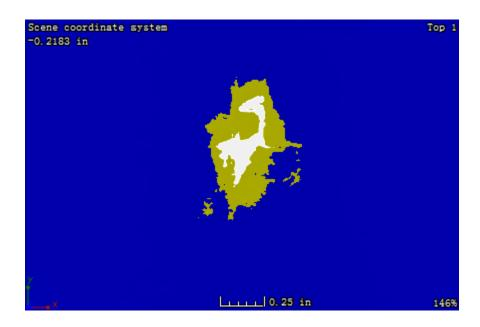


Figure C. 31: CT image at the plane located 2.92 mm away from the impacted surface of sample 2-5

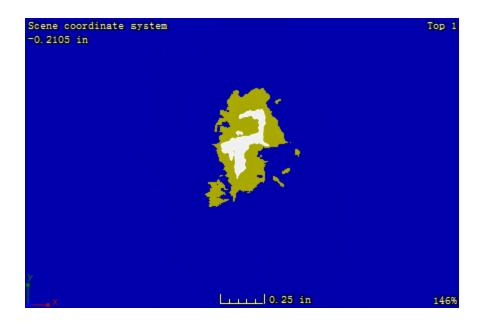


Figure C. 32: CT image at the plane located 3.12 mm away from the impacted surface of sample 2-5





Figure C. 33: CT image at the plane located 3.37 mm away from the impacted surface of sample 2-5

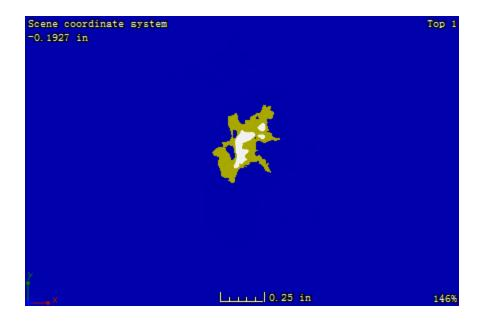


Figure C. 34: CT image at the plane located 3.57 mm away from the impacted surface of sample 2-5





Figure C. 35: CT image at the plane located 3.87 mm away from the impacted surface of sample 2-5

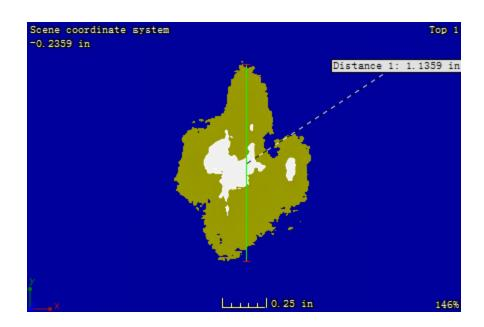


Figure C. 36: CT image at the plane with the largest damage size in sample 2-5 (located 2.47 mm away from the impacted surface)



As one can see, the extent of the damage zone increases with depth, and damage size reaches its maximum at the depth of 2.47 mm away from the impacted surface. Note that the thickness of sample 2-5 was 4.59mm. The size of the largest damage area was measured by the software MyVGL and was 28.85 mm (see Figure C.36).

The maximum measured damage in the sample 2-4 is smaller than in the samples 2-5. This observation is also in good correspondence with the maximum impact load and deflection at the maximum impact load (see Table 2.3). The maximum impact load and deflection at the maximum impact load in the sample 2-4 were higher than in the samples 2-5. It is also worth noting that the impact energy in the sample 2-4 was very similar to sample 2-5. Further comparisons of the impact damage size at the different depths in samples 2-4 and 2-5 are shown in Table 3.1.



## REFERENCES

- Abrate, S., 1998. Impact on Composite Structures. Cambridge University Press, Cambridge.
- A. Klepka, L. Pieczonka, W.J. Staszewski, and F. Aymerich. (2013). Impact damage detection in laminated composites by non-linearvibro-acoustic wave modulations. Composites: Part B xxx (2013) xxx–xxx.
- Ali Hallal, Rafic Younes, and Farouk Fardoun. (2013). Review and comparative study of analytical modeling for the elastic properties of textile composites. Composites: Part B, 50, 22-31.
- A&P Technology. (2014). Tailored Solutions. Retrieved from http://www.braider.com/Tailored-Solutions.aspx#Material\_Hybrids
- CesimAtas and OnurSyman. (2008). An overall view on impact response of woven fabric composite plates. Composites Structuers 82, 336-345.
- CesimAtas and Dahsin Liu. (2008). Impact response of woven composites with small weaving angles. International Journal of Impact Engineering 35, 80-97.
- Clarke S. (1998). Engineered textile preforms for RTM: a comparison of braiding, knitting and weaving technologies. SAMPE J 1998; 34:35–9
- Composites Manufacturing Online. (2013). A New Dimension for Aerospace: The growing interest for 3-D wovens in the aerospace market. Retrieved from http://www.compositesmanufacturingblog.com/2012/12/a-new-dimension-for-aerospace/
- "Dynatup Drop Weight Impact Test Machine Model 8200." Instron.13 Oct. 2008 http://www.instron.us/wa/products/impact/model\_8200
- Hexcel (2010). Technical Fabrics Handbook. U.S. 5-9
- "Is that carbon fiber? Nope. Say hello to Tegris." (2012). Retrieved from http://www.core77.com/blog/materials/is\_that\_carbon\_fiber\_nope\_say\_hello\_to\_t egris\_21732.asp
- Interjacm.wordpress.com. (2013). Aerospace Composite. Retrieved from http://interjacm.wordpress.com/article-3/about-aerospace-composite-3/applications/3d-textile-composite/.
- J.D.Winkel and D.F.Adams. (1985).Instrumented drop weight impact testing of cross-ply and fabric composites. Composites 16, 268-278



- J.N. Baucom and M.A. Zikry. (2005). Low-velocity impact damage progression in woven E-glass composite systems. Composites: Part A 36, 658-664.
- Makeev, A., Nikishkov, Y., Carpentier, P., Lee, E., and Noel, J. (2010), Manufacturing Issues and Measurement Techniques for Assessment of the Effects on Structural Performance of Composite Parts, Proceedings of the AHS 66th Annual Forum, Phoenix, AZ.
- Makeev, A and Nikishkov, Y. (2011), Fatigue Life Assessment for Composite Structure, 26th ICAF Symposium-Montreal, 1-3 June.
- Mehmet Aktas, H.Ersen Balcioglu, Alaattin Aktas, Erkan Turker, and M.Emin Deniz. (2012). Impact and post impact behavior of layer fabric composites. Composite Structures 94, 2809-2818.
- MicroCAT II. (2014). Retrieved from <a href="https://louisville.edu/advising/radiology/microcat-ii.html">https://louisville.edu/advising/radiology/microcat-ii.html</a>
- M.V. Hosur, M.Adbullah and S.Jeelani. (2005). Studies on the low-velocity impact response of woven hybrid composites. Composite Structures 67, 253-262.
- M.V.Hosur, C.R.L. Murthy, T.S. Ramamurthy, and Antia Shet. (1998). Estimation of impact-induced damage in CFRP laminates through ultrasonic imaging. NDT & E International, Vol. 31, No. 5, pp, 359-374
- My VGL 2.2 (2013), Software Manual.
- Naik NK et al. (2010). Damage in woven-fabric composites subjected to low-velocity impact. Compos SciTechnol 2000; 60:731-44
- Nicolas Chretien. (2002). Numerical constitutive models of woven and braided textile structural composite. Virginia Polytechnic Institute and State University.
- N.K. Naik, Y. Chandra Sekher and Sailendra Meduri.(2000). Damage in woven-fabric composites subjected to low-velocity impact. Composites Science and Technology 60, 731-744.
- N.K. Naik, P.Shrirao and B.C.K.Reddy. (2005). Ballistic impact behavior of woven fabric composites parametric studies. Materials Science and Engineering A 412, 104-106.
- N.Rajesh Mathivanan and J.Jerald. Experimental investigation of low-velocity impact characteristics of woven glass fiber epoxy matrix composite laminates of EP3 grade. Materials and Design 31 (2010) 4553-4560.



- Paul J. Schilling, Bhanu Prakash R. Karedla, Arun K. Tatiparthi, Melody A. Verges, and Paul D. Herrington. (2005). X-ray computed micro tomography of internal damage in fiber reinforced polymer matrix composites. Composites Science and Technology 65 (2005) 2071-2078.
- P. Tan, L. Tong and G.P. Steven. (1997). Modelling for predicting the mechanical properties of textile composites-A review. Composite: Part A, 28A, 903-922.
- Richard, Ketcham. (2012), X-ray Computed Tomography (CT), Integrating Research and Education Retrieved from http://serc.carleton.edu/research\_education/geochemsheets/techniques/CT.html
- Robert M. Jones. (1998). Mechanics of Composite Materials. U.S. Taylor & Francis.
- R. Usamentiaga, P. Venegas, J. Guerediaga, L. Vega, and I. Lopez. (2013). Automatic detection of impact damage in carbon fiber composites using active thermography. Infrared Physics & Technology 58 (2013) 36-46.
- Sinan Fidan, Tamer Sınmazcelik, and EgemenAvcu. (2012). Internal damage investigation of the impacted glass/glass aramid fiber reinforced composites by micro-computerized tomography. NDT & E International 51 (2012) 1-7.
- Stephen, Johnson. (2006), Stephen Johnson on Digital Photograhpy, O'Reilly. ISBN 0-596-52370-X.
- Stock SR. (1999). X-ray micro tomography of materials. Int Mater Rev 1999; 44 (4): 141-64.
- Tien-Wei Shyr and Yu-Hao Pan. (2003).Impact resistance and damage characteristics of composite laminates. Composite Structures 62, 193-203.
- VGStudio MAX 2.2 (2013), Production information Retrieved from http://www.volumegraphics.com/fileadmin/user\_upload/documents/Flyer/VGStudioMAX\_22\_en.pdf
- V.P.W. Shim and L.M. Yang. (2005). Characterization of the residual mechanical properties of woven fabric reinforced composites after low-velocity impact. International Journal of Mechanical Sciences 47, 647-665.

